

**GEDIZ UNIVERSITY ★ GRADUATE SCHOOL OF SCIENCE ENGINEERING AND
TECHNOLOGY**

**NANOSTRUCTURE ARRAYS FOR
DETECTION OF BIOMOLECULES**

M.Sc. THESIS

Sümeyra GÖKALP

Institute of Science

Nanotechnology Graduate Program

Thesis Advisor: Assist. Prof. Dr. Hadi M. ZAREIE

Co-Advisor: Prof. Dr. Yves J. CHABAL

DECEMBER 2013

**GEDIZ UNIVERSITY ★ GRADUATE SCHOOL OF SCIENCE ENGINEERING AND
TECHNOLOGY**

**NANOSTRUCTURE ARRAYS FOR
DETECTION OF BIOMOLECULES**

M.Sc. THESIS

**Sümevra GÖKALP
(60071102)**

Institute of Science

Nanotechnology Graduate Program

**Thesis Advisor: Assist. Prof. Dr. Hadi M. ZAREIE
Co-Advisor: Prof. Dr. Yves J. CHABAL**

DECEMBER 2013

GEDİZ ÜNİVERSİTESİ ★ FEN BİLİMLERİ ENSTİTÜSÜ

**BİYOMOLEKÜLLERİN TAYİNİNDE
NANODİZİLERİN KULLANIMI**

YÜKSEK LİSANS TEZİ

**Sümevra GÖKALP
(60071102)**

Fen Bilimleri Enstitüsü

Nanoteknoloji Yüksek Lisans Programı

**Tez Danışmanı: Yrd. Doç. Dr. Hadi M. ZAREIE
Eş Danışman: Prof. Dr. Yves J. CHABAL**

ARALIK 2013

Sümevra Gökarp, a **M.Sc.** student of **GU Institute of Science** student ID **60071102**, successfully defended the **thesis** entitled “**NANOSTRUCTURE ARRAYS FOR DETECTION OF BIOMOLECULES**”, which she prepared after fulfilling the requirements specified in the associated legislations, before the jury whose signatures are below.

Thesis Advisor : **Assist. Prof. Dr. Hadi M. ZAREİE**

İzmir Institute of Technology

Co-advisor : **Prof.Dr. Yves J. Chabal**

University of Texas at Dallas

Jury Members : **Assist. Prof. Dr. Hadi M. ZAREİE**

İzmir Institute of Technology

Prof. Dr. M. Emin Şengün ÖZSÖZ

Gediz University

Assoc. Prof. Dr. Gülnur AYGÜN

İzmir Institute of Technology

Date of Submission : 30 December 2013

Date of Defense : 23 December 2013

To my husband and family,

ACKNOWLEDGEMENT

First, I would like to thank my supervisor Assist. Prof. Hadi M. Zareie for his support and help throughout my master's studies. I am extremely grateful to Prof. Yves J. Chabal to allow me to work in his lab at University of Texas, and his support for my thesis studies. I would like to thank Research Scientist Jean Francois Veyan especially for his help in using XPS and all his support during the experiments.

My deepest appreciation goes to my dear husband, Assistant Professor Omer N. Gokalp. I would like to thank him for the nights that we stayed together in the labs, for his invaluable help during the writing stage of this thesis, and overall for his patience and moral support. Without him, this thesis would not have been possible.

I would like to thank my dear sister PhD Candidate Melike Karakaya for her help and advice on the technical details of my research and the writing of my thesis.

I am grateful to my dear mother and father, without their support, I would not be here today. I also thank my dear sister Fulya, my brother Fatih, and the newest member of our family, my dear nephew Emir, for their constant love and support.

Special thanks to the members of Laboratory for Surface and Nanostructure Modification at UT Dallas, for their hospitality during the last year of my master's studies. In particular, I thank Tatiana Peixoto for being a dear friend, and helping me with my orientation to life in the USA.

Finally I thank Hasan Aydin for his help with AFM. I also thank O. Oner Ekiz and Aysel Tomak for their help during experiment stages and Gülşah Malgır for her friendship.

Last but not least, I would like to thank my dear friend Pinar Arpacay, who, despite being far away in this process, has never lost connection and has always provided her support and friendship.

December 2013

Sümeýra GÖKALP
(M.Sc.)

TABLE OF CONTENTS

	<u>Page</u>
ACKNOWLEDGEMENT	viii
TABLE OF CONTENTS	ix
ABBREVIATIONS	xi
LIST OF TABLES	xii
LIST OF FIGURES	xiii
SUMMARY	xvii
ÖZET	xviii
1. INTRODUCTION	1
1.1 Biosensors	1
1.2 Nanosphere Lithography (NSL)	2
1.2.1 Nanostructures	3
1.3 Temperature Responsive Polymers	4
1.4 Biotin and Streptavidin	6
1.5 Self-Assembly Monolayers (SAMs)	6
1.6 Atomic Force Microscopy (AFM)	7
1.7 X-Ray Photoelectron Spectroscopy (XPS)	8
1.7.1 Principles	9
1.7.2 Applications	9
1.7.2.1 Elemental identification	10
1.7.2.2 Chemical state identification	11
1.7.2.3 Quantification	11
1.7.3 Charging and Discharging in XPS	11
2. EXPERIMENTAL SECTION	14
2.1 Preparation of Nanostructures	14
2.2 Functionalization of Nanosandwiches with Polymers	15
2.2.1 Functionalization phases	16
2.2.1.1 Binding of S _{PHO}	17
2.2.1.2 Binding of S _{PDS}	18
2.2.1.3 Binding of S _{PDS+PHO}	19
2.2.2 Investigation of polymer phase transition on nanosandwich arrays	19
2.3 Charge-Contrast XPS	21
2.4 External Resistance	23
3. RESULT AND DISCUSSION	25
3.1 AFM Analyses of Nanosandwich Arrays Before And After Modification with Polymers	25
3.1.1 Au /Al ₂ O ₃ /Au (20 nm /20 nm/ 20 nm) nanosandwiches without functionalization (S ₁)	25
3.1.2 Au / Al ₂ O ₃ / Au nanosandwiches before and after functionalization with PHO polymer	26
3.1.3 Au/ Al ₂ O ₃ / Au nanosandwiches before and after functionalization with PDS polymer	27
3.1.4 Au/ Al ₂ O ₃ / Au nanosandwiches before and after functionalization with PHO+PDS polymers	28
3.1.5 Au/ Al ₂ O ₃ / Au nanosandwiches before and after functionalization with SA biomolecule	29

3.1.6 Au/ HfO ₂ / Au (20 nm/ 20 nm/ 20 nm) nanosandwiches without functionalization (S ₂).....	30
3.1.7 Au /HfO ₂ /Au nanosandwiches before and after functionalization with PDS polymers.....	31
3.1.8 Au /HfO ₂ /Au nanosandwiches before and after functionalization with ATES polymer.....	31
3.1.9 Au /HfO ₂ /Au nanosandwiches before and after functionalization with PDS+ATES polymers	32
3.2 Survey Spectrum Measurement of Nanostructures With XPS.....	33
3.3 Detailed Analysis of the Elements in the Samples	42
3.4 Applying External Square Wave Pulse for Monitoring Frequency Dependence of Nanostructures.....	53
3.5 Charging and Discharging Properties of Nanostructures	59
3.6 Connection of External Resistance.....	78
3.7 Calculation of Capacitance Values.....	88
3.8 Comparison of Theoretical and Experimental Capacitance Values	91
4. CONCLUSIONS AND RECOMMENDATIONS	93
REFERENCES	95
CURRICULUM VITAE.....	101

ABBREVIATIONS

2D	: Two Dimensional
3D	: Three Dimensional
AFM	: Atomic Force Microscopy
ATES	: Silane terminated polymer
BE	: Binding Energy
BNC	: Bayonet Neill-Concelman
c/s	: Coulomb/Second
DC	: Direct current
DI	: Deionized Water
ESCA	: Electron Spectroscopy for Chemical Analysis
eV	: Electron Volt
Hz	: Hertz
KE	: Kinetic Energy
kHz	: Kilohertz
LCST	: Lower Critical Solution Temperature
m²	: Meter square
MEMA	: Methyl ether methacrylate
MΩ	: Mega Ohm
nm	: Nanometer
NSL	: Nano Sphere Lithography
ODPA	: Oxydiphthalic anhydride
OEGMA	: Oligo(ethylene glycol) methyl ether methacrylate
PDMS	: Polymethylsiloxane
PDS	: Thiol terminated polymer
PEG	: Polyethylene glycol polymers
PHO	: Phosphoric acid ester
PMPMS	: Poly(mercaptopropyl)methylsiloxane
PNIPAM	: Poly (N-isopropyl acrylamide)
PS/PMMA	: Polystyrene-b-poly(methyl methacrylate) copolymer
RAFT	: Reversible addition fragmentation chair-transfer
RF	: Radio Frequency
SAMs	: Self Assembly Monolayers
SPM	: Scanning Probe Microscopy
SQW	: Square wave pulses
TRP	: Temperature responsive polymer solutions
UHV	: Ultra High Vacuum
V	: Volt
XPS	: X-Ray Photoelectron Spectroscopy

LIST OF TABLES

	<u>Page</u>
Table 2.1 : Polymers end-groups and binding groups.....	16
Table 2.2 : The Production of the sample 1	17
Table 2.3 : The Production of the sample 2	17
Table 3.1 : The binding energy values for Al, C, Au, Hf, N, O, P, Si, S elements ...	33
Table 3.2 : The list of the values of binding energies, heights and areas of the samples	46
Table 3.3 : Tabulated values of binding energy, height and area on the samples (S_2 , S_{2PDS} , S_{2ATES} , $S_{2ATES+PDS}$)	48
Table 3.4 : The B.E differences Vs. frequency values S_{1PHO}	60
Table 3.5 : The B.E differences Vs. frequency values S_{1PHO}	62
Table 3.6 : The B.E differences vs. frequency values S_{1PDS}	64
Table 3.7 : The B.E differences Vs. frequency values $S_{1PDS+PHO}$	65
Table 3.8 : The B.E differences vs. frequency values for S_{1SA}	66
Table 3.9 : The comparison of the binding energy difference versus frequency for the five samples which consist of Au/ Al_2O_3 / Au nanosandwicheshe Production of the sample	68
Table 3.10 : The B.E differences vs. frequency values for S_2	69
Table 3.11 : The B.E differences frequency values for S_{2PDS}	71
Table 3.12 : The B.E differences frequency values for S_{2ATES}	72
Table 3.13 : The B.E differences vs frequency values for $S_{2PDS+ATES}$	74
Table 3.14 : The comparison of the binding energy difference versus frequency for the five samples which consist of Au/ HfO_2 / Au nanosandwiches.....	75
Table 3.15 : The comparison of the binding energy differences per different frequencies for nine samples which consist of Au/ Al_2O_3 / Au nanosandwiches and Au/ HfO_2 /Au nanosandwiches	77
Table 3.16 : The measured difference between the peaks versus frequencies for the samples which consist of Au/ Al_2O_3 / Au nanosandwiches.....	79
Table 3.17 : The measured difference between the peaks versus frequency for the samples which consist of Au/ HfO_2 / Au nanosandwiches.....	80
Table 3.18 : Cutoff frequency values for samples which includes Au/ Al_2O_3 / Au and Au/ HfO_2 / Au nanosandwiches	88
Table 3.19 : An excel program for calculation of the real and theoretical capacitance values	90
Table 3.20 : Experimental and theoretical capacitance values of the nine samples..	91

LIST OF FIGURES

	<u>Page</u>
Figure 1.1 : Basic working principles of a typical biosensor (Belluzo et al., 2008)...	1
Figure 1.2 : Scanning Electron Microscopy micrograph was prepared using NSL by Dr. Hadi Zareie.	3
Figure 1.3 : The depiction of tapping mode atomic force microscopy of triangle nanostructures	4
Figure 1.4 : Collapse form of the responsive polymer after LCST is reached (Gil and Hudson, 2004).....	5
Figure 1.5 : SAM formation process (left) and the anchoring of head group on the surface (right) (Schreiber, 2000).....	7
Figure 1.6 : AFM image from Nanomagnetic Instruments.....	8
Figure 1.7 : Schematic illustration of the working principle of X-Ray Photoelectron Spectroscopy	9
Figure 1.8 : XPS survey spectrum of S ₂ ATES+PDS on the silicon surface.....	10
Figure 2.1 : Schematic illustration of the general process of the preparation of the nanosandwich arrays by Nanosphere Lithography (NSL) (A) Spin coating of polystyrene beads.(B) Metal deposition, (C) Lift off, (D) Single hexagonal nanosandwich array.	15
Figure 2.2 : Functionalization of a nanosandwich composed of three layers with temperature-responsive polymers.	16
Figure 2.3 : Schematic illustration of the nanosandwiches before and after functionalization with phosphate-terminated polymer to Al ₂ O ₃ layer... ..	18
Figure 2.4 : Schematic illustration of the nanosandwiches before and after functionalized with thiol-terminated polymers to gold layers	18
Figure 2.5 : Schematic illustration of the nanosandwiches before and after functionalized with phosphate and thiol-terminated polymers to their specific metal layers which are Al ₂ O ₃ and Au, respectively	19
Figure 2.6 : (A) Schematic illustration of the functionalized nanosandwich arrays with thiol terminated polymer above the LCST. (a) unfunctionalized and (b) functionalized nanosandwich arrays with thiol terminated polymer at below LCST (25 °C) and (c) above LCST (45 °C).	20
Figure 2.7 : (A) Schematic illustration of mixed SAM functionalized nanosandwiches and streptavidin detection above the LCST.....	20
Figure 2.8 : Experimental Setup	21
Figure 2.9 : Display of the oscilloscope showing the function delivered by the SQW function generator.	22
Figure 2.10 : SQW function generator.....	22
Figure 2.11 : SQW function generator connected to the sample through a UHV BNC connector located on the main XPS chamber.....	23
Figure 2.12 : The illustration of the external resistance between XPS input and function generator A) XPS input, B) 10MΩ external resistance, and C) function generator	24
Figure 3.1 : Tapping mode AFM images of unfunctionalized nanosandwiches of Au/ Al ₂ O ₃ / Au (20 nm/ 20 nm/ 20 nm) on Si substrate A) 5μ×5μ, B) enlarged image of A (1μ×1μ).	25

Figure 3.2 : Tapping mode AFM images of A) functionalized (S_1) and B) phosphate-terminated polymer functionalized (S_{1PHO}) nanosandwiches arrays on Si as represented at $2\mu \times 2\mu$.	26
Figure 3.3 : Tapping mode AFM images of A) functionalized (S_1) and B) phosphate-terminated polymer functionalized (S_{1PDS}) nanosandwiches arrays on Si as represented at $2\mu \times 2\mu$ and $1\mu \times 1\mu$, respectively.	27
Figure 3.4 : Tapping mode AFM images of A) unfunctionalized (S_1) and B) phosphate- terminated polymer functionalized ($S_{1PHO+PDS}$) nanosandwiches arrays on Si as represented at $2\mu \times 2\mu$.	28
Figure 3.5 : Tapping mode AFM images of A) unfunctionalized (S_1) and B) functionalized with streptavidin biomolecule (S_{1SA}) above the lower critical temperature (LCST) of the polymer on nanosandwich arrays as represented at $2\mu \times 2\mu$.	29
Figure 3.6 : Tapping mode AFM images of unfunctionalized (S_2) A) $10\mu \times 10\mu$ and B) enlarged image of A ($0.7\mu \times 0.7\mu$).	30
Figure 3.7 : Tapping mode AFM images of A) unfunctionalized (S_2) ($0.7\mu \times 0.7\mu$) and B) functionalized thiol-terminated polymers (S_{2PDS}) nanosandwiches arrays on Si as represented at $2\mu \times 2\mu$.	31
Figure 3.8 : Tapping mode AFM images of A) unfunctionalized (S_2) ($0.7\mu \times 0.7\mu$) and B) functionalized silane-terminated polymers (S_{2ATES}) nanosandwiches arrays on Si as represented at $2\mu \times 2\mu$.	31
Figure 3.9 : Tapping mode AFM images of A) unfunctionalized (S_2) ($0.7\mu \times 0.7\mu$) and B) functionalized thiol and silane-terminated polymers ($S_{2PDS+ATES}$) nanosandwiches arrays on Si as represented at $2\mu \times 2\mu$.	32
Figure 3.10 : Wide Survey Spectrum of Sample 1 (S_1)	34
Figure 3.11 : Wide Survey Spectrum of Sample 2 (S_{1PHO})	35
Figure 3.12 : Wide Survey Spectrum of Sample 3 (S_{1PDS})	36
Figure 3.13 : Wide Survey Spectrum of Sample 4 ($S_{1PHO+PDS}$)	37
Figure 3.14 : Wide Survey Spectrum of Sample 5 (S_{1SA})	38
Figure 3.15 : Wide Survey Spectrum of Sample 6 (S_2)	39
Figure 3.16 : Wide Survey Spectrum of Sample 7 (S_{2PDS})	40
Figure 3.17 : Wide Survey Spectrum of Sample 8 (S_{2ATES})	41
Figure 3.18 : Wide Survey Spectrum of Sample 9 ($S_{2ATES+PDS}$)	42
Figure 3.19 : Au4f region of the samples on Si substrate when the samples are grounded	44
Figure 3.20 : O1s spectrum of the sample recorded, when grounded.	45
Figure 3.21 : XPS spectra of the Si2p region of the samples on Si substrate	46
Figure 3.22 : Comparison of the C1s spectra for S_1 , S_{1PHO} , S_{1PDS} , $S_{1PDS+PHO}$ and S_{1SA}	47
Figure 3.23 : Comparison of the C1s region for S_2 , S_{2PDS} , S_{2ATES} and $S_{2ATES+PDS}$	48
Figure 3.24 : XPS spectra of Al2p region for the samples	49
Figure 3.25 : P2p region of the grounded samples on the Si substrate	50
Figure 3.26 : XPS spectrum of the Hf4f region on the samples	51
Figure 3.27 : S2p spectrum of the grounded samples	52
Figure 3.28 : XPS spectrum of the N1s region	53
Figure 3.29 : XPS data from the Au4f region	55
Figure 3.30 : Si2p spectra of recorded, when grounded (dashed curves) and when subjected to $\pm 10V$ SQW pulses of 150 kHz (solid curves)	56
Figure 3.31 : C1s region under ± 10 SQW excitation for the nanostructures	57

Figure 3.32 : XPS spectra for O1s region when grounded and subjected to $\pm 10V$ amplitude of SQW pulses	57
Figure 3.33 : XPS data from the O 1s region when a $\pm 10V$ amplitude voltage is applied to the sample for different frequencies: 185 kHz, 190 kHz, 195 kHz and 200 kHz.	58
Figure 3.34 : Frequency dependence of the measured difference between the peaks for S_1	60
Figure 3.35 : Frequency dependence of the measured difference between the peaks like Figure 24 for S_{1PHO}	62
Figure 3.36 : Frequency dependence of the measured difference between the peaks like Figure 3.33 for S_{1PDS}	63
Figure 3.37 : The measured B.E difference was plotted against the frequency for $S_{1PDS+PHO}$	65
Figure 3.38 : The measured B.E difference was plotted against the frequency for S_{1SA}	66
Figure 3.39 : The comparison of the binding energy difference versus frequency for the five samples which consist of Au/ Al_2O_3 / Au nanosandwiches ...	67
Figure 3.40 : The measured B.E difference was plotted against the frequency for $S_2(Au, HfO_2/ Au$ nanosandwiches.	69
Figure 3.41 : The measured B.E difference was plotted vs against frequency for S_{2PDS}	70
Figure 3.42 : The measured B.E difference was plotted vs against frequency for S_{2ATES}	72
Figure 3.43 : The measured B.E difference was plotted against frequency for $S_{2PDS+ATES}$	73
Figure 3.44 : The comparison of the binding energy difference versus frequency for the five samples which consist of Au/ HfO_2 / Au nanosandwiches. ...	75
Figure 3.45 : Connecting an external resistance (10M Ω) between the samples (inside XPS) and function generator.	78
Figure 3.46 : Frequency dependence of the distance of peaks for Au/ Al_2O_3 / Au samples	79
Figure 3.47 : Frequency dependence of the distance of peaks for Au/ HfO_2 / Au samples	80
Figure 3.48 : XPS spectrum with RC at 1Hz	81
Figure 3.49 : XPS spectrum with RC at 100Hz	81
Figure 3.50 : XPS spectrum with RC at 200Hz	82
Figure 3.51 : XPS spectrum with RC at 300Hz	82
Figure 3.52 : XPS spectrum with RC at 400Hz	82
Figure 3.53 : XPS spectrum with RC at 500Hz	83
Figure 3.54 : XPS spectrum with RC at 600Hz	83
Figure 3.55 : XPS spectrum with RC at 700Hz	83
Figure 3.56 : XPS spectrum with RC at 800Hz	84
Figure 3.57 : XPS spectrum with RC at 900Hz	84
Figure 3.58 : XPS spectrum with RC at 1000Hz	84
Figure 3.59 : XPS spectrum with RC at 2000Hz	85
Figure 3.60 : XPS spectrum with RC at 3000Hz	85
Figure 3.61 : XPS spectrum with RC at 4000Hz	85
Figure 3.62 : XPS spectrum with RC at 5000Hz	86
Figure 3.63 : XPS spectrum with RC at 6000Hz	86
Figure 3.64 : XPS spectrum with RC at 7000Hz	86

Figure 3.65 : XPS spectrum with RC at 8000Hz	87
Figure 3.66 : XPS spectrum with RC at 9000Hz	87
Figure 3.67 : XPS spectrum with RC at 10000Hz	87
Figure 3.68 : A schematic display of a nanosandwich (Au/ Al ₂ O ₃ / Au) which has 60 nm thickness, 240 nm height and 170 nm base.	89
Figure 3.69 : Plate area A.....	89

NANOSTRUCTURE ARRAYS FOR DETECTION OF BIOMOLECULES

SUMMARY

In this study, the sandwich-like nanostructure arrays are functionalized with temperature responsive polymers and multiple biomolecule species, and the capacitance properties of these nanosandwiches are examined at different frequencies intervals under external voltage and square wave pulses using XPS.

As a result of this project, we obtained a novel and improved biosensor by using the nanomaterials we developed. These biosensors can be used for diagnosis of multiple diseases with single blood sample with immediate applications in biomedicine and biotechnology.

9 different samples were prepared by modifying Au/ Al₂O₃/ Au and Au/ HfO₂/ Au (20nm/ 20nm/ 20 nm) metal/insulator/metal multiple layer nanostructures with PDS, PHO, ATEs end group temperature responsive polymers and biotin-streptavidin biomolecule. Each sample's capacitance parameters were examined by XPS at 150-250 kHz frequency levels under ± 10 external voltage. Thus, the capacitance values of nanostructures modified by different polymers and biomolecules at different frequency levels are calculated by using their charging/discharging properties.

Lastly, to calculate the mathematical values of the empirically observed capacitance values, a 10 mega ohm resistance is included between ± 10 voltage and XPS, and measurements were recorded between 150-250 kHz frequency level. This way, the effect of Al₂O₃ and HfO₂ –insulators which are at the middle layer of nanosandwiches and have different dielectric properties- on the capacitance values are calculated. Capacitance measurements of nanosandwich structures have not been reported in the literature as a possible transduction mechanism for the detection of biological binding events.

Keywords: Nanosphere Lithography, Nanostructures, XPS, Charging/ Discharging Properties, Differential charging, Capacitance Properties

BİYOMOLEKÜLLERİN TAYİNİNDE NANODİZİLERİN KULLANIMI

ÖZET

Bu çalışmada, “Nanosphere Litografi” tekniği kullanılarak elde edilen sandviç görünümlü nanoyapılı diziler sıcaklığa duyarlı polimerler ve çok katmanlı biyomolekül türleriyle işlevselleştirilmiştir. Bu nanosandviçlerin kapasitans özellikleri XPS (X-ışını fotoelektron spektroskopisi) kullanılarak dışarıdan doğrusal voltaj ve kare dalgalar uygulanarak farklı frekans aralıklarında incelenmiştir.

Bu projede, nanosphere tekniği ile elde edilen nanomalzemeler kullanarak kapasitans bazlı yeni nesil biosensörler geliştirilmiştir. Tek bir kan örneğinden bir çok hastalığı aynı anda doğrudan teşhis edebilen bu biyosensörler biyotıp ve biyoteknoloji alanında kullanılabilirler.

Au/ Al₂O₃/ Au and Au/ HfO₂/ Au (20nm/ 20nm/ 20 nm) metal/ yalıtkan/ metal çok katlı tabakalarından oluşan nanoyapılar PDS, PHO, ATEŞ uç gruplu sıcaklığa duyarlı polimerlerle ve biyotin-streptavidin biyomolekülü ile modifiye edilerek dokuz farklı örnek hazırlanmıştır. Her bir örneğe 150-250 kHz frekans aralığında dışardan ± 10 V doğrusal voltaj uygulanmış ve kapasitans parametreleri XPS cihazı ile incelenmiştir. Böylece her bir farklı polimerle ve biyomolekülle modifiye edilmiş nanoyapıların, şarj/deşarj özelliklerinden yararlanılarak farklı spesifik frekans aralıklarındaki kapasitans değerleri hesaplanmıştır.

Son olarak, deneysel olarak gözlenen kapasitans özelliklerinin matematiksel hesaplamaları yapılmıştır. Bunun için örneklere dışarıdan ± 10 V'luk voltaj uygulanmış ve XPS cihazı ile örnekler arasında 10 mega ohm luk bir direnç bağlanarak 150-250 kHz frekans aralığında spektrumlar alınmıştır. Böylece nanosandviçlerin orta tabakasında bulunan dielektrik davranışları birbirinden farklı olan Al₂O₃ ve HfO₂ yalıtkanlarının kapasitans değerlerine etkisi hesaplanmıştır. Nanosandviç yapıları kapasitans ölçümleriyle biyolojik bağlanma olaylarını açıklamak için kullanılan bu tür transdüksiyon mekanizmalarına daha önce literatürde rastlanmamaktadır.

Anahtar Kelimeler: Nanosphere Litografi, nanoyapılar, XPS, Şarj/deşarj özellikleri, diferansiyel şarj, kapasitans özellikleri

1. INTRODUCTION

1.1 Biosensors

The advances in the techniques used for the detection of metabolites such as glucose, urea, and cholesterol in blood are critical in the clinical diagnostic field. Biosensors are devices that are commonly used for biological monitoring and environmental sensing applications (Védrine et al., 2003). A biosensor is defined as “an analytical device that combines the specificity of a biological sensing element with a transducer to produce a signal proportional to target analyte concentration” (Zhai et al., 1997). A simple depiction of a biosensor is provided in Figure 1 below.

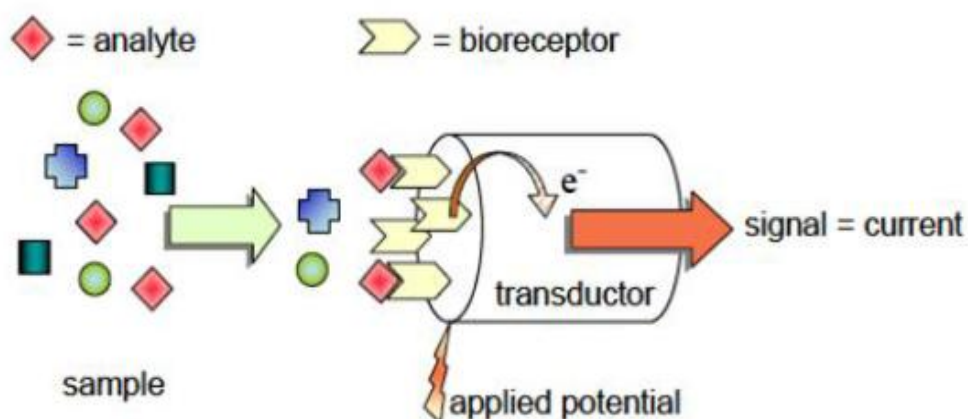


Figure 1.1 : Basic working principles of a typical biosensor (Belluzo et al., 2008)

In the drug discovery and medicine fields, it is important to be able to examine large numbers of samples in a quick and sensitive way. Such applications that require high throughput monitoring can be facilitated through the use of multiple biomolecule detecting biosensors. The recent developments in nanotechnology field helped improve the sensitivity and performance of biosensors used for these purposes (Jianrong et al., 2004). The use of multiple layers of nanostructures (metal/insulator/metal layers) enables the detection of multiple biomolecules with high sensitivity for high throughput applications for diagnosis of diseases.

Biosensors need to translate the biorecognition events to quantifiable signals, thus the transduction mechanisms should be able to produce sensitive and quantitative signals reliably. As an alternative to the transduction mechanism, we can use mechanisms that can identify a change in the inherent properties of the analyte or the biochip surface after binding. In this study, we offer such a desirable alternative to the traditional transduction methods, by using capacitance of the sandwich like nanostructures as a function of biomolecular binding events. Our method is unique because it provides a simple and inexpensive, yet sensitive and reliable method for biosensors. Specifically, we generate sandwich-like nanostructure arrays from metal/insulator/metal layers by using nanosphere lithography, which will be described in the next section.

1.2 Nanosphere Lithography (NSL)

Lithography techniques are typically used to obtain arrays of nanostructures. Well known lithography techniques used in the literature are e-beam lithography, ion-beam lithography, photolithography and nanosphere lithography (Haes and Van Duyne, 2004). In this study, we used nanosphere lithography (NSL) to fabricate arrays of metal/insulator nanostructures due to certain advantages of this method. We will define NSL, and discuss its advantages below.

NSL is a high-powered production method of the 2D periodic particle arrays of nanoparticles where the shape and size of the nanoparticles and the spacing among them are controlled (Hulteen et al., 1999), (Zareie et al., 2008b). It is a very simple and inexpensive technique that was first introduced by (Deckman and Dunsmuir, 1983) as “natural lithography”, and later advanced by the work of (Hulteen and Van Duyne, 1995) who renamed the method to “nanosphere lithography”. During the self-assembly of nanospheres (i.e. polystyrene particles), the NSL procedure can be changed to include a liquid/gas interface to produce defect free monolayers over an area of $\sim 1\text{cm}^2$ (Wagner, 1979). This way, the 2D periodic particle arrays are patterned in a parallel on the surface as self-assembly monolayers (Haes and Van Duyne, 2004).

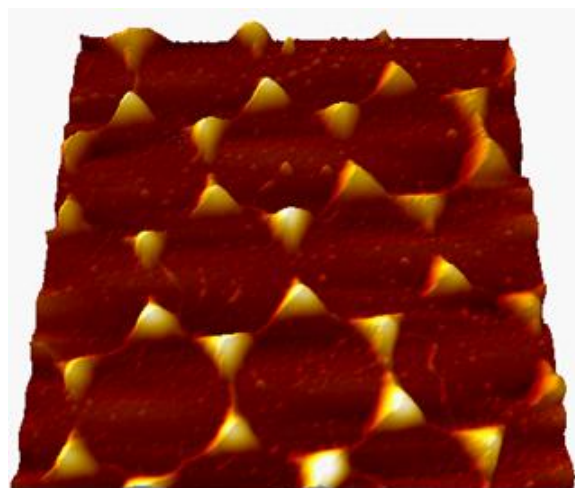


Figure 1.3 : The depiction of tapping mode atomic force microscopy of triangle nanostructures (Zareie et al., 2008a)

We used nanoparticles in order to fabricate arrays of nanostructures composed of metal/insulator/metal layers (Au/Al₂O₃/Au and Au/HfO₂/Au nanosandwiches) of 20 nanometer thickness by using Nanosphere lithography.

1.3 Temperature Responsive Polymers

Polymer based responsive systems are widely used in biomedical, nanomedicine, nanotechnology and other related fields due to their nonlinear response to even smallest changes in the environmental stimuli (Ulgut and Suzer, 2003), (Cabane et al., 2012). These stimuli can be chemical, physical, or biological in nature. Examples of chemical stimuli include pH, ionic strength, or redox; while physical stimuli include temperature, light, and electric field; and biological stimuli typically involve analytes and biomacromolecules (Cabane et al., 2012). When applied to stimuli responsive polymers (smart polymers) these stimuli result in responses such as phase separation, shape change, and permeability.

For the purposes of our study, where we focus on biosensor applications, we used temperature responsive polymers that respond to small changes in temperature in the environment with sudden and large changes in their conformation. Temperature responsive polymers are most typically used form of physical stimuli for the phase separation (Gil and Hudson, 2004), (Schmaljohann, 2006). For example, it has been shown that the changes in the conformation of polymer chains can determine the interaction of a biomolecule and its ligand (Bulmus et al., 2000).

The phase separation happens when the temperature goes above a critical threshold point, which is called lower critical solution temperature (LCST), and it is reversible when the temperature goes below LCST (Hoffman, 1995). Polymer chains in solution are collapsed when the temperature is increased above LCST, resulting in an interface with a less hydrophilic state. With the introduction of hydrophilic or hydrophobic components to the polymer structure, the LCST of temperature responsive polymers can be changed. Typical polymers with adjustable LCST values that are used for biological applications are Poly (N-isopropyl acrylamide) (PNIPAM) and poly (ethylene glycol methyl ether (meth) acrylate). In this study we used poly ethylene glycol based polymers which are non-fouling compellent and biocompatible temperature responsive polymers. These polyethylene glycol polymers (PEG) are produced by using MEMA, MEO₂MA, and OEGMA₃₀₀ monomers (Xu et al., 2008), (Xu et al., 2008), (Fan et al., 2006) with the RAFT technique (Boyer et al., 2009), (Huang et al., 2009)

These copolymers have specific LCST values within the range of 20C to 45C, and they have specific functional end groups such as thiol (PDS), phosphoric acid ester (PHO), or silane (ATES) that bind to only one layer of Au/Al₂O₃/HfO₂ metal-insulator layers, respectively (Zareie et al., 2008a). These co-polymers were produced by Dr. Volga Bulmus Zareie and her group.

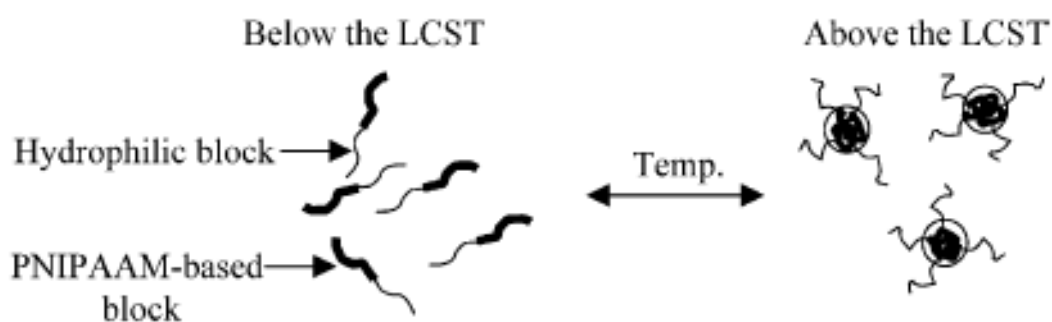


Figure 1.4 : Collapse form of the responsive polymer after LCST is reached (Gil and Hudson, 2004)

Our unique contribution in this study is to functionalize PDS, PHO, and ATES end groups with PEG based temperature responsive polymers for controlling the affinity between multiple biomolecule pairs, namely biotin and streptavidin on metal/insulator/metal nanosandwiches for detecting multiple biorecognition features.

1.4 Biotin and Streptavidin

The detecting of multiple biorecognition features is very important for the development of biosensor technology (Xia et al., 2004). Streptavidin and biotin are common and important biomolecules for the detection of biorecognition. To our knowledge, in past studies temperature responsive polymers have not been used to control multiple biomolecular (streptavidin biotin) recognition events. We applied this technique by mixing biotin and polymer with SAMs technique. Biotin is a vitamin well known with its use in nano-biotechnology applications. Streptavidin is a protein with a symmetrical cubic structure with strong affinity towards its ligand, biotin (Xia et al., 2004). The Streptavidin-Biotin couple is extensively used as a molecular linker (Xia et al., 2004) in areas such as diagnostic applications in medical research (Young, 2000), (Faber et al., 2002), drug discovery (Lal et al., 2002) fundamental and cellular biology investigations (Zhu et al., 2001), and analytical sensor developments (Rowe et al., 1999), (Michael et al., 1998).

In our study, the temperature responsive polymers are mixed with biotin in order to obtain biotinylated surfaces. The nanosandwich arrays are functionalized with these polymers and biotin mixtures by using Self Assembly Monolayers (SAMs) method for controlled binding of streptavidin biomolecules.

1.5 Self-Assembly Monolayers (SAMs)

The most commonly used method for anchoring temperature responsive polymers and biomolecules on the surfaces is Self-Assembly Monolayers (SAMs), defined as “ordered molecular assemblies formed by the adsorption of an active surfactant on a solid surface” (Ulman, 1996). SAMs are nanostructures with a typical thickness of 1-3 nm, and their molecular components determine the different surface properties, stabilize surface atoms, and alter the electrical and physical properties of the surface (Love et al., 2005).

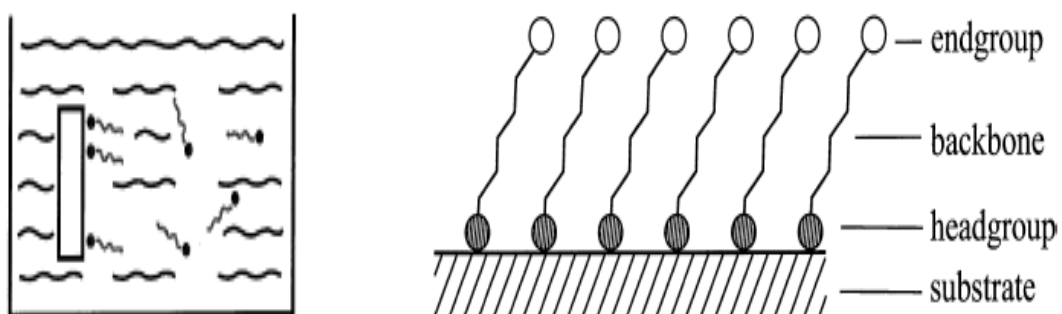


Figure 1.5 : SAM formation process (left) and the anchoring of head group on the surface (right) (Schreiber, 2000)

In our study, the head groups in the temperature responsive polymer solutions (TRP) spontaneously grafted on their specific metal or insulator surfaces such as Au/Al₂O₃/Au or Au/HfO₂/Au as well-ordered structures. Moreover, we also used the mixed self-assembly technique where we immersed the sample with nanosandwiches into the mixture of polymer and biotin solution in order to anchor polymer structures chemically on the surface. After obtaining the biotinylated surface via the SAMs method, streptavidin biomolecule is bounded to the surface through the head group of its specific ligand, biotin. The binding of these polymers and biomolecules are characterized by the AFM and XPS techniques, as discussed below.

1.6 Atomic Force Microscopy (AFM)

Atomic Force Microscopy (AFM) is a form of scanning probe microscopy (SPM) which operates by scanning the surface atoms by a pointed tip mounted on the cantilever. AFM is a powerful method to obtain 3D (x, y, z directions) high resolution images of all kinds of surfaces (such as polymers, adsorbed molecules, fibres, films etc.) at the atomic scale by using force interaction between surface and the tip of the microscope. These images can be obtained in air, in liquid or in vacuum. AFM also allows measuring the topography of the samples and roughness of the surfaces (Blanchard, 1996).

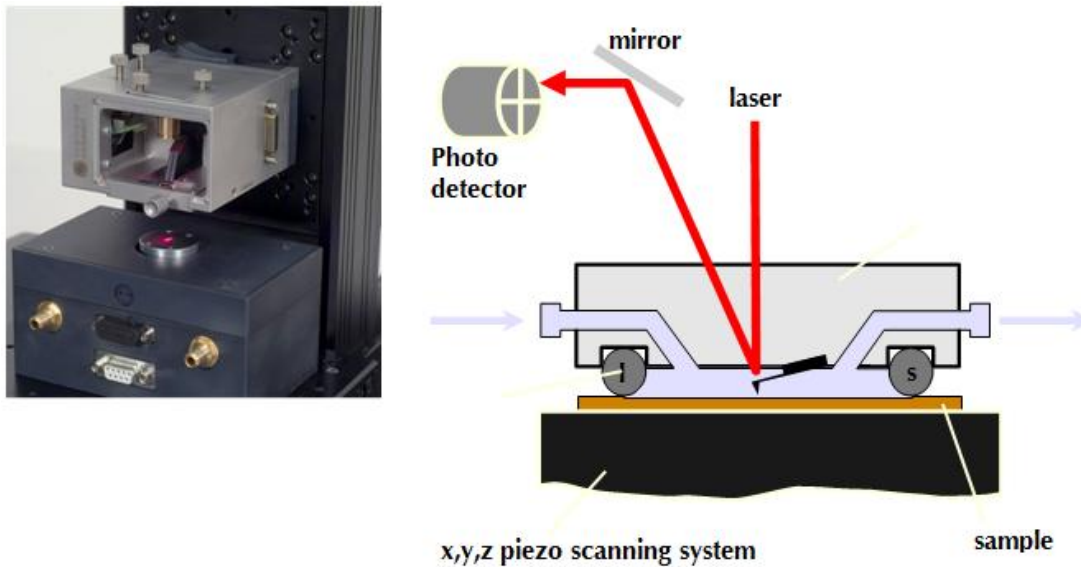


Figure 1.6 : AFM image from Nanomagnetic Instruments.

There are three modes of AFM that allows scanning different types of surfaces. In the contact mode, the tip touches the smooth surface with short range repulsive forces that allow atomic resolution. In the non-contact mode, on the other hand, the tip applies force without touching the surface. It can be used for all kinds of surfaces, but especially it is preferred for soft samples due to lack of degradation effects (Takahashi et al., 2002). Finally, the tapping mode of AFM, which is used in our study, basically refers to the scanning the surface with the resonance frequency that results from the oscillation of cantilever. Tapping mode and non-contact mode are similar to each other except the difference in the type of tips (Shiraki et al., 2006).

1.7 X-Ray Photoelectron Spectroscopy (XPS)

XPS (X-Ray Photoelectron Spectroscopy) is one of the most effective techniques for analyzing surface structures. It was introduced by Kai Sieghban and his research group in 1961 at University of Uppsala, Sweden; and originally named as Electron Spectroscopy for Chemical Analysis (ESCA); while later mostly referred as XPS (Siegbahn et al., 1967). Prof. Sieghban received the Nobel Prize in 1981 for the development of this technique.

XPS is used to obtain information regarding the chemical, physical, and electrical properties of the surface structures (Ertas and Suzer, 2006). It gives us the information regarding chemical state of the surface by measuring the binding energies of the emitted electrons from different kinds of elements (Wagner et al.,

1990). For example, XPS allows us to control the charging of the surfaces, which in turn helps us understand the electrical potential of the surfaces, such as their capacitance values.

1.7.1 Principles

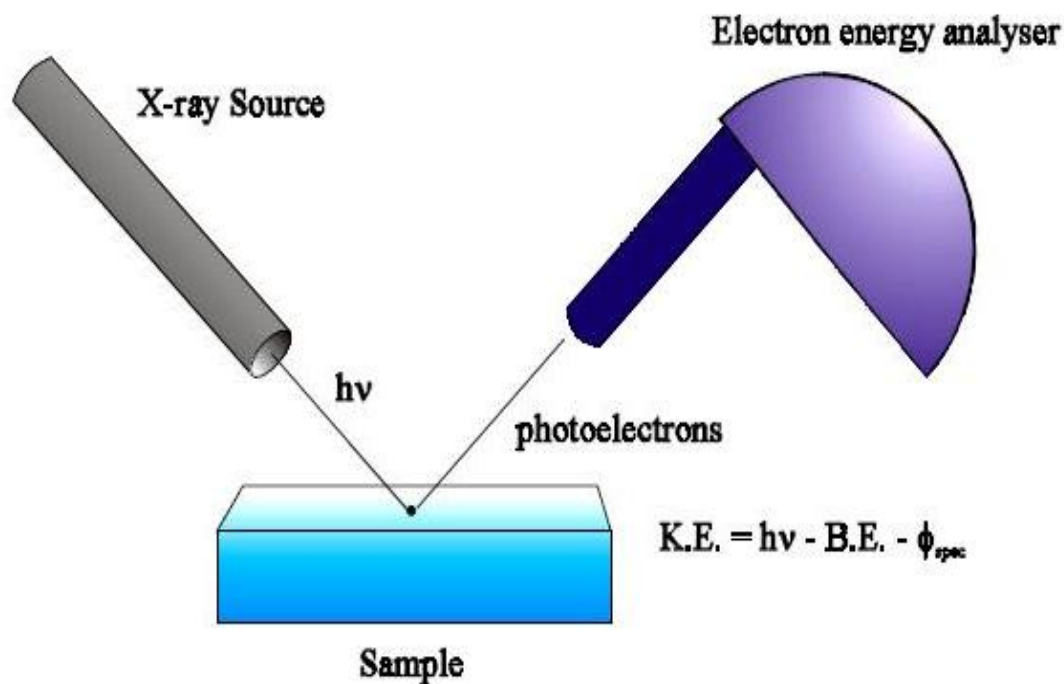


Figure 1.7 : Schematic illustration of the working principle of X-Ray Photoelectron Spectroscopy

Figure 1.7 illustrates the main components and working principles of an XPS experiment. Through a photoelectric effect, the photons coming through the X-ray source interact with the atoms on the surface, extracting electrons from the sample. The kinetic energies of the photoelectrons emitted from the surface are determined by an electron energy analyser, and given by the following formula:

$$KE = hv - BE - \phi \quad (1.1)$$

KE is the kinetic energy of the electrons extracted from the surface; BE is the binding energy; hv is the energy of the photons coming from the X-ray source; and ϕ refers to a work function.

1.7.2 Applications

XPS has wide range applications in areas such as elemental identification, chemical identification, and quantification.

1.7.2.1 Elemental identification

Elemental identification by XPS is possible through analyzing the binding energy values of the photoelectrons that are emitted from the surface as depicted in Figure 1.8. Each element has a specific binding energy value, which helps us to recognize the element by looking at the peak positions on the survey spectrum. The only exception to this rule is Hydrogen and Helium atoms (Kerber et al., 1996). The binding energy values that we obtain from XPS not only help us identify unique elements; but also give us information regarding the orbital of atoms. For instance, the peak around 133 eV is associated with 2p level of the P; while 402 eV is associated with 1s level of N, 17 eV corresponds to 4f level of Hf, and 336 eV is associated with 4d⁵ level of Au on the XPS spectrum as shown in Figure 8.

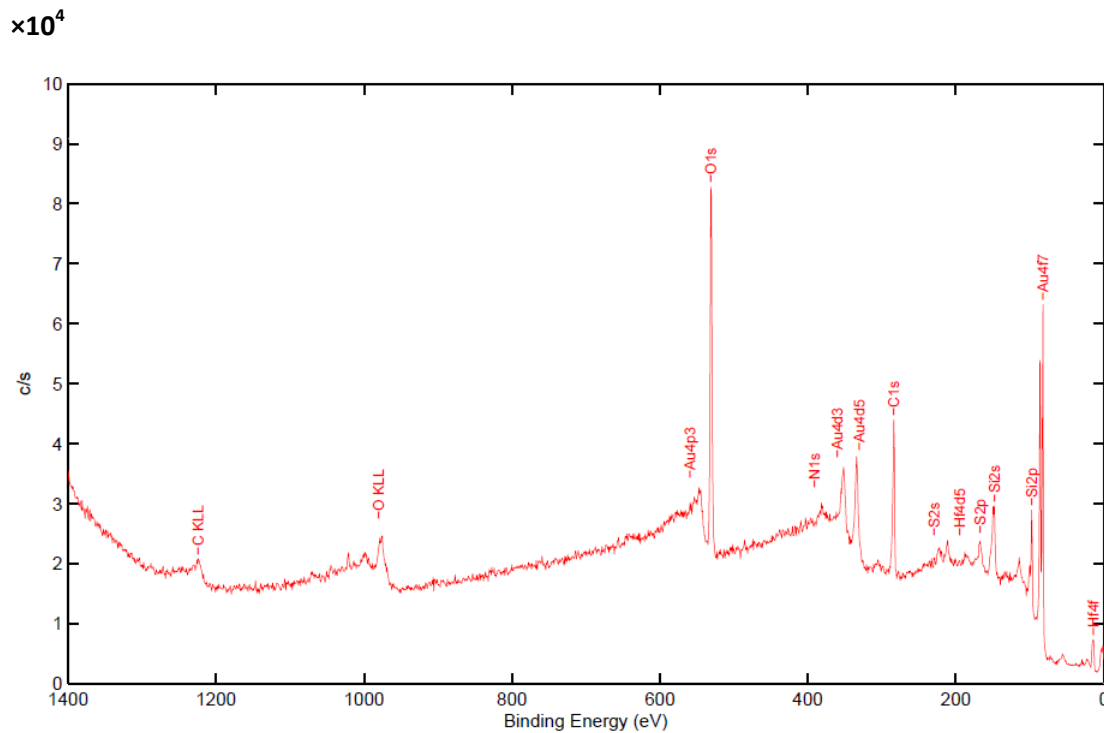


Figure 1.8 : XPS survey spectrum of S₂ATES+PDS on the silicon surface

The survey spectrum is basically a plot of electron binding energy values versus the intensity of the photoelectrons in 0-1400 eV interval (Wagner, 1979). The spectrum on Figure 1.8 shows a survey scan data which can help us to understand the unknown elements on the sample surface.

1.7.2.2 Chemical state identification

While analyzing the surface structures, XPS technique also helps us identify the chemical state of the atoms on the surfaces. Chemical state identification gives us the elemental and chemical composition of the surface structures (Karabudak et al., 2006). The chemical compositions of the molecules on the surface are determined by how the elements are bounded to the surface, which can be monitored by using the XPS spectra. The value of binding energy of atoms of the same element may sometimes shift to higher or lower binding energy levels (chemical shifts) due to reasons such as oxidation, charging etc. (Nikitin et al., 2005). Through detailed scans of the elements by XPS, separate multiple peaks can be understood to be linked to different chemical bonding states (Guittet et al., 2001), (Endo et al., 2001).

1.7.2.3 Quantification

There are two quantification methods for XPS analysis, the qualitative and quantitative analysis. The qualitative analysis involves the elemental and chemical identification of the surfaces, as mentioned in the previous sections. On the other hand, the quantitative analysis refers to the calculation of the height and area of the peaks of the analyzed atoms on the surface, within the 1-20 nm thickness range of the species by using the following formula (Briggs et al., 1995):

$$\frac{[C]_x}{[C]_y} = \frac{A_x \sigma_Y}{A_Y \sigma_X} \left(\frac{E_y^k}{E_x^k} \right)^{3/2} \quad (1.2)$$

In this formula, the kinetic energy of the photoelectron peak is given by E^k , while the area of the photoelectron peak is A , and σ refers to the cross-section of the atom's orbital. Using this formula, we can find information regarding the molecular configuration and functional groups of the surfaces.

1.7.3 Charging and Discharging in XPS

One of the great uses of XPS is also it helps us understand the charging discharging properties of materials (Suzer and Dâna, 2006) and control the charging on the surface. During the emission of photoelectrons through the electron analyzer, a

positive charge accumulation on the samples can be observed in the XPS analysis. While this surface charging (differential charging) has been identified as problematic due to resulting in inaccurate measurement of binding energies, this nuisance can be used in a beneficial way as it also enables us to extract additional information regarding electrical, physical, and structural properties of the samples (Briggs et al., 1995), (Lau and Wu, 1991), (Gouzman et al., 2006).

Through internal and external interventions, the charging and discharging properties of the surface can be controlled for obtaining electrical and analytical information. For instance, by applying external voltage to the sample, charging-discharging at certain frequency intervals can be observed, which gives us information about electrical parameters such as capacitance and resistance (Suzer and Dâna, 2006), (Dane et al., 2006).

There have been various application areas of differential charging properties of surfaces in the literature. For example, (Lau and Wu, 1991) used surface charging technique with XPS to produce dielectric-semiconductor structures and measured electrical properties of these structures using charging effects. In another study, (Havercroft and Sherwood, 2000) showed the chemical differences between the samples consisting of oxide films by applying d.c. negative biases to the samples. By using the differential charging, they were able to estimate the differences in oxide thickness between aluminum and magnesium regions.

(Karabudak et al., 2006) observed twin peaks on different energy levels on the surface while applied ± 10 square pulses to the conducting samples such as Silicon Oxide layer using XPS spectrum. The differential charging of the surface increase and decrease the binding energy values correspondingly. Thus, the dielectric properties of the surface are extracted in a non-contact fashion by using the differential charging of the surface structures. Similarly, (Suzer et al., 2007) show that by applying an external voltage to the samples under XPS recording of the data, the contrast in the charging of different domains enable them to differentiate the existence of chemically and electrically different domains in composite samples. By using differential charging, (Suzer, 2003) separated the phase of PDMS layer from the phase of SiO_2/Si substrate in order to obtain information on the dielectric properties of the composite layers. (Dane et al., 2006) demonstrated in detail how the

calculate the resistance and capacitance measurements of surface structures by using XPS.

In addition to these studies, differential charging is also used in past studies for studying specific polymers and thin films for detecting their electrical and physical properties. (Sezen et al., 2007) studied thin (10-50 nm) PS/PMMA polymeric materials by applying external bias with different frequencies for characterized phase-separation of the thin films. By using differential charging, electrical properties of polymeric materials (tacticity, packing, crystallinity, and effect density etc) can be detected. (Gouzman et al., 2006) used differential charging to characterize the self-assembled films grafted on multilayers of ODPA on stainless steel and glass substrates, and monolayer of ODPA on silicon. (Johnson and Levicky, 2004) analyzed the poly((mercaptopropyl)methylsiloxane) (PMPMS) to reveal the surface coverage with XPS through differential capacitance measurements. These past studies show that charging and discharging properties of surfaces can be used to extract electrical properties of the organic inorganic and polymeric materials.

The aim of this study is to use the differential charging properties of Au/Al₂O₃/Au and Au/HfO₂/Au nanosandwich structures by applying external voltage bias under different frequencies while recording XPS data, to measure the capacitance value of these nanostructures in order to obtain capacitance-based biosensors. To our knowledge no previous study has investigated the use of metal/insulator/metal nanostructures as capacitors for biosensor applications.

2. EXPERIMENTAL SECTION

2.1 Preparation of Nanostructures

It has been known that lithography techniques help fabricate arrays of metal/insulator nanostructures. Among lithography techniques, NSL is a simple and inexpensive method for fabrication of periodic arrays (Deckman and Dunsmuir, 1983). In our study, NSL technique is used to obtain nanostructures on silicon substrates. Silicon species of 1cm × 1cm are cleaned with piranha solution at 65 °C for 30 minutes, and the surfaces are rinsed with DI water and absolute ethanol and dried with nitrogen gas. Various polystyrene particles that is found as a suspension in water with 0.5 and 1 micron sizes were used in this study. And these particles are diluted in (1:400 v/v) triton X-100/methanol before spin coating. For each experiment, a mixture of 10 microliter particles to 60 microliter surfactant was used and then this mixture was sonicated for 30 minutes. 10 microliter nanoparticle drops was spin coated on Si(111) substrate.

The schematic illustration shows at below how the nanosandwich arrays were prepared by NSL.

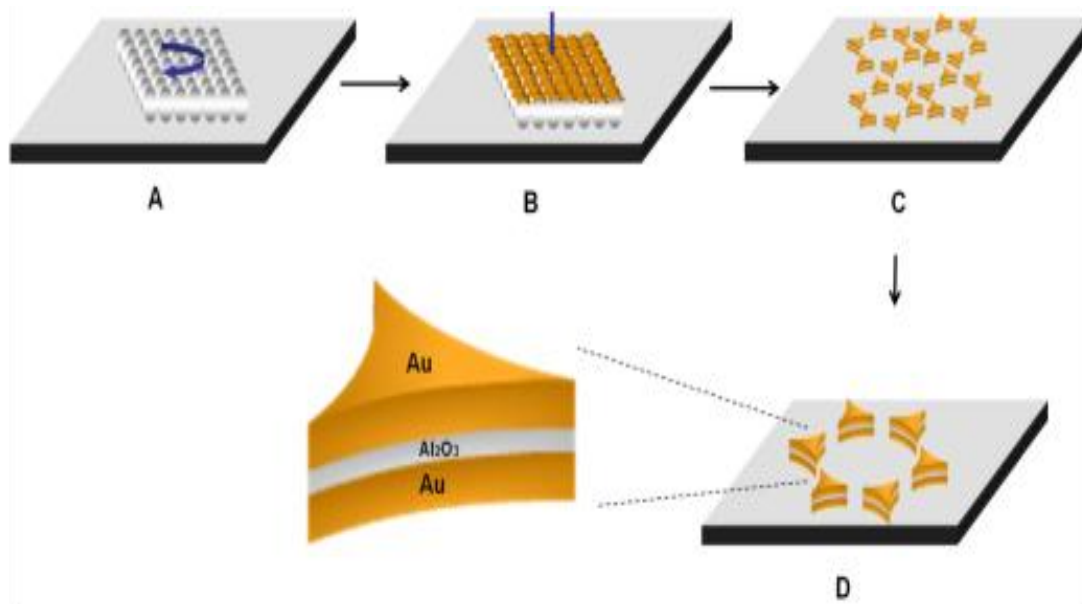


Figure 2.1 : Schematic illustration of the general process of the preparation of the nanosandwich arrays by Nanosphere Lithography (NSL) **(A)** Spin coating of polystyrene beads, **(B)** Metal deposition, **(C)** Lift off, **(D)** Single hexagonal nanosandwich array (Zareie et al., 2008b).

First, polystyrene particles were spin coated on the silicon substrate. Then, the substrate is top-coated with Au/ Al₂O₃/ Au or Au/ HfO₂/ Au layers. Au/Al₂O₃/Au thin film layers were deposited on Polystyrene particles on the Si surface by using high vacuum DC and RF magnetron sputtering (Lindgren et al., 2003), (Carcia et al., 2003). Then, as can be seen in step C, the Nano sphere mask was removed by sonication in dichloromethane for 2 minutes. Finally, the single hexagonal nanosandwich array was produced.

2.2 Functionalization of Nanosandwiches with Polymers

In this part, 3 different temperature-responsive polymers with functional end groups are used to functionalize the nanosandwiches. Three different copolymers with distinct LCST values (35°C, 40°C, and 45°C) were synthesized by a process called “the reversible addition fragmentation chair –transfer” (RAFT) technique (Boyer et al., 2009), (Huang et al., 2009). Each copolymer was designed to have a functional end-group that can bind to only one layer of the nanosandwich. More specifically, three different polymers have phosphoric acid ester, silane, and thiol end-groups to bind with Au/Al₂O₃/HfO₂, respectively.

Table 2.1 : Polymers end-groups vs. binding groups.

End group functionality	Layer
Phosphoric acid ester	Al ₂ O ₃
Silane	HfO ₂
Thiol	Au

2.2.1 Functionanalization phases

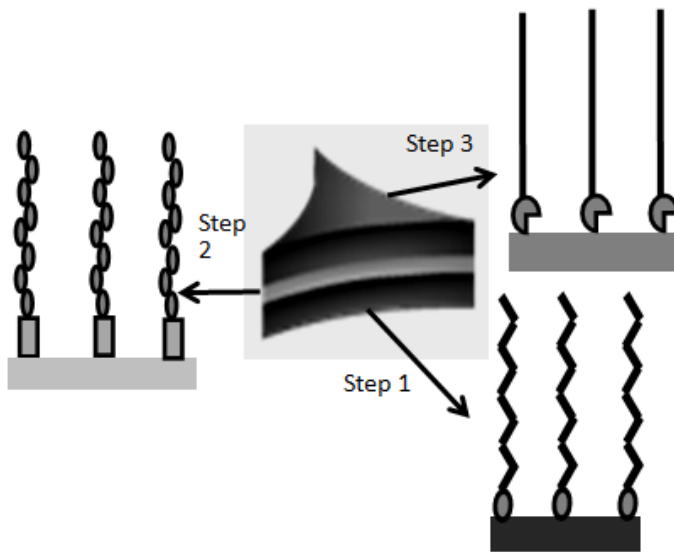
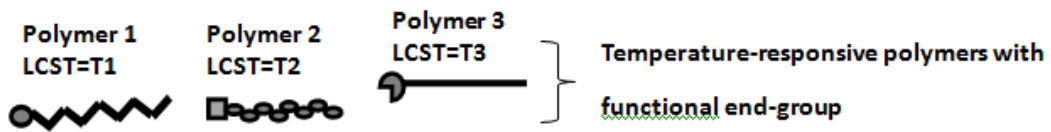


Figure 2.2 : Functionalization of a nanosandwich composed of three layers with temperature-responsive polymers (Tübitak Project 110T759)

So far, the production of the samples were described. The nine samples investigated in this study are shown in Table 2.2 and Table 2.3

Table 2.2 : The Production of the sample 1.

Sample	Substance
S₁	Nano sandwiches (20 nm Au/20 nm Al ₂ O ₃ / 20 nm Au) on Si surface
S_{1PHO}	with phosphate terminated polymer
S_{1PDS}	with thiol terminated polymer
S_{1PDS+PHO}	with thiol- and phosphate-terminated polymers
S_{1SA}	with streptavidin

Table 2.3 : The Production of the sample 2.

Sample	Substance
S₂	Nanosandwiches (20 nm Au/ 20 nm HfO ₂ /20 nm Au) on Si surface
S_{2PDS}	with thiol terminated polymer
S_{2ATES}	with silane terminated polymer
S_{2PDS+ATES}	with thiol- and silane-terminated

2.2.1.1 Binding of S_{PHO}

Phosphate is a functional end-group that can only bind on its specific metal layer, Al₂O₃. The phosphate terminated polymer was bound on the substrate with SAM technique as shown in Figure 2.3.

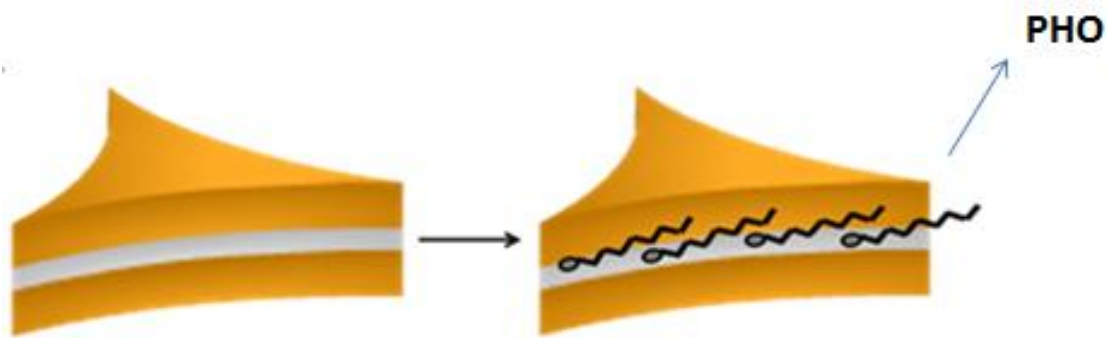


Figure 2.3 : Schematic illustration of the nanosandwiches before and after functionalization with phosphate-terminated polymer to Al_2O_3 layer (Tübitak Project 110T759)

First, the sample was incubated in 0.01 mM polymer solution in Ethanol for 24 hours. Then, the sample was taken out and rinsed with ethanol.

2.2.1.2 Binding of S_{PDS}

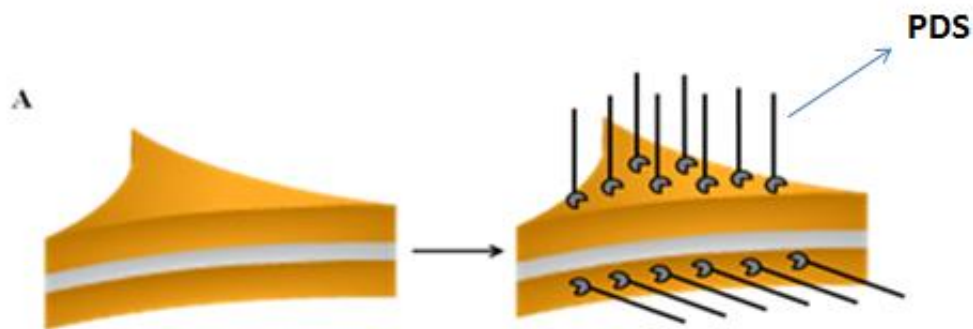


Figure 2.4 : Schematic illustration of the nanosandwiches before and after functionalized with thiol-terminated polymers to gold layers (Tübitak Project 110T759)

Figure 2.4 shows the functionalization of nanosandwiches with thiol-terminated polymers. The process is identical with the previous one. Thiol-terminated polymer was used for this sample. Thiol is a functional end-group that binds to its specific layer of Au through a chemical bond.

2.2.1.3 Binding of $S_{PDS+PHO}$

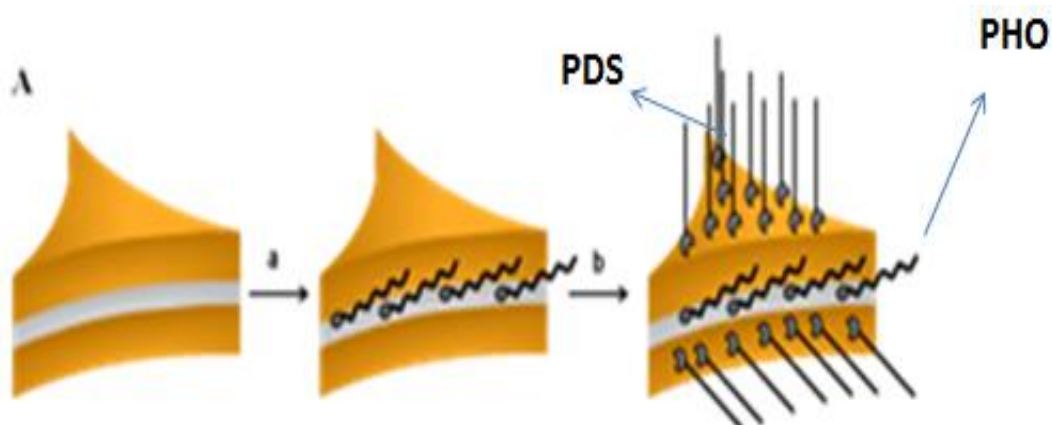


Figure 2.5 : Schematic illustration of the nanosandwiches before and after functionalized with phosphate and thiol-terminated polymers to their specific metal layers which are Al_2O_3 and Au, respectively (Tübitak Project 110T759)

This figure shows the functionalization of nanosandwiches with thiol and phosphate terminated polymers. The same technique was used as above.

2.2.2 Investigation of polymer phase transition on nanosandwich arrays

The goal in this step is to bind streptavidin (biomolecule) to nanosandwiches arrays functionalized with a mixture of thiol-terminated polymer with biotin. Biotin is a vitamin that has a very high and specific affinity towards Streptavidin protein, and widely used in nano-biotechnology applications (Boyer et al., 2009), (Gil and Hudson, 2004). The bio affinity binding of ligands (such as Streptavidin) to the receptor molecules (Biotin) on the nanosandwich surfaces is performed by increasing the temperature of the solution above the LCST of each polymer assembled on the surface. This allows the polymer chains to collapse at the critical temperature and allow only the receptor molecules to bind their specific ligands

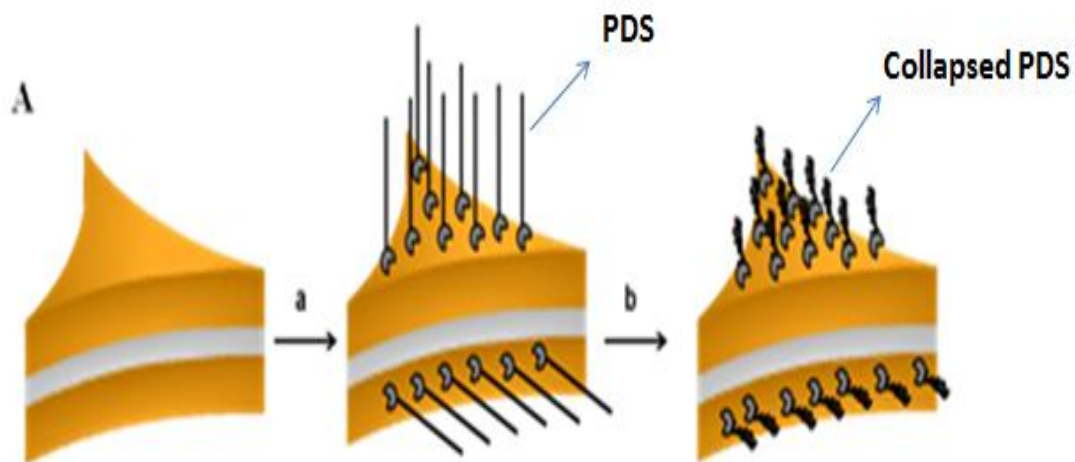


Figure 2.6 : (A) Schematic illustration of the functionalized nanosandwich arrays with thiol terminated polymer above the LCST. (a) unfunctionalized and (b) functionalized nanosandwich arrays with thiol terminated polymer at below LCST (25 ° C) and (c) above LCST (45 ° C) (Tübitak Project 110T759)

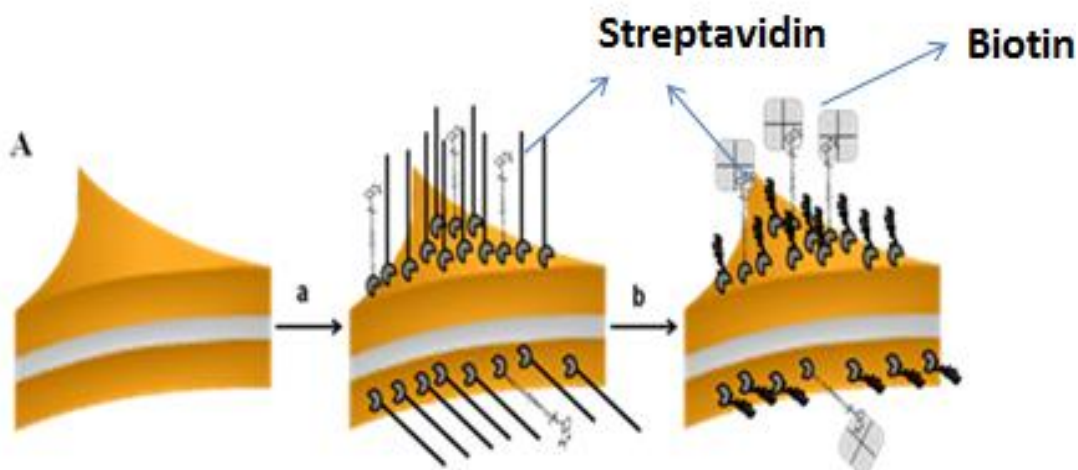


Figure 2.7 : (A) Schematic illustration of mixed SAM functionalized nanosandwiches and streptavidin detection above the LCST (Tübitak Project 110T759)

The nanosandwiches were incubated with 0.01 mM (9:1) thiol terminated polymer/EZ-link biotin below the LCST polymer (25°C). After incubation, the polymers were heated above LCST (45°C). Then the temperature-responsive polymers in the mixed SAM are collapsed, allowing the Streptavidin to bind to Biotin part.

2.3 Charge-Contrast XPS

As briefly mentioned in the introduction part, our goal is to show that nanosandwiches have capacitance properties at specific frequencies. Capacitance measurements of nanosandwich structures have not been reported in the literature as a possible transduction mechanism for the detection of biological binding events. In this section, the experimental setup was explained and how samples have been tested by using the Perkin Elmer PHI 5600 ESCA System.

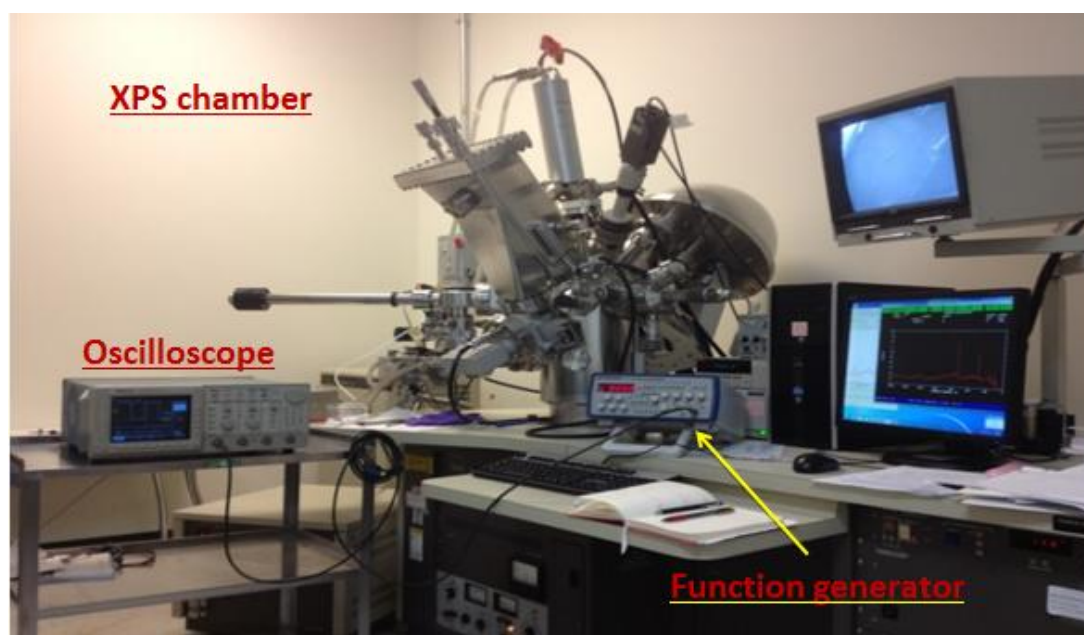


Figure 2.8 : Experimental Setup

For these experiments, an oscilloscope and a function generator were used as well as XPS. The samples mentioned above were loaded into the XPS chamber through a load lock chamber equipped with a transfer arm. The base pressure in that small introduction chamber was 10^{-8} Torr after a 10 minutes pumping with a turbo pump. After introducing the sample in the UHV main chamber, the base pressure was back into the 10^{-10} Torr range within 5 minutes and remained stable during data acquisition. For each sample, a survey scan was taken with the sample grounded (without applying any voltage). To avoid surface charge effect due to the produced photo-electrons, the flood gun was turned on, showering the sample with very low energy electrons. Then, scans were recorded, focusing the specific energy range of the different species present on the sample: 265-305 eV for C1s, 515-550 eV for

O1s, 80-120 eV for Si2p, 65-105 eV for Au4f. During those scans, different frequencies ranging from 0.1 Hz to 250kHz (specifically: 0.1 Hz, 150kHz, 160, 170, 180, 185, 190, 195, 200, 210, 220, 230, 240, 250 kHz) were subsequently applied to the sample using a square-wave-generator (SQW) with an amplitude of $\pm 10V$ (samples 1, 2 and 3). The amplitude of the signal at each frequency was measured by using an oscilloscope (before connecting the SQW generator to the samples).

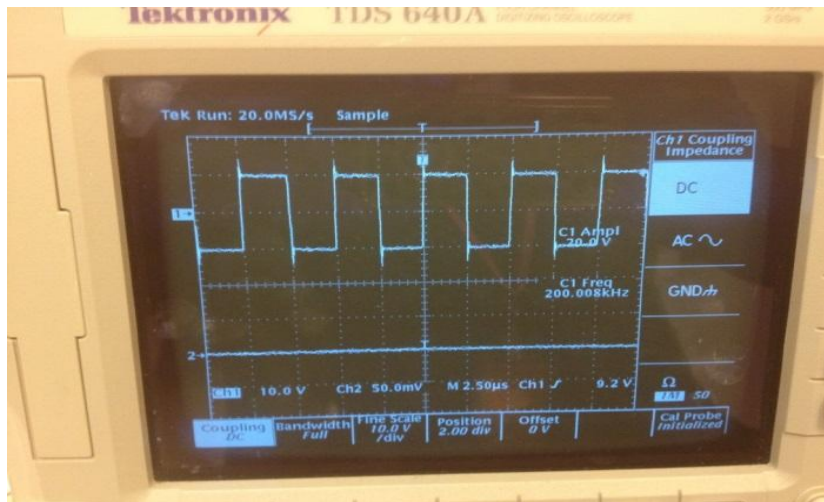


Figure 2.9 : Display of the oscilloscope showing the function delivered by the SQW function generator.

Before connecting the SQW generator to the samples, the signal frequency and voltage amplitude were measured by using an oscilloscope and set to the correct values with square wave generator.

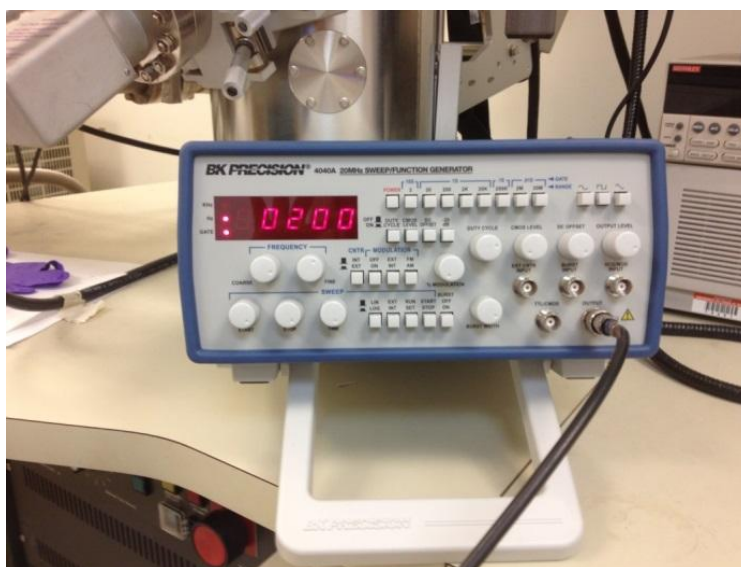


Figure 2.10 : SQW function generator

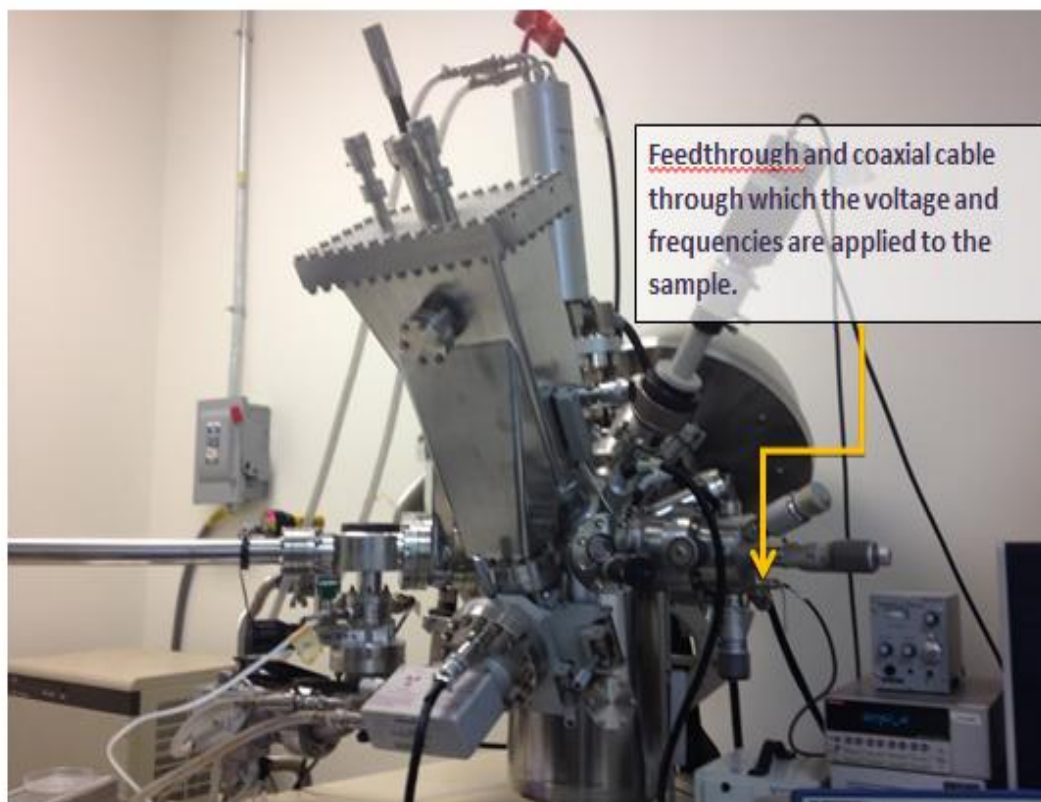


Figure 2.11 : SQW function generator connected to the sample through a UHV BNC connector located on the main XPS chamber

Next, the cable from the function generator was connected to the sample through a specific connector on the XPS chamber (in order to apply $\pm 10V$) for different frequencies.

2.4 External Resistance

In the previous part, the XPS data of nine nanosandwiches were taken by applying $\pm 10V$ with different frequencies in order to demonstrate capacitance properties of these nanosandwiches. After that, an RC circuit was used to understand and calculate the behavior of the samples' capacitance values.

In this section, a simple RC circuit was created by connecting an external resistance between function generator and XPS input as shown in Figure 2.12.

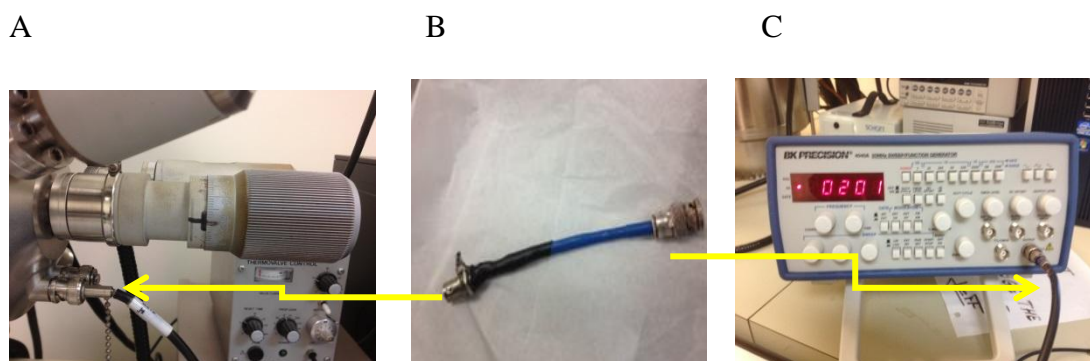


Figure 2.12 : The illustration of the external resistance between XPS input and function generator **A)** XPS input, **B)** $10\text{M}\Omega$ external resistance, and **C)** function generator

In figure 2.12, one side of the coaxial cable (B) of $10\text{M}\Omega$ external resistance was connected to the input of the XPS (A) and the other side of the cable was connected to the function generator (C) under $\pm 10\text{V}$ SQW pulses with different frequencies (while the flood gun was turned on). Then, the nine samples were analysed one more time by using XPS while applying $\pm 10\text{V}$ SQW pulses and $0.1\text{ Hz} - 10\text{ kHz}$ frequencies by connecting a $10\text{M}\Omega$ external resistance between the samples and function generator.

3. RESULT AND DISCUSSION

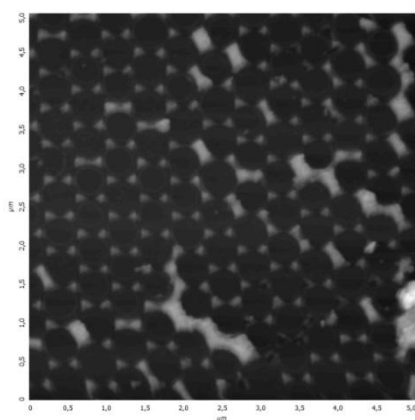
3.1 AFM Analyses of Nanosandwich Arrays Before And After Modification with Polymers

As mentioned in previous experimental section, nanosandwich arrays (20 nm/ 20 nm/ 20 nm Au/ Al₂O₃/ Au and Au/ HfO₂/ Au) were prepared by using nanosphere lithography (NSL). The obtained arrays of nanostructures were then functionalized with thiol, phosphate and silane terminated polymers and characterized with AFM and XPS techniques. The nanosandwich arrays were also functionalized with polymer and biotin mixture for controlled binding of streptavidin and monitored with AFM and XPS analyses to validate them.

In this section, the nine samples of nanodot arrays before and after treatment with polymers and biomolecules were analysed by using AFM in air. The tapping mode AFM images of the nanosandwiches and the corresponding height of the images were examined for nine samples as shown below respectively.

3.1.1 Au /Al₂O₃ /Au (20 nm /20 nm/ 20 nm) nanosandwiches without functionalization (S₁)

A



B

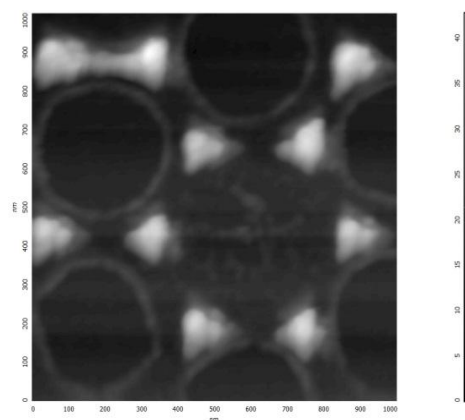
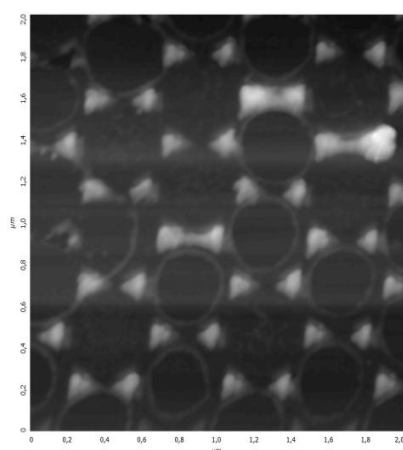


Figure 3.1 : Tapping mode AFM images of unfunctionalized nanosandwiches of Au/ Al₂O₃/ Au (20 nm/ 20 nm/ 20 nm) on Si substrate **A)** 5 μ ×5 μ , **B)** enlarged image of A (1 μ ×1 μ).

The AFM images of the unfunctionalized nanosandwiches of Au/ Al₂O₃/ Au layers were taken in tapping mode as shown at Figure 3.1. And, the average height of the AFM images were calculated from line profile as 55 nm. From Figure 3.1, some remained parts were observed due to the boundary of closed-packed polystyrene spheres. Rings can clearly be seen in the surrounding of unfunctionalized nanosandwichs arrays, which consists of the re-emission of Al₂O₃ from the center layer of triangular arrays.

3.1.2 Au / Al₂O₃/ Au nanosandwiches before and after functionalization with PHO polymer

A



B

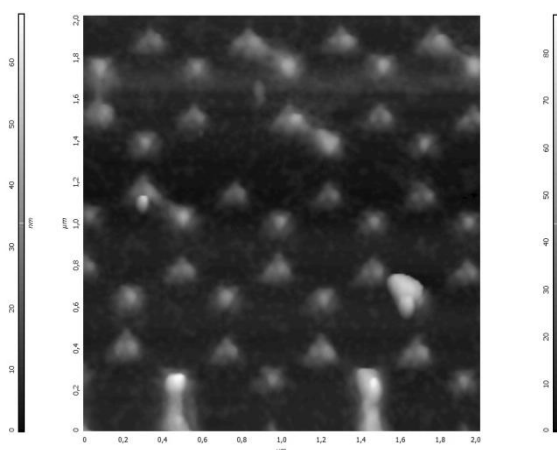


Figure 3.2 : Tapping mode AFM images of A) functionalized (S₁) and B) phosphate- terminated polymer functionalized (S_{1PHO}) nanosandwiches arrays on Si as represented at 2μ×2 μ.

The comparison of unfunctionalized and phosphate-terminated polymer functionalized nanosandwich arrays were depicted in Figure 3.2 A and B, respectively. The heights of the AFM images were measured for unfunctionalized and functionalized nanosandwiches with line profile at AFM. The height of unfunctionalized nanosandwiches is 55nm, while the height of functionalized nanosandwiches is 58nm. The increase in the height shows that phosphate-terminated polymer is bound to the Al₂O₃ layer of nanosandwiches.

3.1.3 Au/ Al₂O₃/ Au nanosandwiches before and after functionalization with PDS polymer

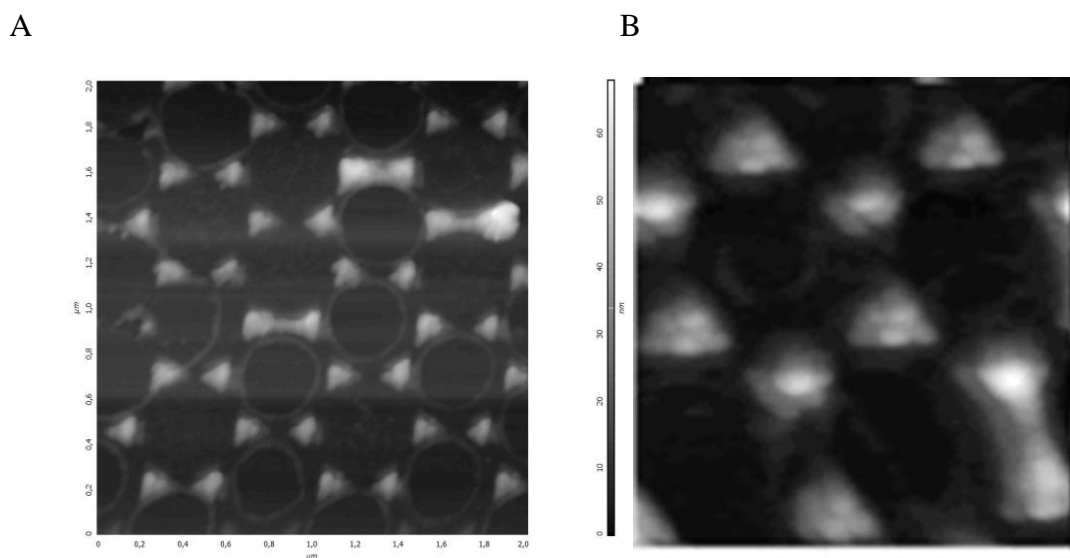
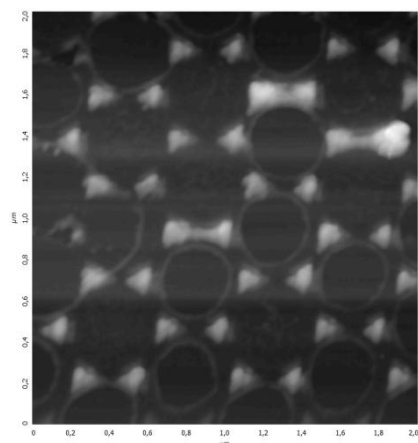


Figure 3.3 : Tapping mode AFM images of A) functionalized (S_1) and B) phosphate- terminated polymer functionalized (S_{1PDS}) nanosandwiches arrays on Si as represented at $2\mu \times 2\mu$ and $1\mu \times 1\mu$, respectively.

From Figure 3.3, the heights of AFM images were calculated with line profile for unfunctionalized and functionalized nanosandwiches with thiol-terminated polymer. The height of unfunctionalized nanosandwiches was 55 nm. After incubation with PDS polymers, the height of the Figure 3.3 B was measured 60 nm. The variation of the height was due to the PDS polymers binding on the Au layers of the nanosandwiches. Therefore, the binding of polymers to the Au layers were resulted in the triangles to adopt a more rounded shape.

3.1.4 Au/ Al₂O₃/ Au nanosandwiches before and after functionalization with PHO+PDS polymers

A



B

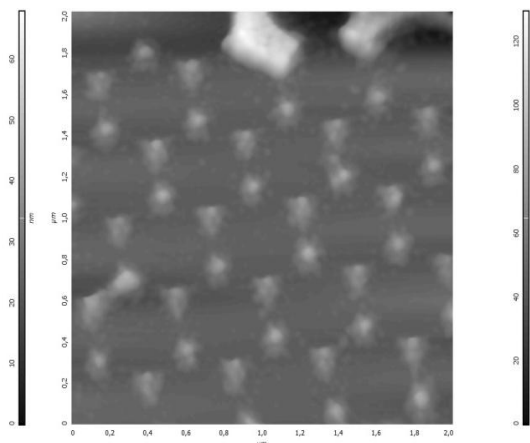


Figure 3.4 : Tapping mode AFM images of A) unfunctionalized (S_1) and B) phosphate- terminated polymer functionalized ($S_{1\text{PHO+PDS}}$) nanosandwiches arrays on Si as represented at $2\mu \times 2\mu$.

AFM images were taken and the heights of Figure 3.4 A and B were measured 55 and 64 nm for unfunctionalized and functionalized nanosandwiches, with phosphate and thiol-terminated polymers. As a result, the phosphate-terminated polymers were bound to Al₂O₃ layer near the nanodot arrays as shown in Figure 3.4 B. And, the thiol-terminated polymers were also bound the gold layers as a formation of S-Au covalent bound.

3.1.5 Au/ Al₂O₃/ Au nanosandwiches before and after functionalization with SA biomolecule

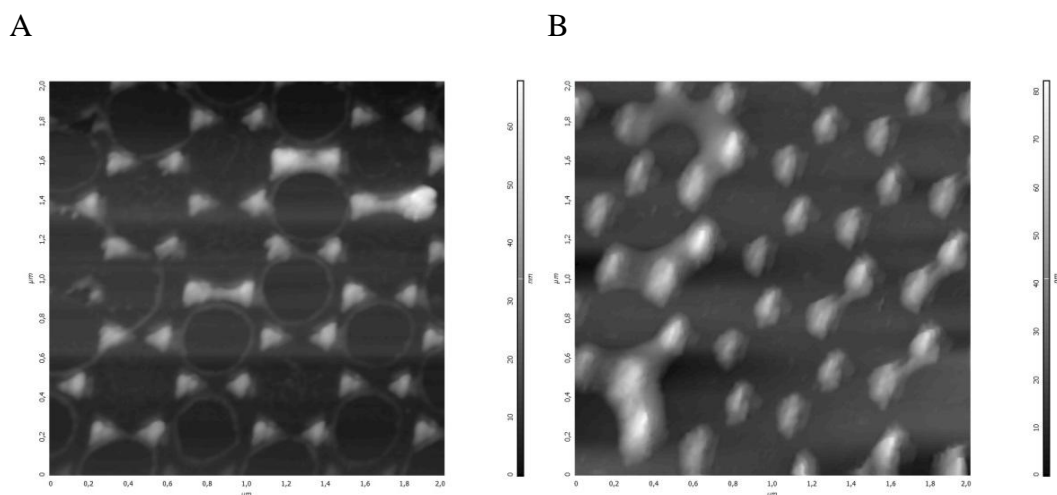


Figure 3.5 : Tapping mode AFM images of **A)** unfunctionalized (S_1) and **B)** functionalized with streptavidin biomolecule (S_{1SA}) above the lower critical temperature (LCST) of the polymer on nanosandwich arrays as represented at $2\mu \times 2\mu$.

AFM images were represented in Figure 3.5 A and B for unfunctionalized and after functionalized nanosandwiches arrays after modification with streptavidin biomolecule. After modification with streptavidin, the height of the unfunctionalized nanosandwiches increased from 55 nm to 66 nm. The polymer morphology changed depending on the temperature being below or above the LCST in order to bind SA molecules to biotin molecules. Streptavidin molecules were bound to gold layers as shown in Figure 3.5 B.

3.1.6 Au/ HfO₂/ Au (20 nm/ 20 nm/ 20 nm) nanosandwiches without functionalization (S₂)

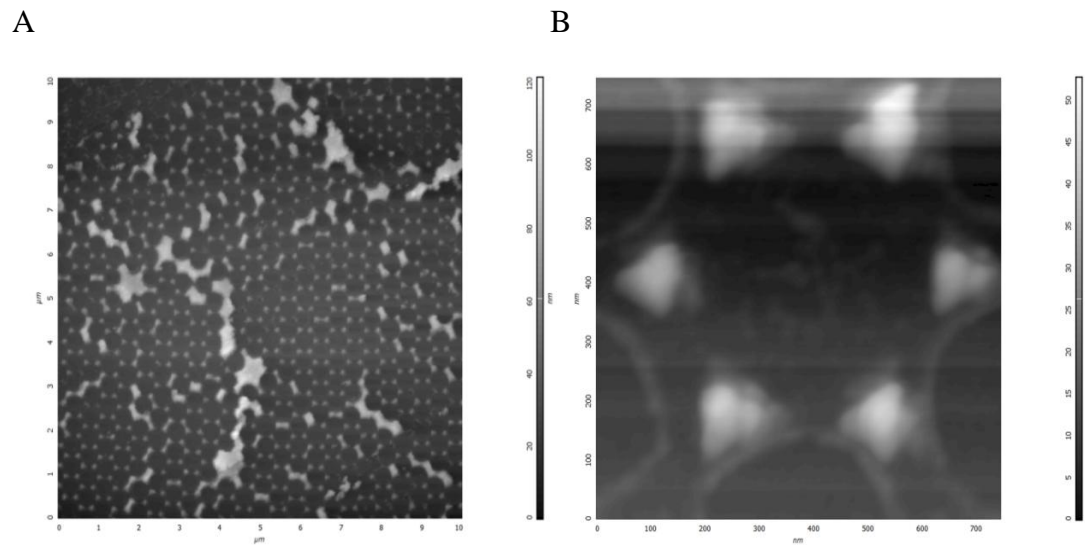


Figure 3.6 : Tapping mode AFM images of unfunctionalized (S₂) **A)** 10μ×10μ and **B)** enlarged image of A (0.7μ×0.7μ).

The remaining four samples which consist of Au/ HfO₂/ Au (20 nm/ 20 nm/ 20 nm) layers of nanosandwiches were analyzed by using AFM in tapping mode. In addition, the height of the Figure 3.6 of the unfunctionalized nanosandwiches was measured 54 nm. The height value was decreased 1 nm different from Figure 3.1 which is the AFM image of the unfunctionalized nanosandwiches of Au/ Al₂O₃/ Au layers. The variation was due to the HfO₂ metal between gold layers.

3.1.7 Au /HfO₂ /Au nanosandwiches before and after functionalization with PDS polymers

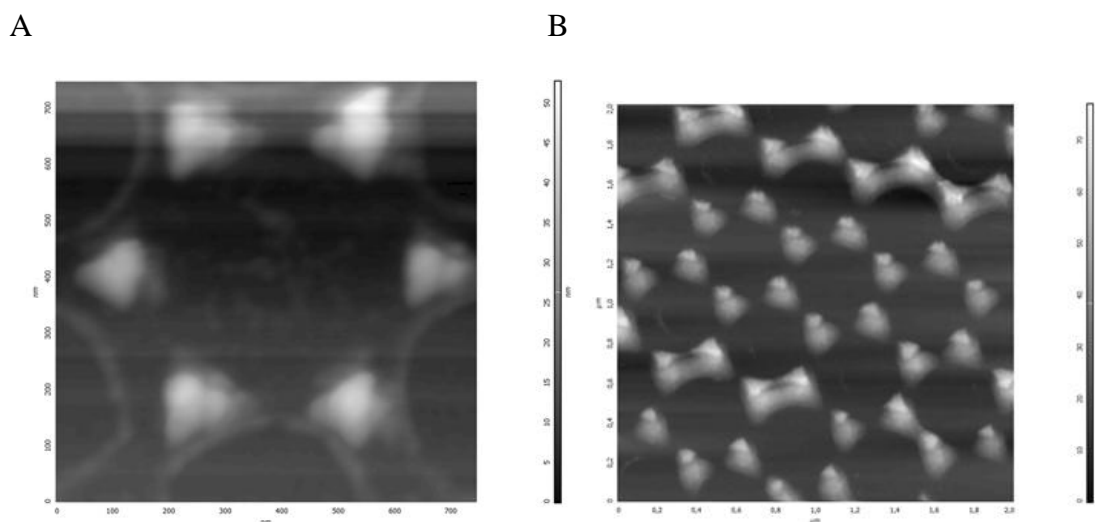


Figure 3.7 : Tapping mode AFM images of **A)** unfunctionalized (S_2) ($0.7\mu\times 0.7\mu$) and **B)** functionalized thiol-terminated polymers (S_{2PDS}) nanosandwiches arrays on Si as represented at $2\mu\times 2\mu$.

The AFM images of nanosandwich arrays (Au/ HfO₂/ Au) were taken before and after functionalization with thiol-terminated polymers. The heights of Figure 3.7 A and B were measured 54 and 59 nm from line profile in AFM. Therefore, thiol-terminated polymers were attached to Au layers.

3.1.8 Au /HfO₂ /Au nanosandwiches before and after functionalization with ATEs polymer

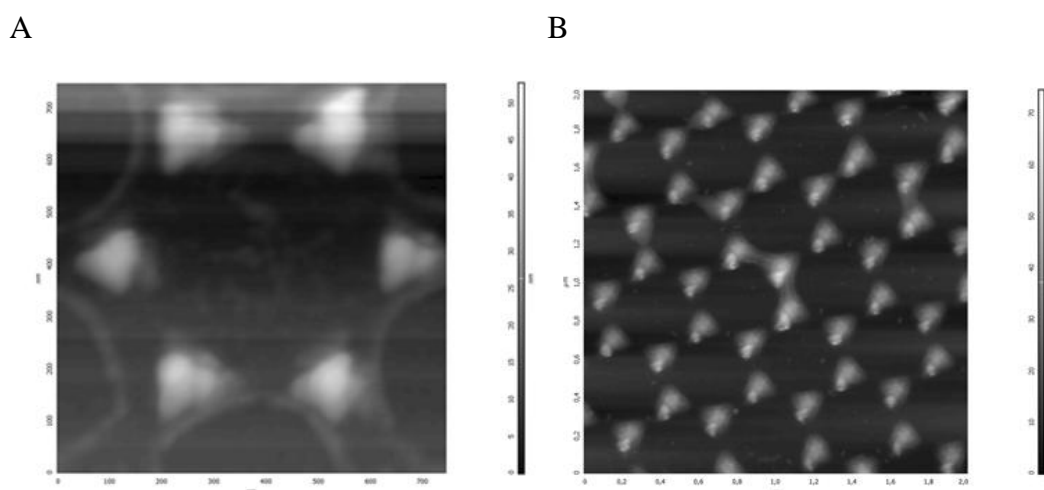


Figure 3.8 : Tapping mode AFM images of **A)** unfunctionalized (S_2) ($0.7\mu\times 0.7\mu$) and **B)** functionalized silane-terminated polymers (S_{2ATES}) nanosandwiches arrays on Si as represented at $2\mu\times 2\mu$.

The corresponding tapping mode AFM results are shown in Figure 3.8. Au/ HfO₂/ Au nanodots before functionalization were observed in the Figure 3.8 A with the height of 54 nm which was calculated from the line profile. On the other hand, Figure 3.8 B displays the image of the same nanodots after treatment with silane-terminated polymer with the height of 61 nm. From these AFM images and the heights of the nanosandwiches, it can be understood that the ATEs polymer was completely bound to the side of the hafnium layer in nanosandwiches.

3.1.9 Au /HfO₂ /Au nanosandwiches before and after functionalization with PDS+ATES polymers

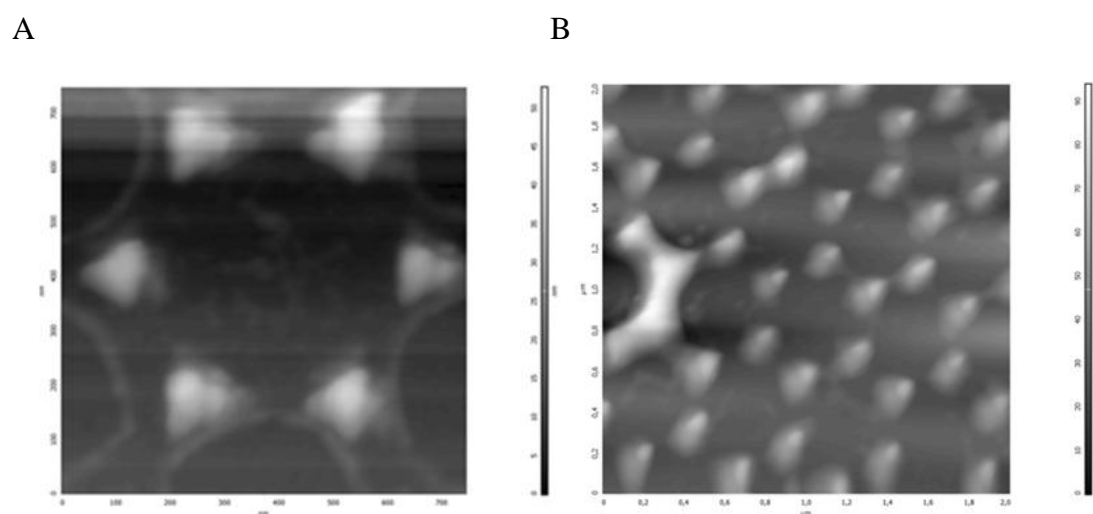


Figure 3.9 : Tapping mode AFM images of A) unfunctionalized (S_2) ($0.7\mu\times 0.7\mu$) and B) functionalized thiol and silane-terminated polymers ($S_{2PDS+ATES}$) nanosandwiches arrays on Si as represented at $2\mu\times 2\mu$

The tapping mode AFM images of Au/ HfO₂/ Au nanosandwiches before and after functionalization with thiol and silane-terminated polymers were displayed in Figure 3.9. The height of the images were calculated from line profile for Figure 3.9 A and B and found 54 and 65 nm, respectively. The increase in heights was brought about by the chemical binding of thiol and silane-terminated polymers to their specific layers of Au and HfO₂ in the nanosandwiches.

3.2 Survey Spectrum Measurement of Nanostructures With XPS

As briefly mentioned in the introduction section, a survey scan which includes energy peaks identifies the elemental composition of the analyzed surface. All the elements apart from hydrogen and helium are detected in the survey scan. (Wagner, 1979) The 9 wide survey scans below were taken with the samples grounded (without applying any voltage and frequency). These survey scans show the elements that are on the surfaces. Table 3.1 below shows the list of elements that were observed on the samples.

Table 3.1 : The binding energy values for Al, C, Au, Hf, N, O, P, Si, S elements.

ELEMENTS	ORBITALS	B.E (eV)
Aluminum	Al2p	69-87
	Al2s	114-132
Carbon	C1s	279-297
	C_KLL	1201-1239
Gold	Au4d3	345-363
	Au4d5	336-354
	Au4f	80-98
	Au4f7	81-99
	Au4p3	538-556
Hafnium	Hf4d	204-242
	Hf4d5	204-242
	Hf4f	10_28
	Hf4p3	373-392
Nitrogen	N1s	392-410
	N_KLL	1089-1121
Oxygen	O1s	524-542
	O_KLL	961-989
Phosphorus	P2p	124-142
	P2s	186-204
Silicon	Si2p	95-113
	Si2s	146-164
Sulfur	S2p	156-174
	S2s	223-241
	S_LMM	1321-1349

Survey spectra are useful in the identification of chemical states. (Wagner, 1979) Elements can be identified through a broad survey scan with X-Ray Photoelectron Spectroscopy (XPS). A survey scan ranging from 0 to 1400 eV energy scale is enough for the identification of the elements which are detectable. In this thesis, all the survey scans were recorded by using Al K α x-rays.

Nine samples have been tested using X-Ray Photoelectron Spectroscopy. Firstly, XPS survey spectra were recorded on Sample 1 (S1). Sample 1 (S1) consists of Nanosandwiches (20 nm Au/20 nm Al₂O₃/ 20 nm Au) on Si surface without functionalization. As shown in Figure 3.10, the spectrum contains 10 peaks. These peaks were identified in Figure 3.10 as C1s, C_KLL, O1s, O_KLL, Si2p, Si2s, Au4f7, Au4d5, Au4d3 and Al2s with binding energies of 284, 1225, 532, 986, 98, 161, 83, 341, 360 and 121 eV respectively. C_KLL and O_KLL spectral regions are Auger series. As explained in the introduction in detail, normally four Auger series are observable with XPS (Knop-Gericke, 2012) which are KLL, LMM, MNN and NOO (Wagner, 1979). In Figure 1, only the KLL series are observed which includes the initial vacancy in the K shell and final double vacancy in the L shell between Auger transitions (Van Grieken and Markowicz, 2001).

The wide survey scan shows the existence of gold, aluminum and oxygen on the silicon surface. Thus, it is demonstrated that our nanosandwiches were found on the surface covered with 20 nm Au/20 nm Al₂O₃/ 20 nm Au.

×10⁴

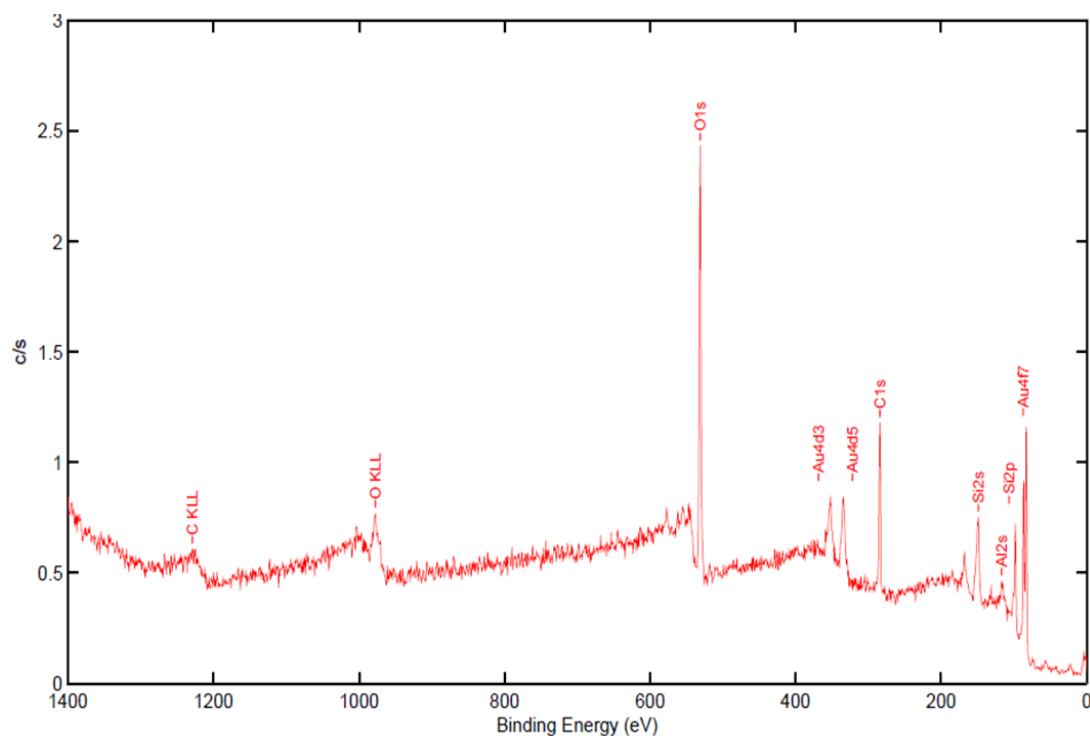


Figure 3.10 : Wide Survey Spectrum of Sample 1 (S₁)

Secondly, Sample 2 (S₁PHO) was analyzed by XPS which consists of nanosandwiches (20 nm Au/ 20 nm Al₂O₃/20 nm Au) on Si surface after functionalization with phosphate terminated polymer. From Figure 3.11 the survey scan includes 11 peaks which are C1s, C_KLL, O1s, O_KLL, Si2p, Si2s, Au4f7, Au4d5, Au4d3, Al2s and P2s. These peaks are comprised of 284, 1225, 532, 986, 98, 161, 83, 341, 360, 121 and 187 eV respectively.

Figure 3.11 shows the presence of the gold, aluminum, oxygen and phosphorus on the silicon sample. The existence of phosphorus in the survey scan indicates the binding of PHO polymer to the Al₂O₃ layer, as expected.

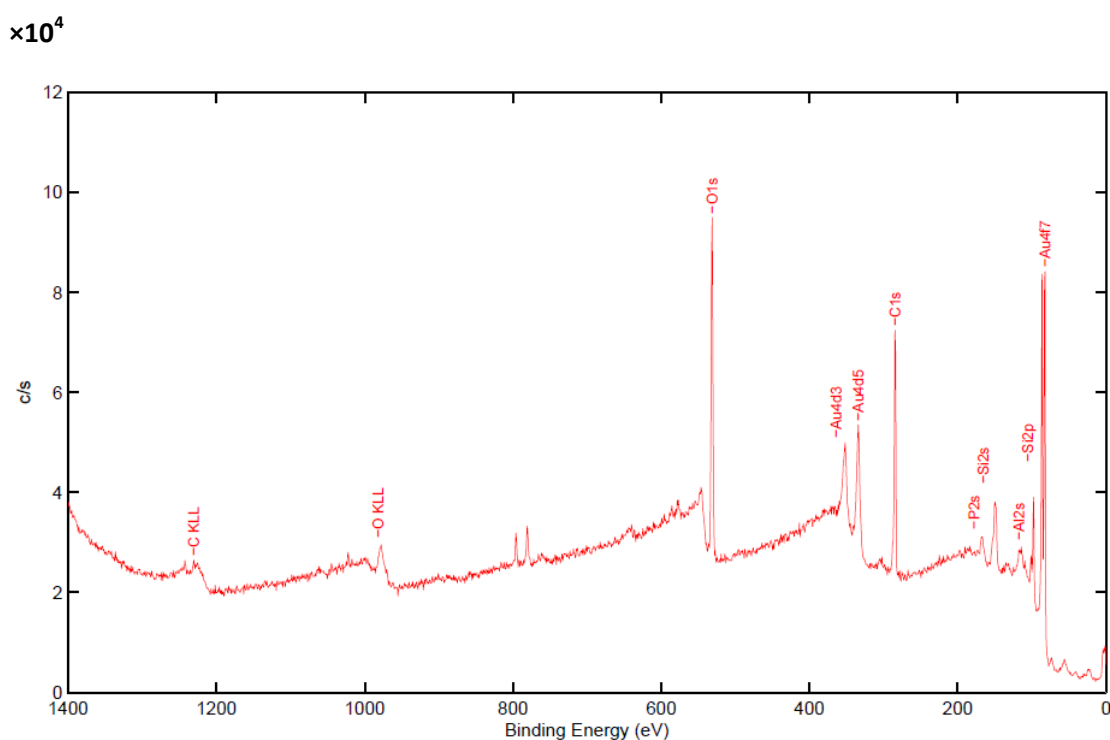


Figure 3.11 : Wide Survey Spectrum of Sample 2 (S₁PHO)

Thirdly, the survey scan was taken for Sample 3 (S₁PDS). This sample is comprised of nanosandwiches (20 nm Au/ 20 nm Al₂O₃/20 nm Au) on Si surface after functionalization with thiol terminated polymer. In Figure 3.12, 12 peaks can be identified for this sample, which includes the C1s, C_KLL, O1s, O_KLL, Si2p, Si2s, Au4f7, Au4d5, Au4d3, Al2s, S2p, S_LMM spectral regions. The corresponding binding energy values of these peaks were 284, 1225, 532, 986, 98, 161, 83, 341, 360, 121, 160 and 1345 eV. Figure 3.12 shows that Sample 3 (S₁PDS) includes C_KLL, O_KLL and S_LMM Auger series. Different from Sample 1, S_LMM

Auger series are also present in this sample. The LMM series were included during the initial ionization of 2p levels, and final vacancies were observed in the 3p or 3d shells (Wagner and Taylor, 1980).

Gold, alumina, oxygen and sulfur were observed clearly in Figure 3.12. This survey scan shows the sulfur element different from Figure 3.10. The presence of sulfur in the survey scan indicates the binding of PDS polymer to its specific layer (Au), as expected.

×10⁴

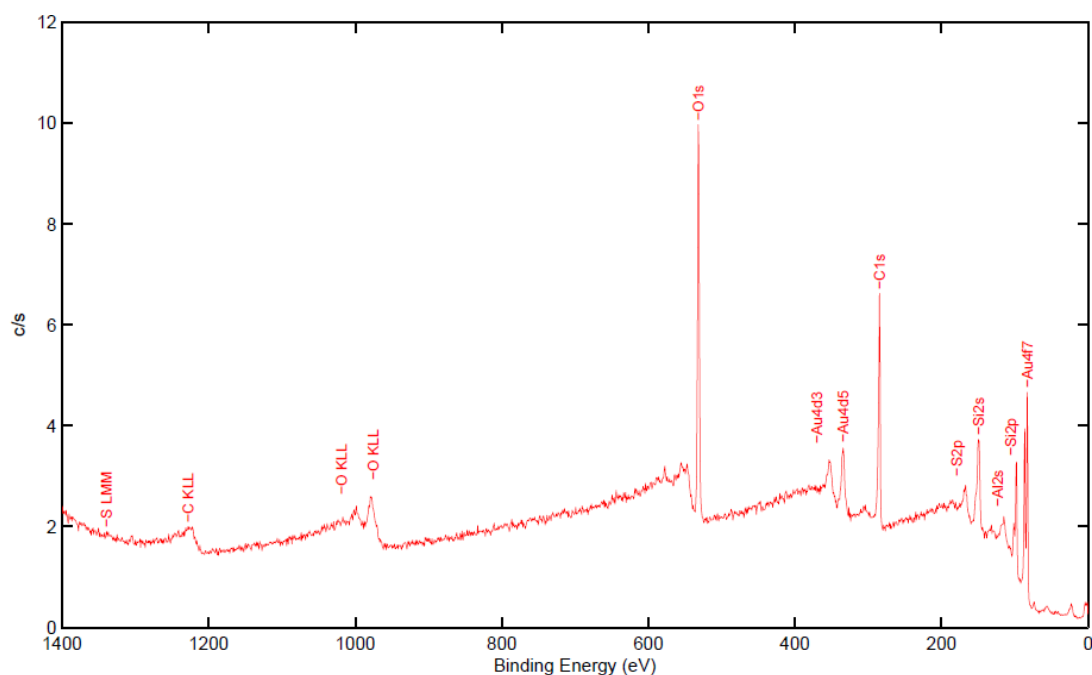


Figure 3.12 : Wide Survey Spectrum of Sample 3 (S1PDS)

Next, the survey spectrum was recorded for Sample 4 (S_{1PHO} + PDS). This sample consists of nanosandwiches (20 nm Au/ 20 nm Al₂O₃ /20 nm Au) on Si surface after functionalization with thiol- and phosphate-terminated polymers. As can be seen in Figure 3.13, this spectrum contains 11 peaks which are C1s, C_KLL, O1s, O_KLL, Au4f7, Au4d5, Au4d3, Al2p, S2p, S_LMM, P2p with binding energy levels of 284, 1225, 532, 986, 83, 341, 360, 73, 160, 1345 and 126 eV respectively.

Gold, alumina, oxygen, sulfur and phosphorus can be identified in Figure 3.13. The presence of sulfur and phosphorous in the XPS results indicates the PHO and PDS polymers were bonded to their specific Al₂O₃ and Au layers respectively.

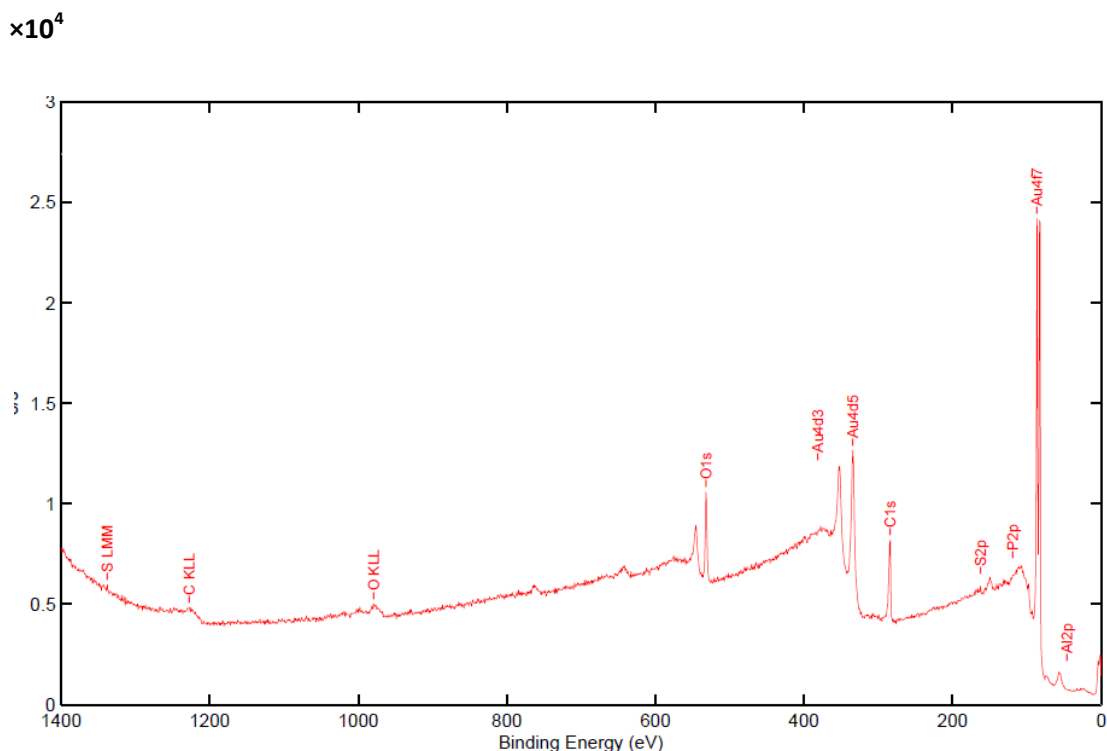


Figure 3.13 : Wide Survey Spectrum of Sample 4 (S_{1PHO+PDS})

Sample 3.14 (S_{1SA}) which contains the nanosandwiches (20 nm Au/ 20 nm Al₂O₃ /20 nm Au) on Si surface after functionalization with thiol end group polymers and streptavidin was analyzed by XPS. 14 peaks were identified in the spectrum, which are C1s, C_KLL, O1s, O_KLL, Si2p, Si2s, Au4f7, Au4d5, Au4d3, Al2s, S2p, S_LMM, N1s, N_KLL spectral regions with binding energies of 284, 1225, 532, 986, 98, 161, 83, 341, 360, 121, 160, 1345, 397, 1100 eV.

This wide survey scan reveals that the S_{1SA} includes gold, alumina, sulfur, nitrogen and oxygen on the silicon surface. As distinct from Sample 1, the detection of N and S elements on the surface shows that streptavidin biomolecule is bonded to the biotinylated nanosandwich. (Hyun et al., 2001) Since the biotin is a strong high affinity receptor ligand binding to the streptavidin (Savage, 1992), (Kaifer, 1992), the presence of biotin-linked reagents on the polymeric surface makes the surface attractive for the binding of streptavidin to the surface (Holmberg et al., 2005). From Figure 3.14, the elements which include N1s peak are offset by an appropriate constant to clarify the streptavidin-biotin interaction.(Hyun et al., 2001).

$\times 10^4$

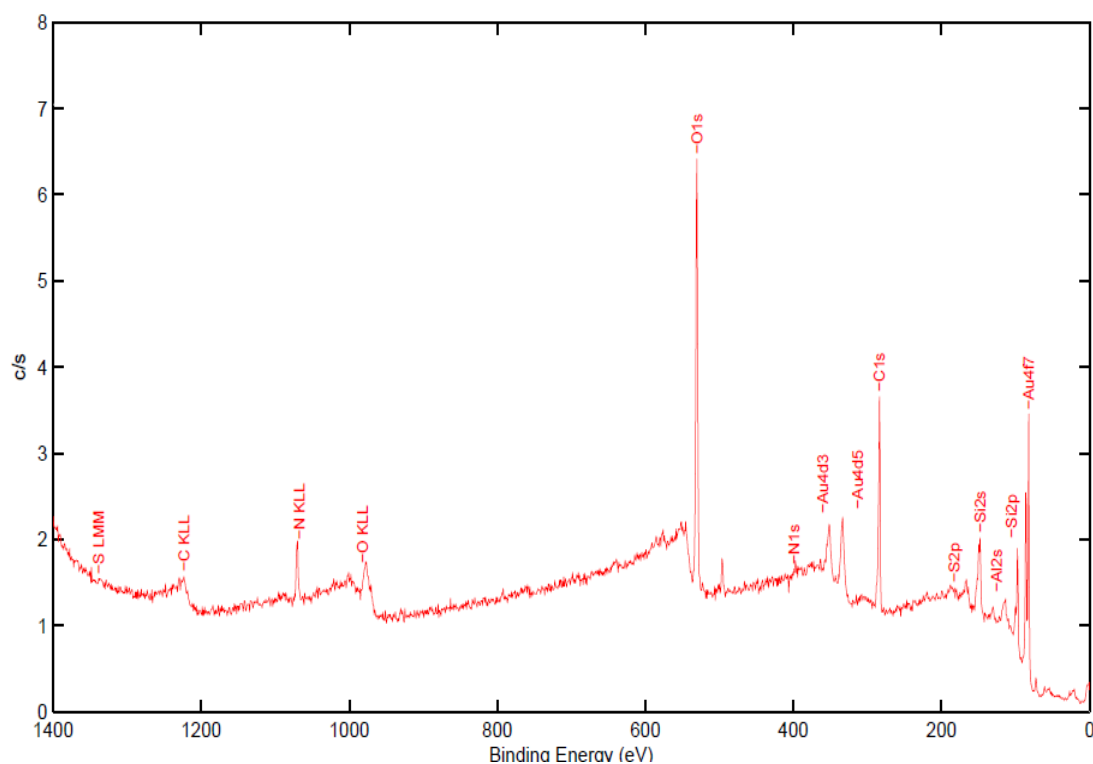


Figure 3.14 : Wide Survey Spectrum of Sample 5 (S_{1SA})

So far we have analyzed the samples with Au/ Al_2O_3 / Au nanosandwiches. In the remaining of the samples, we changed the middle layers of the nanosandwiches to HfO_2 layer, instead of Al_2O_3 . Sample 6 (S_2) consists of nanosandwiches (20 nm Au/ 20 nm HfO_2 /20 nm Au) on Si surface without functionalization. The wide survey scan was recorded for this sample. 13 peaks were identified (C1s, C_KLL, O1s, O_KLL, Au4f7, Au4d5, Au4d3, Si2s, Si2p, Hf4f, Hf4d5, Hf4p3 and Hf4p1) with binding energies of 286, 1225, 532, 986, 98, 161, 83, 360, 341, 14, 216, 391 and 425eV respectively.

From spectrum this sample contains gold, hafnium and oxygen which indicated that nanosandwiches (Au/ HfO_2 /Au) exist on the Si surface.

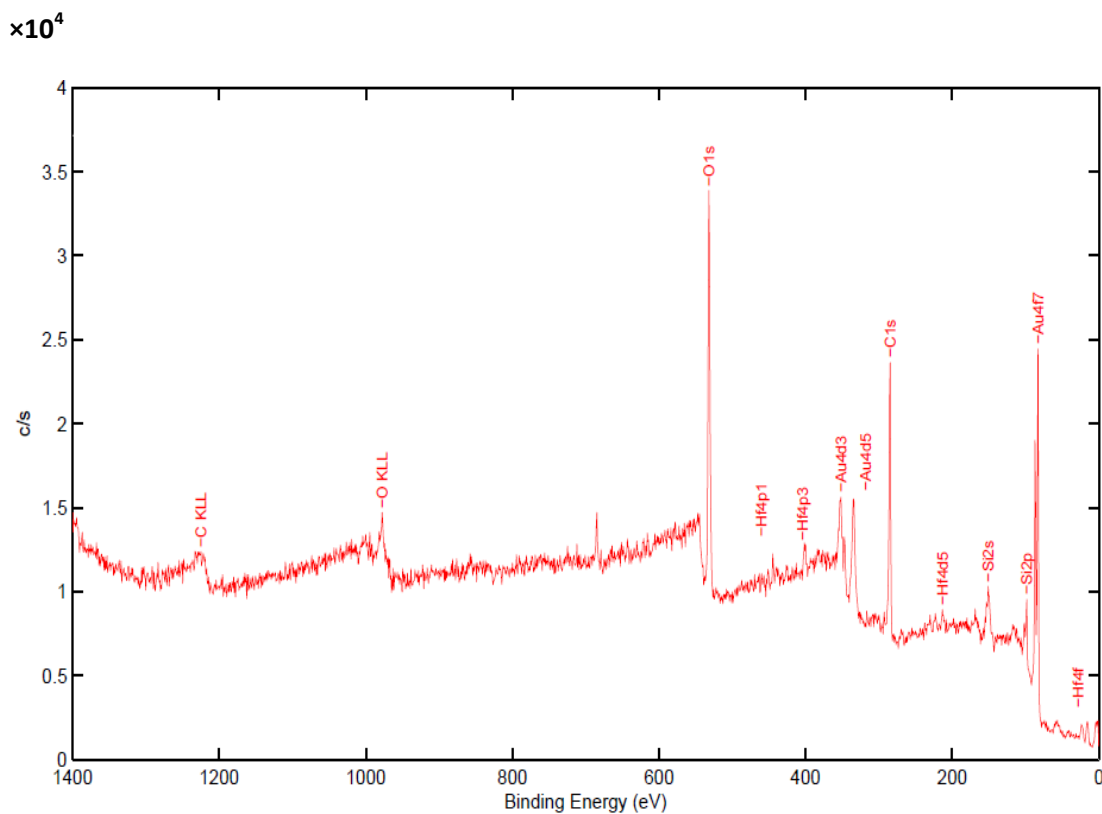


Figure 3.15 : Wide Survey Spectrum of Sample 6 (S₂)

The broad survey scan taken for Sample 7 (S_{2PDS}) contains functionalized nanosandwiches (20 nm Au/ 20 nm HfO₂ /20 nm Au) with thiol- terminated polymer on Si substrate. This spectrum contains 13 peaks which are C1s, C_KLL, O1s, O_KLL, Au4f7, Au4d5, Au4d3, Si2s, Si2p, Hf4f, Hf4d5, Hf4p3 and S2p with the binding energies of 286, 1225, 532, 986, 98, 161, 83, 360, 341, 14, 216, 391 and 168 eV respectively.

From survey spectrum, it was observed that the silicon substrate contains gold, hafnium, oxygen and sulfur. Thus, different from Sample 6, the existence of sulfur element indicates that the PDS polymer was bonded to the specific layer (Au), as shown in Figure 3.16.

$\times 10^4$

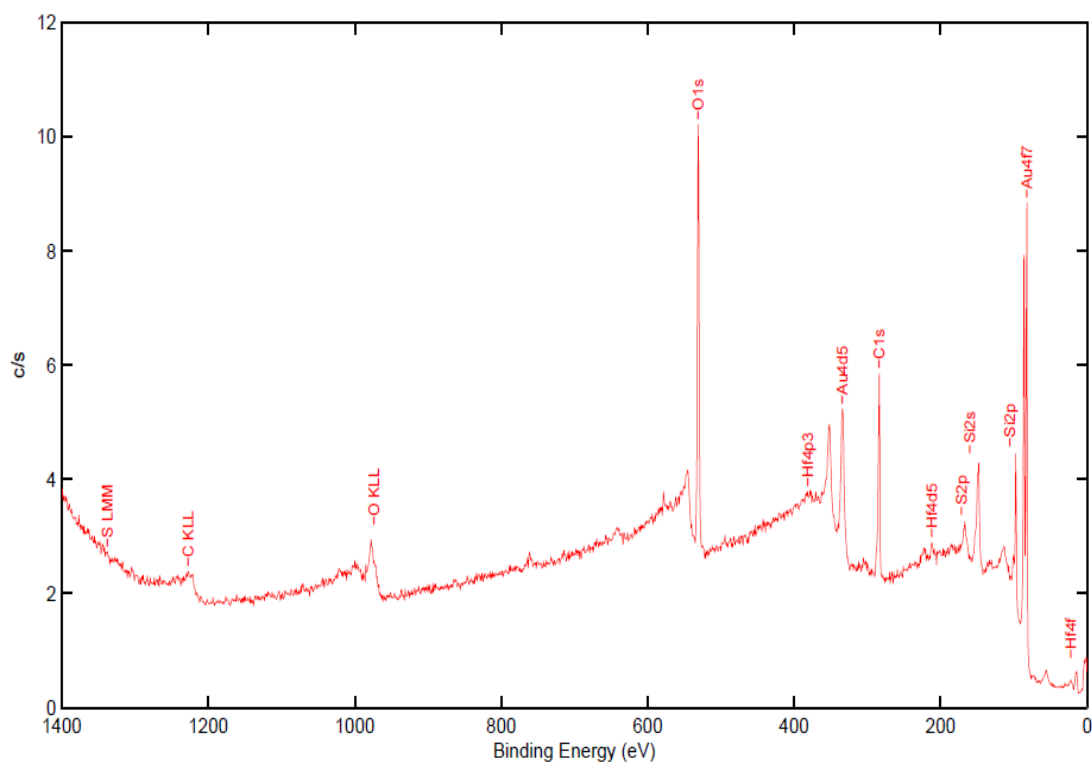


Figure 3.16 : Wide Survey Spectrum of Sample 7 (S_{2PDS})

Figure 3.17 illustrates the survey measurement for Sample 8 (S_{2ATES}) which contains 20 nm Au/ 20 nm HfO₂ / 20 nm Au) on Si surface after functionalization with silane-terminated polymer. 13 peaks of C1s, C_KLL, O1s, O_KLL, Au4f7, Au4d5, Au4d3, Si2s, Si2p, Hf4f, Hf4d5, N1s and N_KLL are displayed in the spectrum, with the binding energies of 286, 1225, 532, 986, 98, 161, 83, 360, 341, 14, 216, 394 and 1095 eV.

These peaks are evidence of the gold, hafnium, oxygen and nitrogen on the surface, as shown in the spectrum. The existence of nitrogen element indicated that silane-terminated ATEs polymer was bonded to its specific layer of HfO₂.

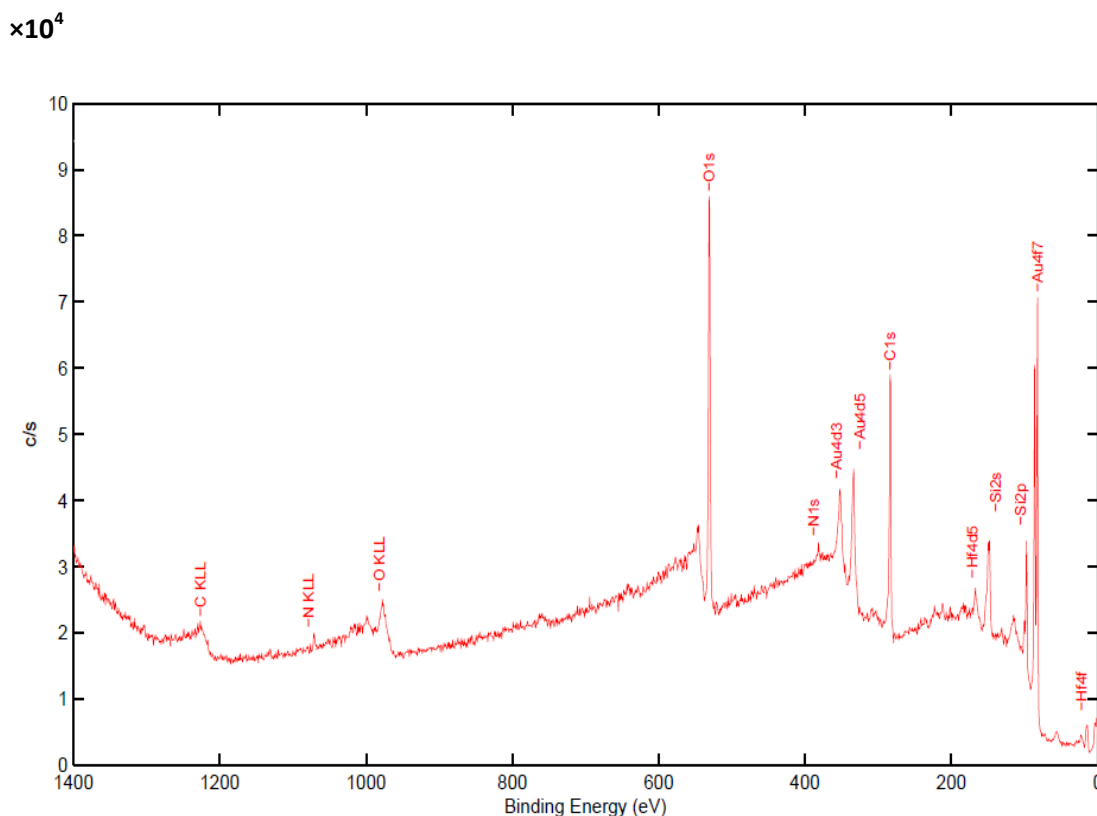


Figure 3.17 : Wide Survey Spectrum of Sample 8 (S_{2ATES})

Finally, the broad survey spectrum of Sample 9 ($S_{2PDS+ATES}$) which includes nanosandwiches (20 nm Au/ 20 nm HfO_2 /20 nm Au) on Si surface after functionalization with both thiol- and silane- terminated polymer is illustrated in Figure 3.18. The survey scan shows 15 peaks, which are C1s, C_KLL, O1s, O_KLL, Au4f7, Au4d5, Au4d3, Au4p3, Si2s, Si2p, Hf4f, Hf4d5, N1s, S2p and S1s spectral regions with corresponding binding energies of 286, 1225, 532, 986, 98, 161, 83, 542, 360, 341, 14, 216, 394, 168 and 224 eV.

The survey spectrum in Figure 3.18 shows the presence of gold, hafnium, sulfur, nitrogen and oxygen on the surface. The existence of sulfur and nitrogen demonstrates that PDS and ATES polymers were bonded to their specific layers, Au and HfO_2 respectively.

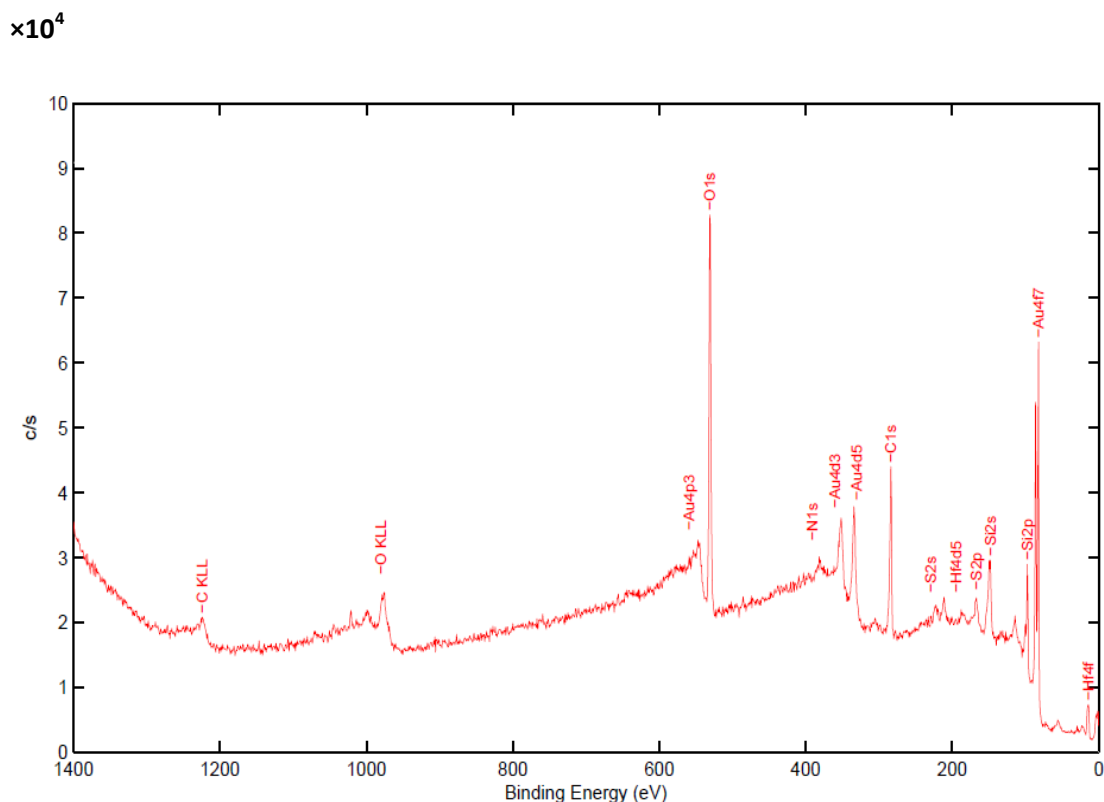


Figure 3.18 : Wide Survey Spectrum of Sample 9 (S₂ATES+PDS)

3.3 Detailed Analysis of the Elements in the Samples

In this section, the XPS spectra of each element (that were identified on the surface of the 9 samples examined in the first section) were taken by focusing the unique range of different elements. These XPS spectra are detailed scans which are used to explain the peak location of the elements and identify the line shapes precisely.

As mentioned in the introduction, the identification of the chemical states of the atoms can be found on the analyzed samples by using XPS. The spectra shows the emitted electrons for each energy level versus their kinetic energy (Wagner, 1979). Each element has its distinct elemental spectrum. In addition, the binding energy of each electron orbit can take various forms. The binding energy values of the same orbits of the same elements may differ because of several reasons. These reasons may include different oxidation states, atomic surrounding states in the energy level of core electrons in atoms, and environment. The spectra should be analyzed by considering the change in the variation of binding energy values which is called chemical shift (Karabudak et al., 2006).

For detailed analysis of the elements, scans were selected broad enough to be able to examine the peak in our region of interest, but less than 25 eV in order to allow determination of the accurate positions of the XPS peaks (Knop-Gericke, 2012), (Van Grieken and Markowicz, 2001).

In this section, detailed scans were recorded focusing the specific range of Au4f, O1s, Si2p, C1s, Al2p, P2p, S2p, Hf4f, N1s regions present on S₁, S_{1PHO}, S_{1PDS}, S_{1PHO+PDS}, S_{1SA} and S₂, S_{2PDS}, S_{2ATES}, S_{2ATES+PDS}. Spectra were taken by 50 sweeps for each region, when the samples were grounded and the flood gun was turned on and was subjected to showering the sample with very low energy electrons. Au4f, O1s, Si2p and C1s spectral regions were observed for all of the nine samples mentioned above. The specific ranges selected for these samples were 80-90 eV for Au4f, 525-538 eV for O1s, 96-106 eV for Si2p, 280-290 eV for C1s.

Firstly, Au4f region was examined for each sample. Au4f peaks were formed of two chemically different parts that are shown in Figure 3.19. The component peak illustrated in Figure 3.19 can be suitable for two doublets. These doublets were separated as Au4f_{7/2} - 4f_{5/2} with 3.6 eV spin-orbit splitting between them (Ertas and Suzer, 2006). The binding energies of the nine samples were measured by using Multipak software. The recorded binding energy values for Au4f peak were 82.816 eV for S₁, 82.741 eV for S_{1PHO}, 82.938 eV for S_{1PDS}, 82.799 eV for S_{1PDS+PHO}, 82.543 eV for S_{1SA}, 82.928 eV for S₂, 82.613 eV for S_{2PDS}, 82.580 eV for S_{2ATES}, 82.678 eV for S_{2ATES+PDS}. The observed binding energy values were not same for each sample. Two possible reasons for the small differences in the binding energy values are the chemical shift, and the charging effects (Iwata and Ishizaka, 1996). The reason we observe the Au4f peaks in these 9 samples is the fact that nanosandwiches in each sample are covered with 40 nm Au layers.

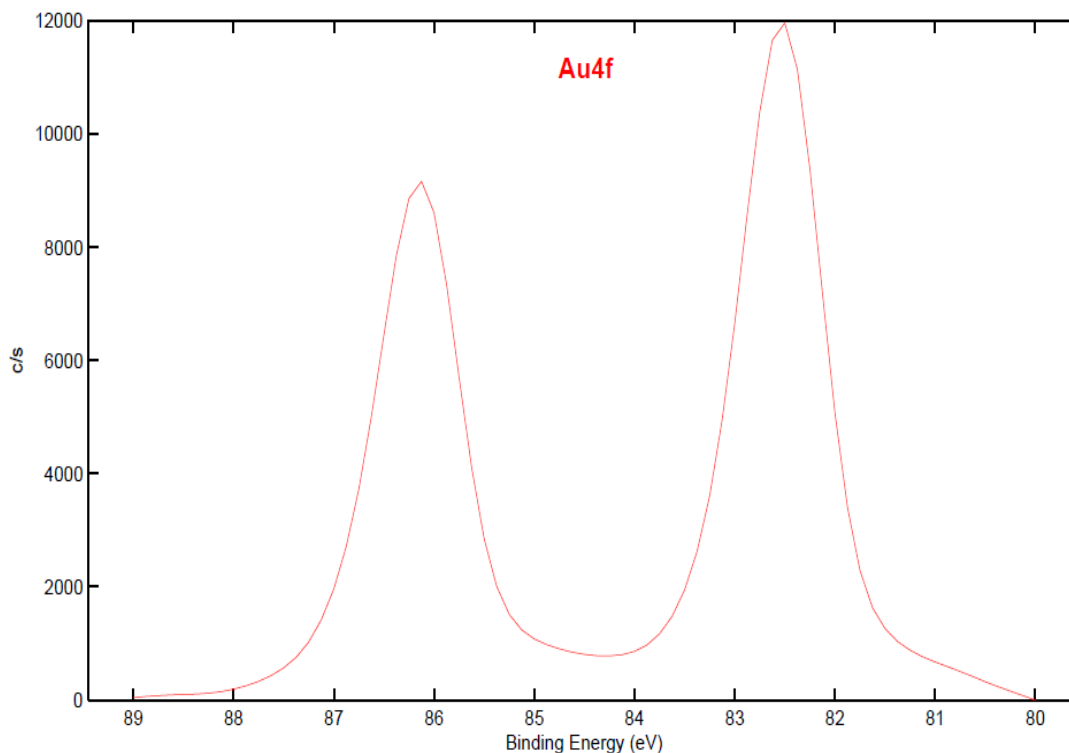


Figure 3.19 : Au4f region of the samples on Si substrate when the samples are grounded

Secondly, the chemical states of the O1s peaks were analyzed for the nine samples. As an example, Figure 3.20 illustrates the peak for the S_{1PDS} sample. The binding energy values which were measured for the nine samples were 530.946 eV for S₁, 531.591 eV for S_{1PHO}, 531.815 eV for S_{1PDS}, 531.787 eV for S_{1PDS+PHO}, 530.711 eV for S_{1SA}, 531.803 eV for S₂, 530.947 eV for S_{2PDS}, 530.933 eV for S_{2ATES} and 530.935 eV for S_{2ATES+PDS} on O1s peak region. It is observed that the binding energy values the samples are different. The difference between these samples can be due to the x-ray satellites and energy loss envelop (Van Grieken and Markowicz, 2001). The chemical states of the samples were determined by the line shape of O1s region. Also, the line shapes help us understand how the polymers (PDS, PHO, ATEs) and streptavidin biomolecule are bonded to the surface (Hyun et al., 2001). These bonds are -COOH, C-O-C, H-O and C=O for O1s region.

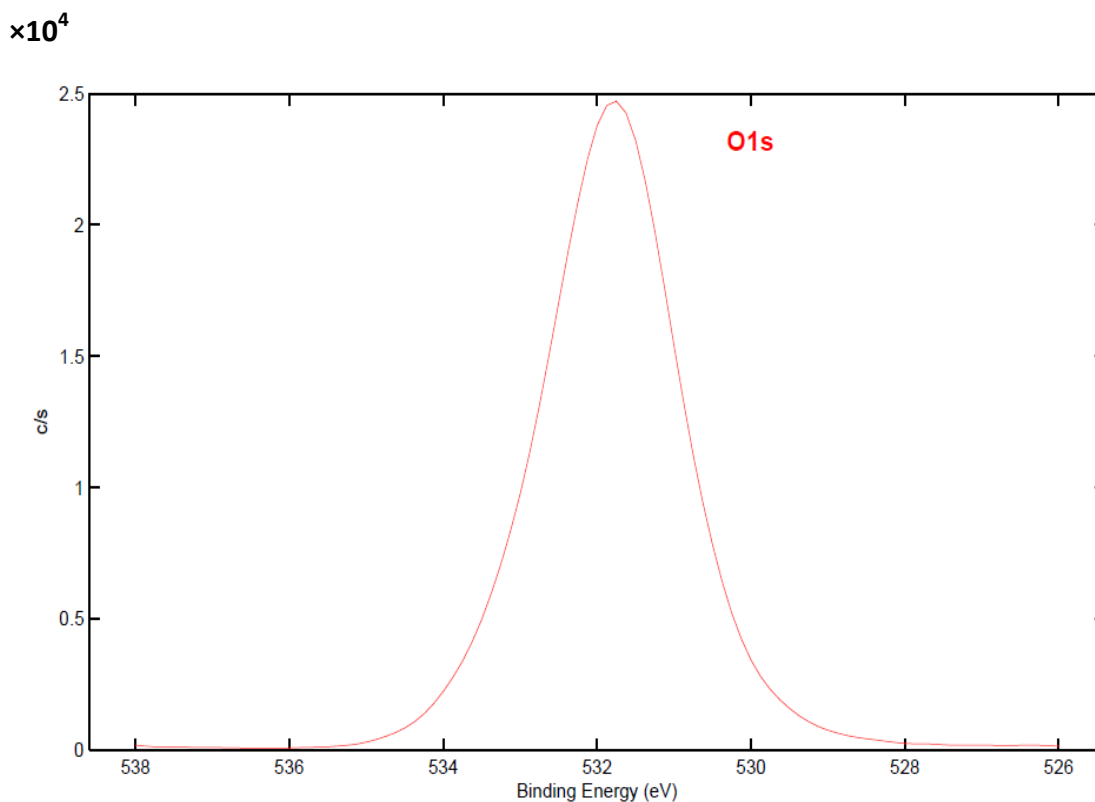


Figure 3.20 : O1s spectrum of the sample recorded, when grounded.

Thirdly, multiplex scans were performed and Si2p peaks were observed for all of the samples. The binding energy values of the nine samples are very close to each other, specifically 97.428 eV for S₁, 97.889 eV for S_{1PHO}, 97.965 eV for S_{1PDS}, 97.927 eV for S_{1PDS+PHO}, 97.406 eV for S_{1SA}, 97.070 eV for S₂, 97.318 eV for S_{2PDS}, 97.353 eV for S_{2ATES}, 97.404 eV for S_{2ATES+PDS} on Si2p peaks. Before each XPS spectrum is taken, the electron flood gun was turned on, and the samples were neutralized. It has been documented in the literature that, depending on the neutralization of samples, the difference in the binding energy values between these components can fluctuate between -1 to 5 eV (Ertas and Suzer, 2006), (Iwata and Ishizaka, 1996), (Ulgut and Suzer, 2003). From Figure 3.21, the Si2p peak is separated into two chemically different constituents, with approximately 3.9 eV difference between them. The first one which can be seen around 101.8 eV in figure 12 was identified as Si⁺⁴ and the other one which can be seen around 97.9 eV was Si⁰ (Wagner, 1979). The chemical shift of the Si neutral atom towards higher energy level by taking the extra electrons ejected from the X-ray shows us that the surface is oxidized. As a result, Si⁰ was transformed into Si⁺⁴, its oxidation state (Ulgut and Suzer, 2003).

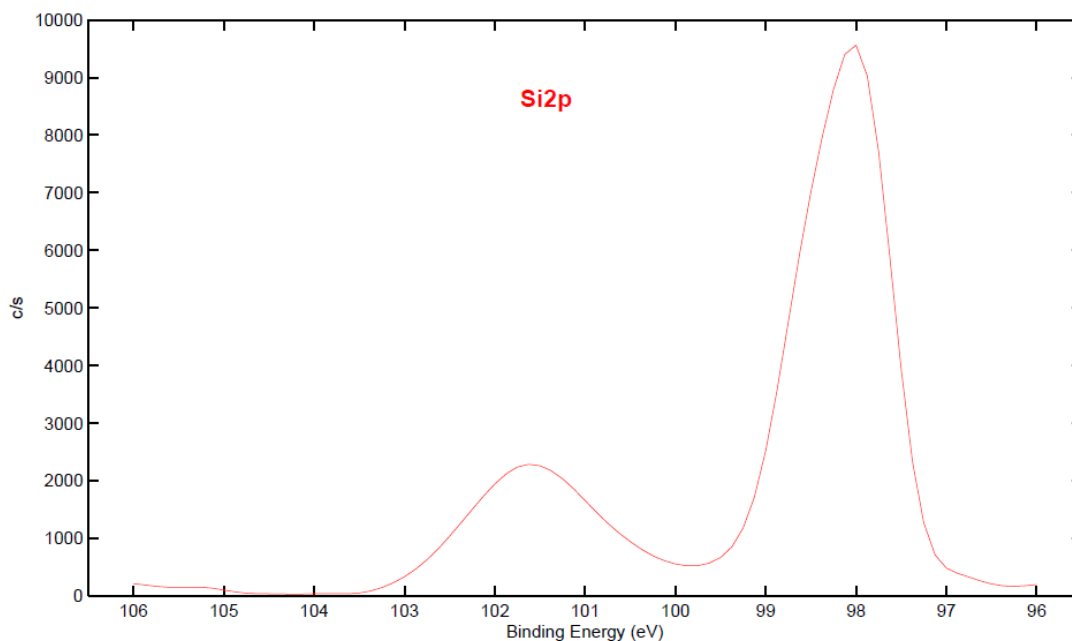


Figure 3.21 : XPS spectra of the Si2p region of the samples on Si substrate

XPS spectra were recorded for nine samples by focusing on the C1s regions. Carbon is identified between the binding energy values of 280 and 300 eV on Si substrate, wherein these emitted electrons match with the C1s peak. The featured C1s peak contains x-ray satellites and energy loss envelope. For C1s region in particular, the binding energy values, heights and areas of the five samples which were named S₁, S_{1PHO}, S_{1PDS}, S_{1PDS+PHO} and S_{1SA} were tabulated in Table 3.2 below.

Table 3.2 : The list of the values of binding energies, heights and areas of the samples.

Au/Al₂O₃/Au NANOSANDWICHES	B.E (eV)	HEIGHT	AREA
Sample 1 (S₁)	283.811	2274	4087
Sample 2 (S_{1PHO})	284.694	16055	29342
Sample 3 (S_{1PDS})	284.805	14320	28503
Sample 4 (S_{1PDS+PHO})	284.385	13777	28356
Sample 5 (S_{1SA})	283.929	7964	14909

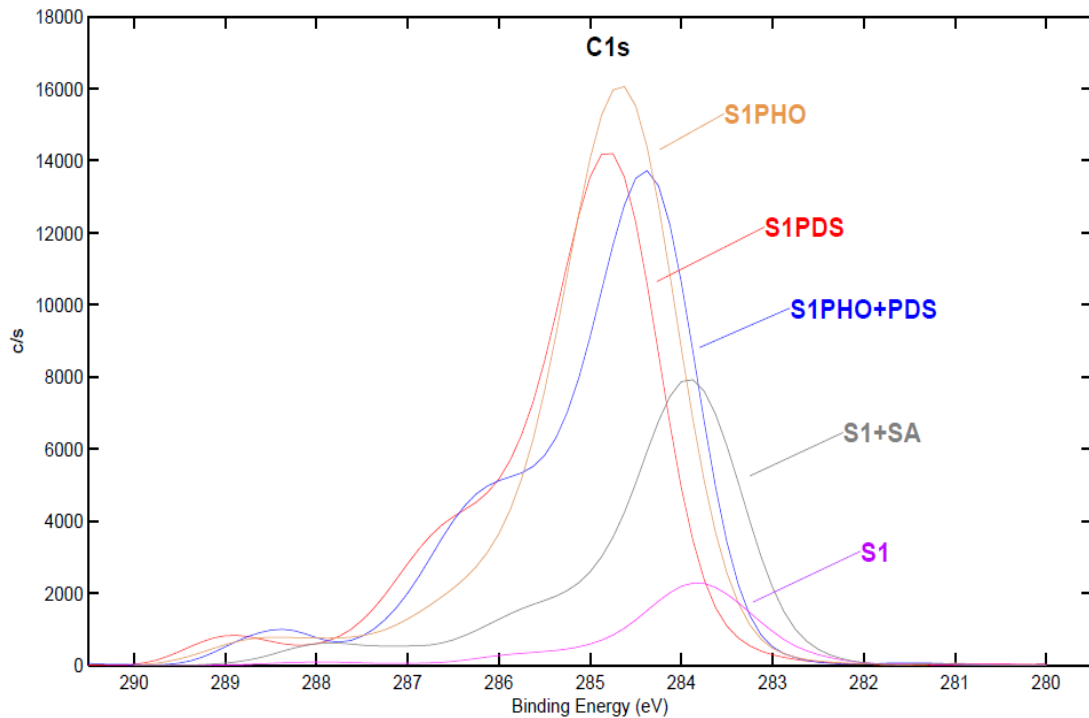


Figure 3.22 : Comparison of the C1s spectra for S₁, S_{1PHO}, S_{1PDS}, S_{1PDS+PHO} and S_{1SA}

The samples mentioned above were compared by using line shapes of C1s. The most convoluted level was observed on the Sample 4 (S_{1PDS+PHO}), and the less convoluted level was on the Sample 1(S₁). Sample 4 has more bonds because it is bonded to both PDS and PHO polymers. These bonds can be seen in the line shapes illustrated in Figure 3.22. Sample 1 is the least convoluted peak because there are no polymers or biomolecules attached to it. Additionally, it follows from Table 2 that these measurements reaffirm that the height and area of Sample 1 is noticeably smaller than other samples. The line shapes which can be seen in Figure 3.22 included the bonds that were on the samples. These bonds can be found as C-H, C-O, C=O on the C1s peaks. Thus, it is confirmed that the PDS and PHO polymers and streptavidin molecule are bonded to the Si surface (Sezen et al., 2007)

Table 3.3 : Tabulated values of binding energy, height and area on the samples (S_2 , S_{2PDS} , S_{2ATES} , $S_{2ATES+PDS}$)

Au/ HfO ₂ /Au NANOSANDWICHES	B.E (eV)	HEIGHT	AREA
Sample 6 (S_2)	284.821	4896	9067
Sample 7 (S_{2PDS})	283.997	10303	23121
Sample 8 (S_{2ATES})	283.682	11556	22414
Sample 9 ($S_{2ATES+PDS}$)	283.953	7299	17915

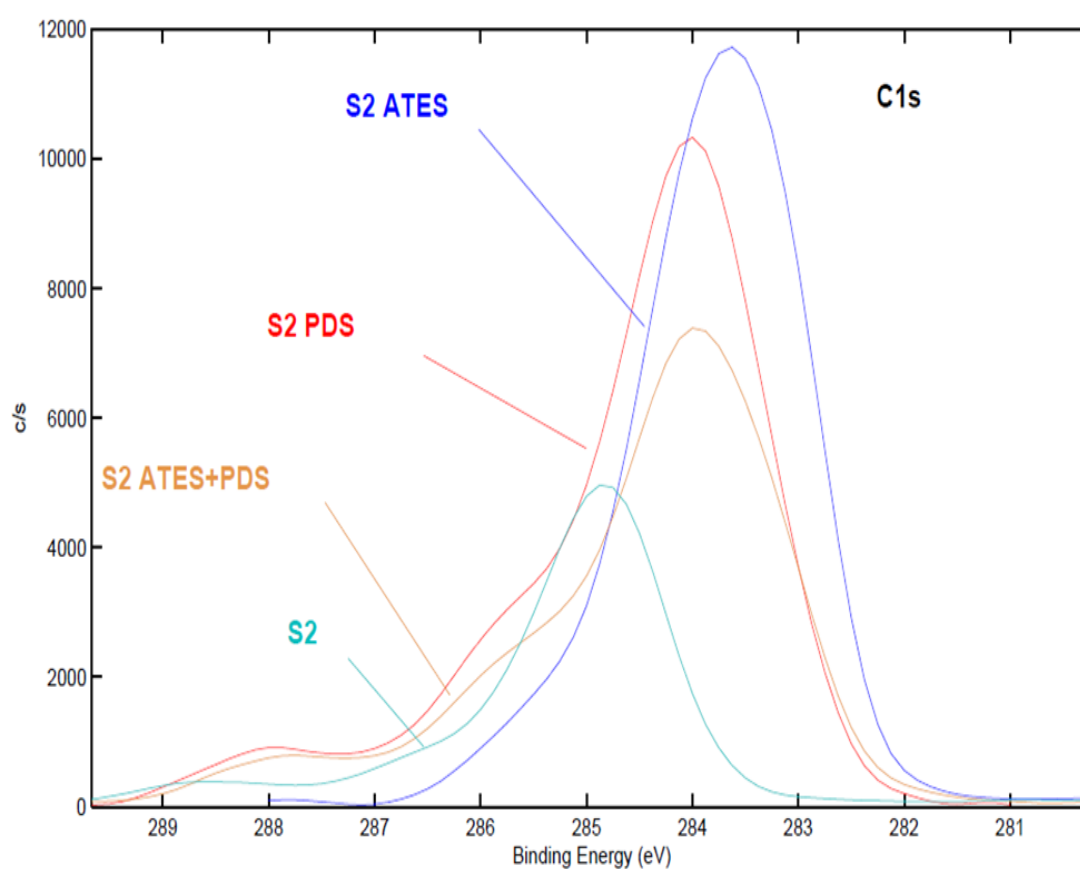


Figure 3.23 : Comparison of the C1s region for S_2 , S_{2PDS} , S_{2ATES} and $S_{2ATES+PDS}$

Since the remaining four samples contain Au/ HfO₂/ Au nanosandwiches (as opposed to Au/ Al₂O₃/ Au nanosandwiches), they are analyzed separately. Figure 3.23 illustrates the C1s peaks for the four samples with different line shapes. When we compare these samples, we can see that S_2 has the peak with the least intensity. Since there are no polymers or biological molecules on it, this sample has the C1s peak with the smallest number of ties. Not surprisingly, when we compare the height

and area values in Table 3.3, it is clear that the smallest measures are for S_2 . However, since the other samples are bonded to polymer(s), their line shapes are more convoluted. This is why the height and area values are high for these samples in Table 3.3. The bonds in these samples are C-H, C-O-, C=O (Suzer et al., 2007).

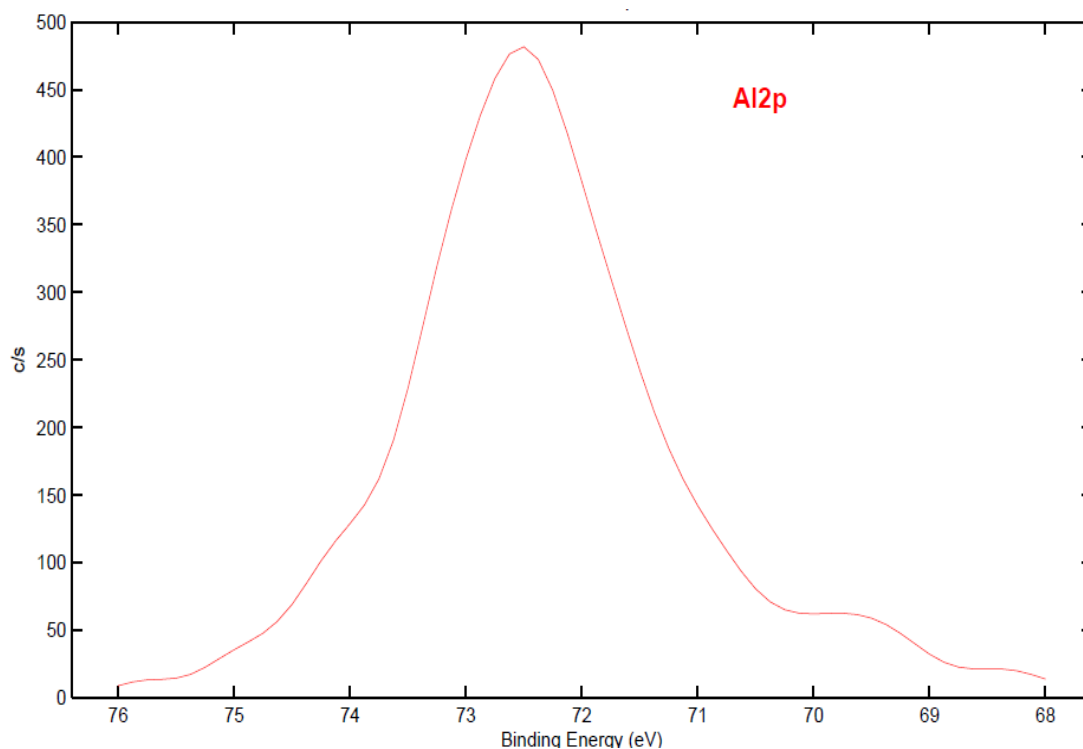


Figure 3.24 : XPS spectra of Al₂p region for the samples

XPS spectra of Al₂p were recorded when the samples were grounded by using 50 sweeps, as shown in Figure 3.24. Al₂p peaks were found in S_1 , $S_{1\text{PHO}}$, $S_{1\text{PDS}}$, $S_{1\text{PDS+PHO}}$ and $S_{1\text{SA}}$ samples comprised of Au/ Al₂O₃/ Au nanosandwiches. Since there are Al₂O₃ layers in the middle of the nanosandwiches, the Al₂p peak is formed on the surface. The binding energy values of Al₂p peaks are 73.087 eV for S_1 , 73.838 eV for $S_{1\text{PHO}}$, 74.084 eV for $S_{1\text{PDS}}$, 72.889 eV for $S_{1\text{PDS+PHO}}$, 72.522 eV for $S_{1\text{SA}}$. It is observed that the binding energy values for these samples are very close to each other. As mentioned in the introduction part, the electrons which were detected through a photoemission by the analyzer of XPS are from the farthest layers (<10 nm). (DEMIROK, 2005). As described before, our nanosandwiches are composed of three layers of 20 nm thickness each. Since the Al₂O₃ layer is in the middle layer of the nanosandwich, and takes place between 20-40 nm, the XPS detector cannot penetrate deep enough to analyze Al₂p peak at that level. Thus, the intensity of Al₂p peak can be seen very low, at the value of 469 c/s, as shown in Figure 3.24.

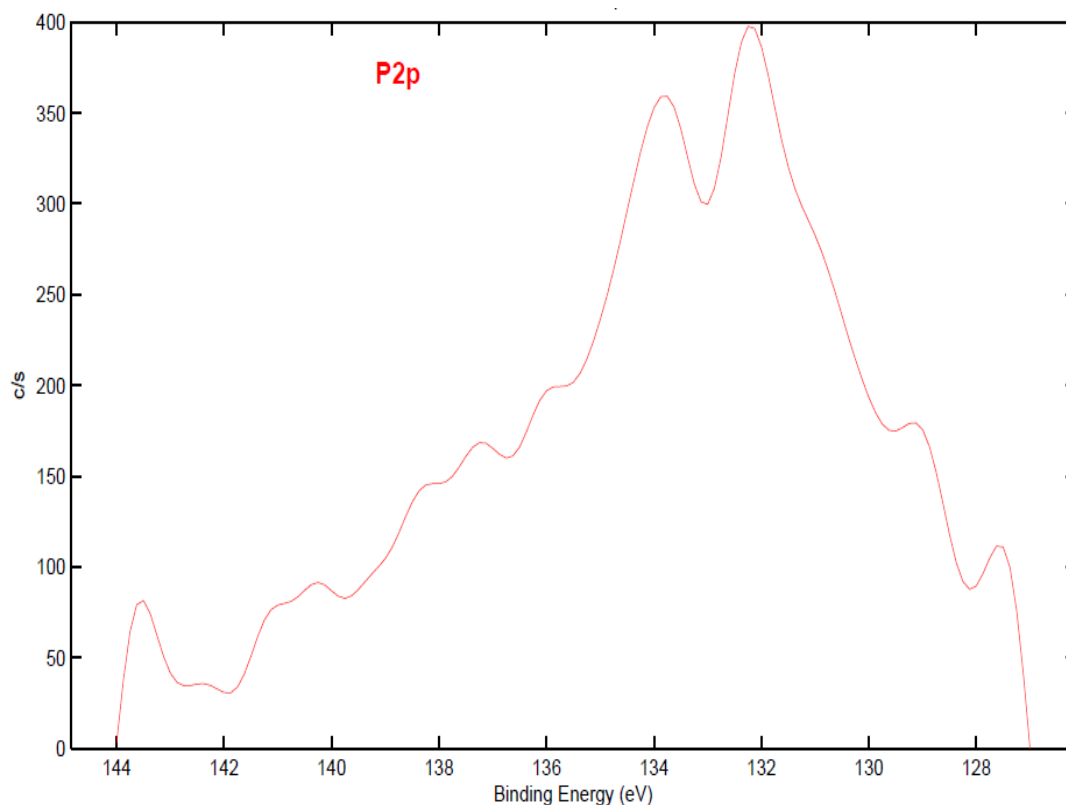


Figure 3.25 : P2p region of the grounded samples on the Si substrate

Next, the samples were analyzed focusing on the P2p regions. $S_{1\text{PHO}}$ and $S_{1\text{PDS+PHO}}$ samples include the P2p peaks, with the binding energy values of 132.320 eV for $S_{1\text{PHO}}$, 132.955 eV for $S_{1\text{PDS+PHO}}$ at the specific range. These samples were functionalized with PHO polymers to the nanosandwiches. PHO polymers are bonded to the Al_2O_3 layer through the phosphorus element. Thus, we can observe the P2P peak in Figure 3.25 for the sample $S_{1\text{PHO}}$.

Hf4f peak in Figure 3.26 was recorded for the samples which are S_2 , $S_{2\text{PDS}}$, $S_{2\text{ATES}}$ and $S_{2\text{ATES+PDS}}$ with the binding energy values of 15.048, 14.432, 14.519 and 14.369 eV respectively. These samples are nanosandwiches comprised of three layers, with HfO_2 layer in the middle ($\text{Au}/\text{HfO}_2/\text{Au}$). Because of the position of the layers, the photoelectrons can provide a shallow representation of the peaks, with Hf4f peak at the intensity value of 1800 c/s. Figure 3.26 depicts this peak for the samples.

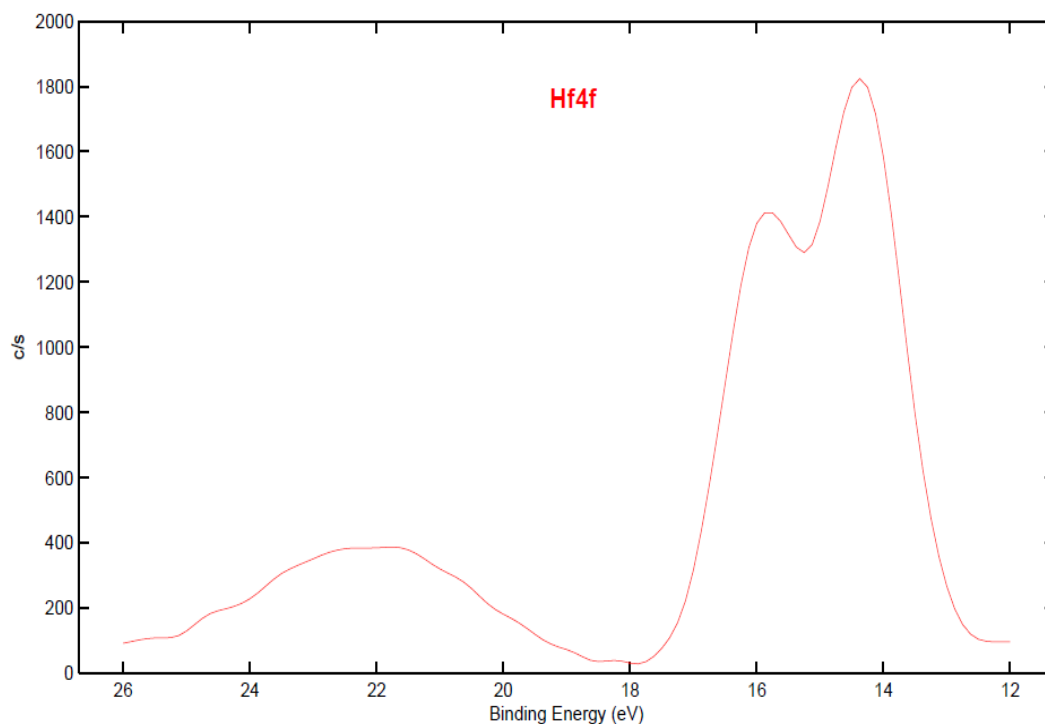


Figure 3.26 : XPS spectrum of the Hf4f region on the samples

S2p spectral regions were analyzed for the samples S_{1PDS} , $S_{1PDS+PHO}$, S_{1SA} , S_{2PDS} , S_{2ATES} and $S_{2PDS+ATES}$ with corresponding binding energies of 167.943, 168.128, 166.913, 167.289, 166.908, and 167.053 eV. S2p peak which is plotted in Figure 3.27 indicates that the sulphide is detached from the polymers, leaving an active anchor to bind to the gold layers (Zareie et al., 2008a). These bonds that are attached to the gold layer are in the form of C-S-Au & -S-C-S-, C-S-.

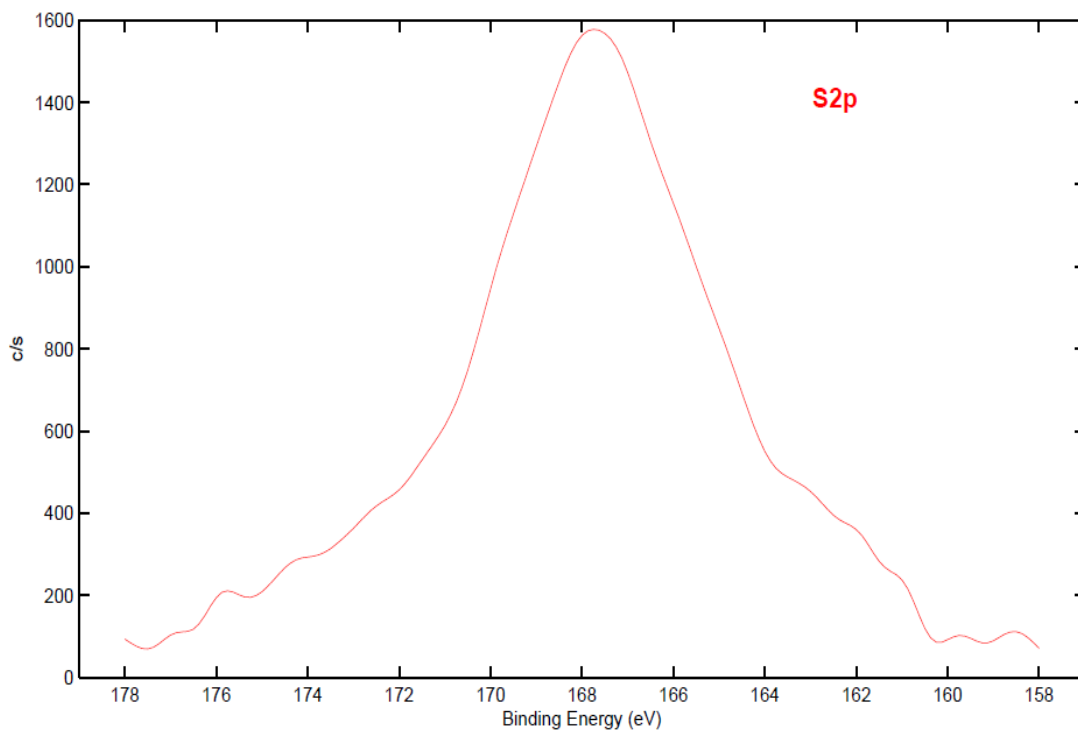


Figure 3.27 : S2p spectrum of the grounded samples

Finally, N1s spectrum was recorded for the samples which are S_{1SA}, S_{2ATES}, S_{2ATES+PDS} with the binding energy of 398.08, 399.347 and 398.348 eV respectively. The binding energy values of the samples are very close to each other. The N1s peak intensity is observed very low, with 160 c/s, as shown in Figure 3.28. So, the chemical state of the elements can not be seen very clearly on the samples. However, the N1s peak in Figure 3.28 indicates that polymers and biomolecules are bonded to the surface.

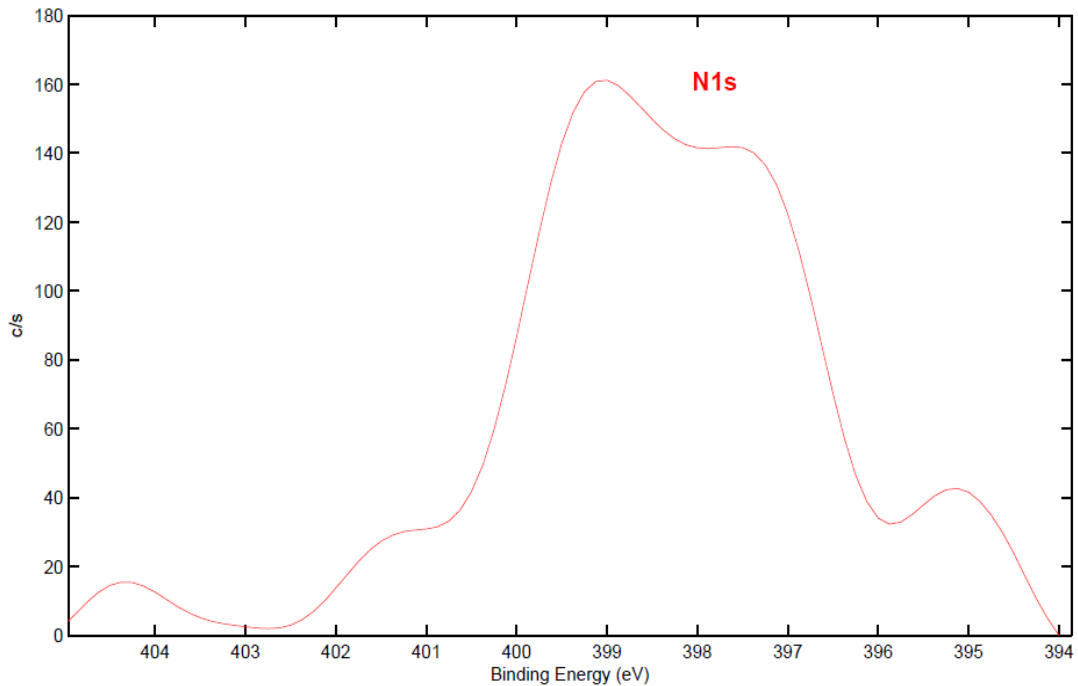


Figure 3.28 : XPS spectrum of the N1s region

3.4 Applying External Square Wave Pulse for Monitoring Frequency

Dependence of Nanostructures

In this section, the nanostructures were examined applying an external bias with different frequencies to each sample while recording XPS data to evaluate charging and electrical potential of the surfaces, and detecting an interaction between nanostructures and X-rays (Ishii, 2009).

Previously, researchers have applied external bias to the conductive and nonconductive materials in order to obtain structural and chemical information of the surfaces while recording XPS data (Suzer, 2003). The binding energy of the voltage applied sample can be shifted with the external bias (Ekiz et al., 2010), which causes differential charging of the sample (Ertas and Suzer, 2004). In the XPS measurements, the differential charging can be seen as a problem for conducting and insulating samples because of the unfinished neutralization of the photoemitted electrons (Dubey et al., 2006). The differential charging (or surface charging) is positive charging which can be tracked by the binding energy differences in charging behavior of layers/components (Barr, 1989). The binding energy shifts are also affected by partial neutralization of the samples due to the exposure to the stray

electrons (Suzer, 2003). On the other hand, the negative charging on the surface may be formed when a low energy electron flood was used for neutralizing (Barr, 1989).

As mentioned in the introduction part, surface charging which was controlled under X-Ray radiation for extracting chemical, physical, structural and electrical parameters of surfaces for different studies (Suzer and Dâna, 2006), can be explained with the help of the external bias. Application of external bias while recording XPS data changes binding energy values of the peaks. This is due to the change in kinetic energy of photoelectrons because of the electrical potential on the surface (Sezen,2008). The kinetic energies of the peaks are increased when the samples are subjected to negative voltage, and decreased under positive voltage (Sezen et al., 2007). When positive voltage is applied to the sample, the sample can be attractive for low energy electrons, reducing the positive charging on the surface (Sezen et al., 2007). However, the application of the negative voltage can increase the positive charging due to the rebounding low-energy electrons while neutralizing (Ulgut and Suzer, 2003), (Ertas and Suzer, 2004), (Suzer and Dâna, 2006). Application of DC stress can control the surface charging as mentioned above.

Besides, surface charging can be controlled with the application of square wave pulses (SQW) (Sezen et al., 2007). Capacitance, resistance, charging and discharging properties of the samples can be obtained from the SQW pulses with different frequencies while XPS peaks are recorded (Suzer et al., 2008). Applying SQW pulses to the samples is a very convenient and valuable technique in order to explain the change in the peak positions due to electrical potential which were obtained as a result of the surface charging (Bauer et al., 2001), (Björneholm et al., 1992), (Drescher et al., 2002), (Höfer et al., 1997), (Hövel et al., 2004), (Hövel et al., 1998), (Marsi et al., 2000).

In this thesis, SQW pulses technique was chosen to apply to the samples in order to analyze differential charging of the surfaces in XPS measurements (Dane et al., 2006). Electrical parameters such as capacitance can be obtained with differential charging through XPS measurement analysis (Zhang et al., 2005) in order to show the capacitance analyses for potential establishment of novel biosensing method in our study (Suzer and Dâna, 2006).

In this section, the nanosandwiches which were analyzed in the previous two parts were examined by applying square wave pulses (SQW) with an amplitude of $\pm 10\text{V}$ and different frequencies ranging from 0.1 Hz to 250 kHz (specifically: 150, 160, 170, 180, 185, 190, 195, 200, 205, 210, 215, 220, 230, 240, 250 kHz) to the samples while XPS data were recorded. The SQW pulses were applied to the samples with the function generator which was connected to the XPS and when the flood gun was turned on. The XPS scans were taken for specific energy ranges of Au4f, Si2p, C1s and O1s elements for the nine samples.

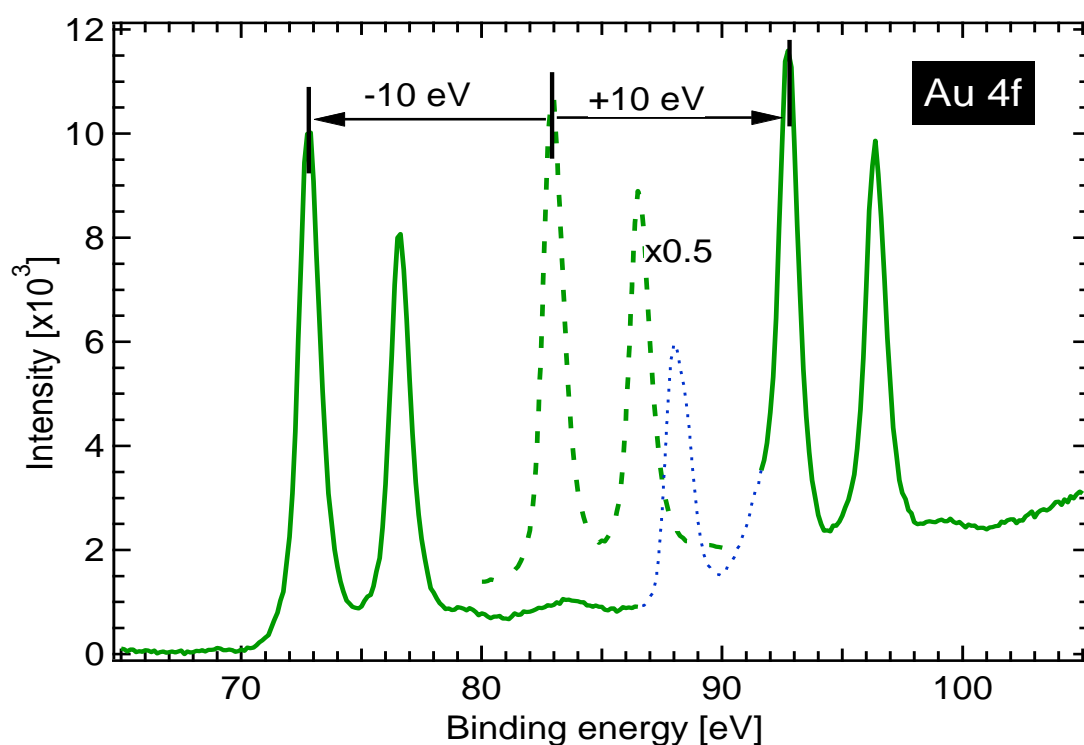


Figure 3.29 : XPS data from the Au4f region

In Figure 3.29, the position of photoelectron peak energy levels are shown with the dashed curves when the samples were grounded (when no voltage was applied but flood gun was turned on). Solid curves, on the other hand, show the upward and downward shifts of the photoelectron peak energy levels due to the application of square wave pulses to the samples with $\pm 10\text{V}$ amplitude for a 150 kHz frequency. The binding energy difference between the two solid peaks was measured 20 eV as expected since we applied external ± 10 voltage.

In a series of experiments, 20eV of solid peak energy difference were observed as the same for 160, 170, 180 kHz frequencies and for the nine samples as shown in Figure

3.29. The intensities of the solid peaks were decreased because of the shifts between binding energies. Therefore, in order to compare grounded and applied voltage samples, the intensities of Au4f, Si2p, C1s and O1s shown with the dashed peaks have been rescaled by a factor 0.5.

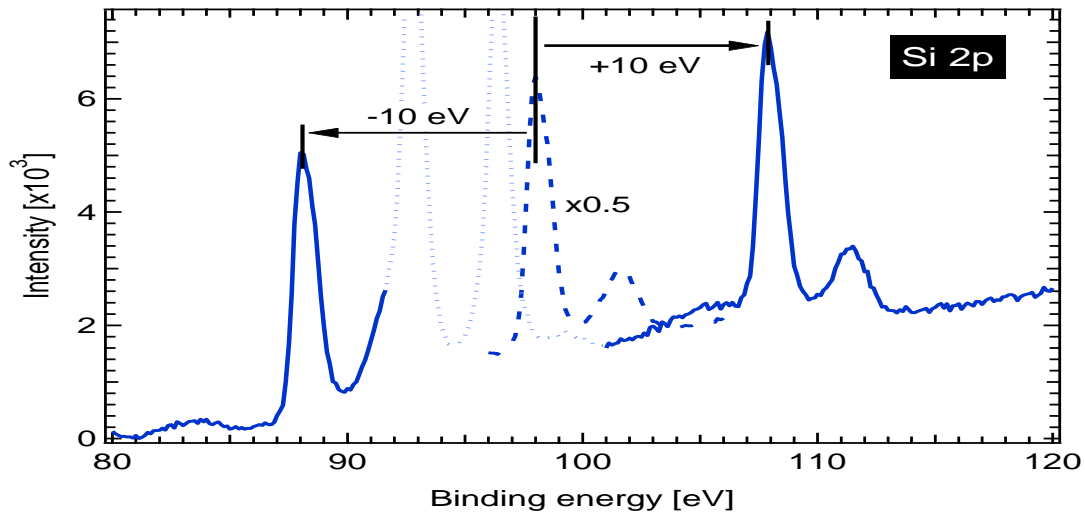


Figure 3.30 : Si2p spectra of recorded, when grounded (dashed curves) and when subjected to ± 10 V SQW pulses of 150 kHz (solid curves)

From Figure 3.30, the samples which are formed with different layers of nanosandwiches are S_1 (Au/ Al_2O_3 / Au layers), S_{1PHO} , S_{1PDS} , $S_{1PDS+PHO}$, S_{1SA} , and S_2 (Au/ HfO_2 / Au layers), S_{2PDS} , S_{2ATES} and $S_{2PDS+ATES}$ were recorded by XPS under SQW pulses (± 10 V) which lead to the doubled peaks at -10 and +10 eV positions for 150 kHz frequency. The separations of the solid curves were due to the charging capacity of the layers because of the neutralization of the the stray electrons on the samples (Suzer, 2003).

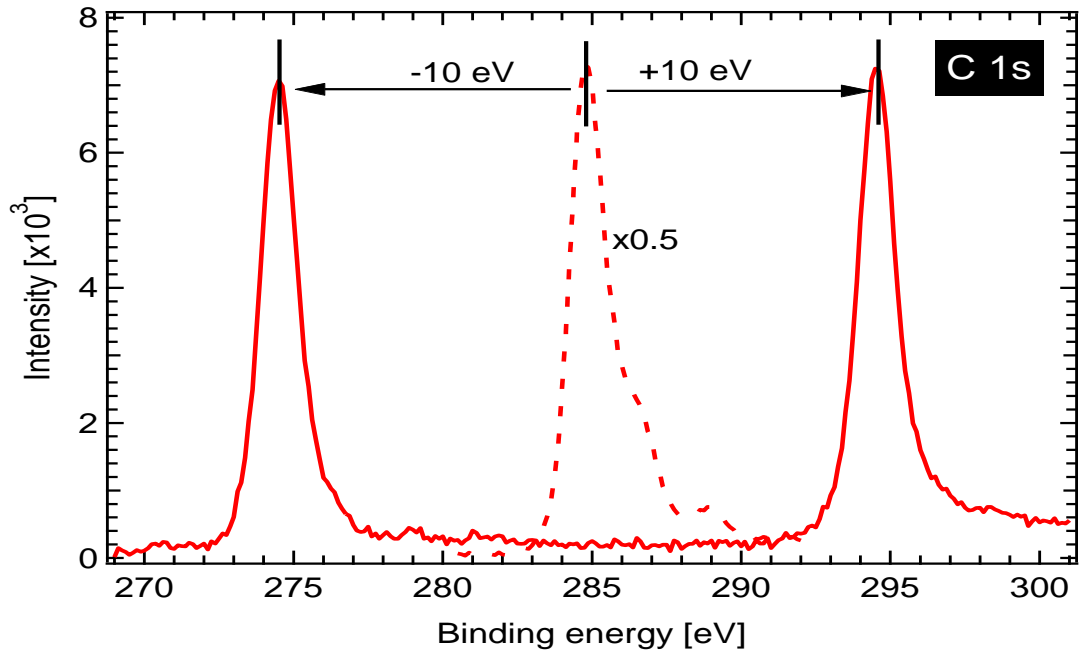


Figure 3.31 : C1s region under ± 10 SQW excitation for the nanostructures

XPS spectra of C1s region were taken under external ± 10 V with square-wave pulses obtained from the function generator as shown in Figure 3.31. The SQW pulses were applied to the samples in order to control photoelectrons which come from the flood gun and traveling inside the samples (Ulguut and Suzer, 2003), (Karadas et al., 2004).

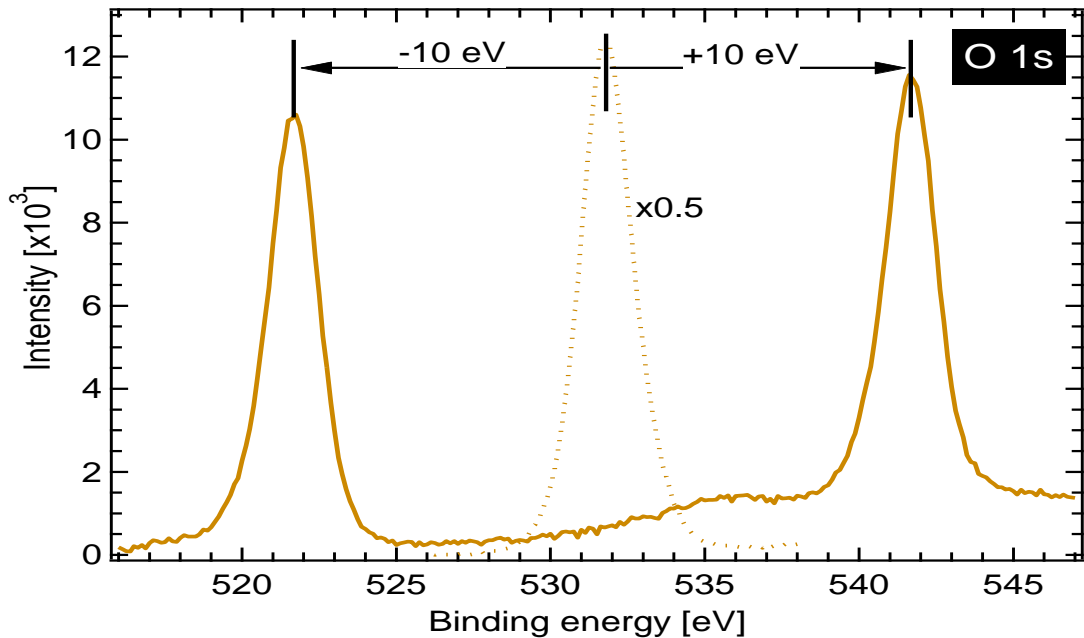


Figure 3.32 : XPS spectra for O1s region when grounded and subjected to ± 10 V amplitude of SQW pulses

Lastly, C1s, O1s, Si2p and Au4f regions of the nine samples were analyzed by XPS while applying ± 10 voltage, so C1s peak is divided into two peaks as demonstrated in Figure 3.32. The remaining regions were also similarly divided depending on the polarity and amplitude of the pulse stress (Guittet et al., 2001). The difference in the binding energy between the two separated peak values is 20eV for the four regions in the nine samples. This result conforms our expectations, because of the application of external bias (± 10 V) to the sample for different frequencies ranging from 0.1 Hz to 180 kHz. The above mentioned XPS measurements were repeated 3 times to show reproducibility at the same conditions for each sample and each of the 4 regions of interest.

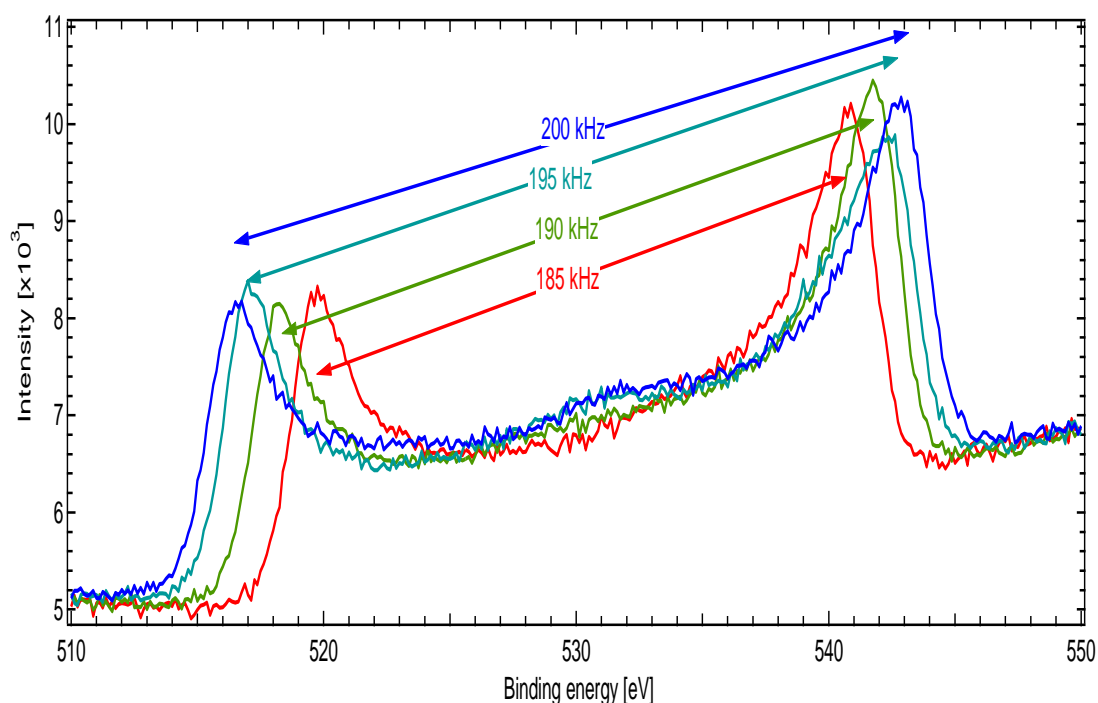


Figure 3.33 : XPS data from the O 1s region when a ± 10 V amplitude voltage is applied to the sample for different frequencies: 185 kHz, 190 kHz, 195 kHz and 200 kHz.

In Figure 3.33, XPS data from O1s region was taken when ± 10 V amplitude of SQW pulses were applied to the nine samples for different frequencies of 185, 190, 195 and 200 kHz when the flood gun was turned on by using 50 sweeps for each measurement. The same XPS results were observed for Au4f, C1s and Si2p regions, with the identical recorded binding energy differences between the peaks for the above mentioned frequencies.

When the frequency values of the samples were gradually increased from 180 to 185, 190, 195, 200 kHz respectively, the binding energy differences between the peaks also increased. The shift in the binding energies was obtained due to the differential charging which also varied depending on the frequency values. Thus, the O1s peaks were shifted because of the accumulated charge in the samples with varying levels of charge storage capacities. As a result, the charging features of the samples due to the molecular structures can be obtained from changing electrical parameters and passing electrons on the samples when XPS measurements were taken under external bias with SQW pulses. (Suzer, 2003), (Suzer and Dâna, 2006), (Suzer et al., 2007).

3.5 Charging and Discharging Properties of Nanostructures

As mentioned in the introduction part, charging/discharging properties of the nanostructures and the collection of charge into the dielectric layers are quite significant in order to produce biosensors and different devices (Sze and Ng, 2006). In general, charging of the materials can be seen as a complication for identifying the binding energy of the multiple moieties in non-conducting samples (Metson, 1999), (Dickinson et al., 1975), (Cros, 1992). Nonetheless, the charging / discharging process can help identify the electrical parameters on the samples which include multiple surface structures (Lau, 1989), (Doron-Mor et al., 2000), (Lewis and Kelly, 1980) and it is acceptable as a helpful technique. For this reason, this technique was used for our samples that consist of multiple layers of nanosandwiches in order to investigate electrical and capacitance properties of the surfaces in this thesis.

In this section, XPS measurements were analyzed from the nine samples which were recorded under ± 10 V amplitude of SQW pulses with the range of 150 to 250 kHz frequencies to display charging/ discharging dynamics on the nanostructures. Particularly, ± 10 V of external bias was chosen to apply to the surfaces in order to control the stray low-energy electrons sent from the flood gun, as well as the secondary electrons reflected from the surface (Ulgut and Suzer, 2003), (Karadas et al., 2004). Thus, XPS was used to extract capacitance parameters of nanostructures under external bias with varying frequencies.

Firstly, the five samples were examined which fabricated ordered arrays of Au/ Al₂O₃/ Au nanosandwiches with 20 nanometer thickness by using nanosphere

lithography technique (NSL). These metal/ insulator/ metal (Au/ Al₂O₃/Au) layers were selected to design and construct a variety of nanosandwiches such as capacitors.

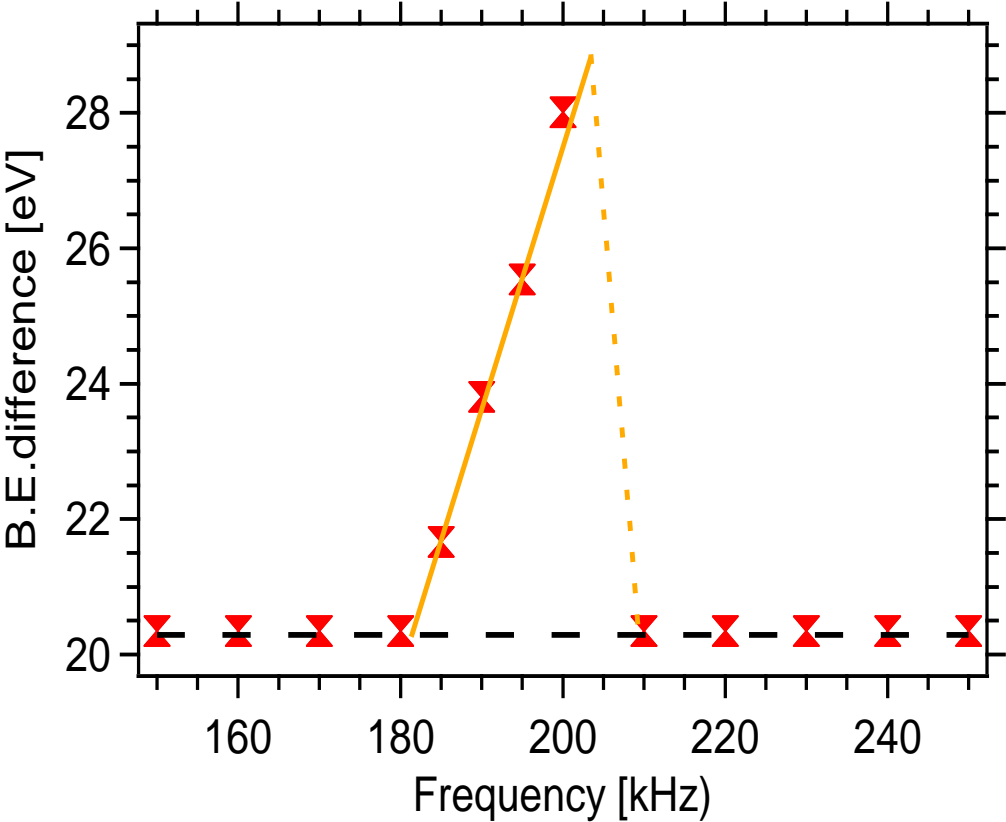


Figure 3.34 : Frequency dependence of the measured difference between the peaks for S₁.

Table 3.4 : The B.E differences Vs. frequency values S_{1PHO}

Frequency (kHz)	B.E Difference (eV)
150	20
160	20
170	20
180	20
185	21.662
190	23.809
195	25.539
200	28.009
210	20
220	20
230	20
240	20
250	20.349

XPS data of the S_1 (Au/ Al₂O₃/Au nanosandwiches) sample were taken when applied ± 10 amplitude voltage for different frequencies. From Table 4, the change in binding energy differences versus frequencies of the S_1 can be seen. When we change the frequency from 150 up to 180 kHz, the binding energy difference does not change as shown in Figure 3.34. However, when we increase the frequency to 185 kHz, the binding energy difference starts to increase to 21.662 eV. It continues to increase with 190 kHz and the increase in the binding energy is measured as 23.809 eV. Binding energy difference continues to increase to 25.539 eV for 195 kHz, and from Figure 3.34, when the frequency is at 200 kHz, the binding energy difference reaches its peak of 28.009 eV. Recall that we applied 20 eV to the S_1 sample, but we saw 28.009 eV in Table 3.4, an 8.009 eV increase due to the shift of peaks.

As shown in Table 3.4, when the frequency goes up to 210 kHz, the binding energy difference goes down to the initial 20 eV, and remains at 20 eV when the frequency is further increased. Thus, it can be said that S_1 sample is charging between 185-200 kHz, and discharging after 200 kHz from Figure 3.34. The specific range of charge accumulation is 185 to 200 kHz in this sample. And this charging/ discharging properties are observed the same way for Au4f, Si2p and C1s regions on this sample. The charging/ discharging is due to the differential charging of the dielectric layer (Al₂O₃) and the polarity of the external bias (Yonzon et al., 2005), (Zhang et al., 2005).

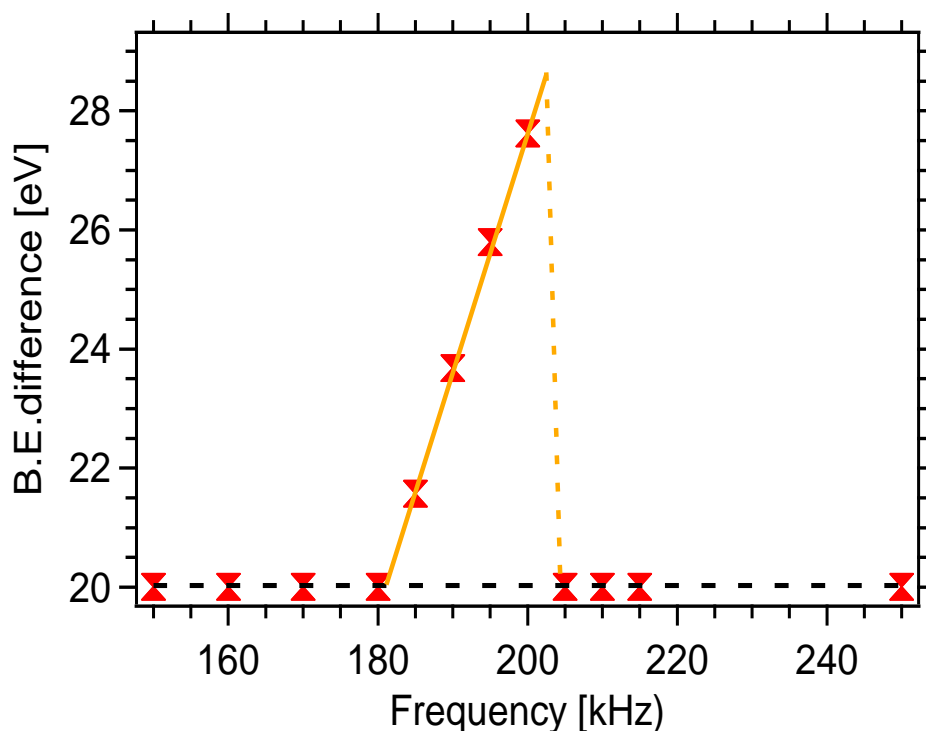


Figure 3.35 : Frequency dependence of the measured difference between the peaks like Figure 24 for S_{1PHO}

Table 3.5 : The B.E differences Vs. frequency values S_{1PHO}

Freq.(kHz)	B.E Diff.(eV)
150	20
160	20
170	20
180	20
185	21.57
190	23.676
195	25.796
200	27.619
205	20
210	20
215	20
220	20
230	20
240	20
250	20

Secondly, XPS results were taken under ± 10 voltage with various frequencies which are tabulated in table 5 for S_{1PHO} sample. The Au/ Al_2O_3 / Au nanosandwiches were functionalized with PHO polymer which is the phosphate terminated polymer by using SAM technique. From Figure 3.35, it is observed that the highest binding

energy difference is 27.6 eV at 200 kHz frequency which is less than the binding energy value of the unfunctionalized nanosandwiches because of the binding of the polymer on the Al_2O_3 dielectric layer. This polymer binding affected the differential charging on the $\text{S}_{1\text{PHO}}$ (Sezen et al., 2007). From Table 3.5, there is a connection between frequency and binding energy shift under the SQW pulses on the $\text{S}_{1\text{PHO}}$ sample. Thus, the sample is charging from 185 to 200 kHz and discharging after 200 kHz.

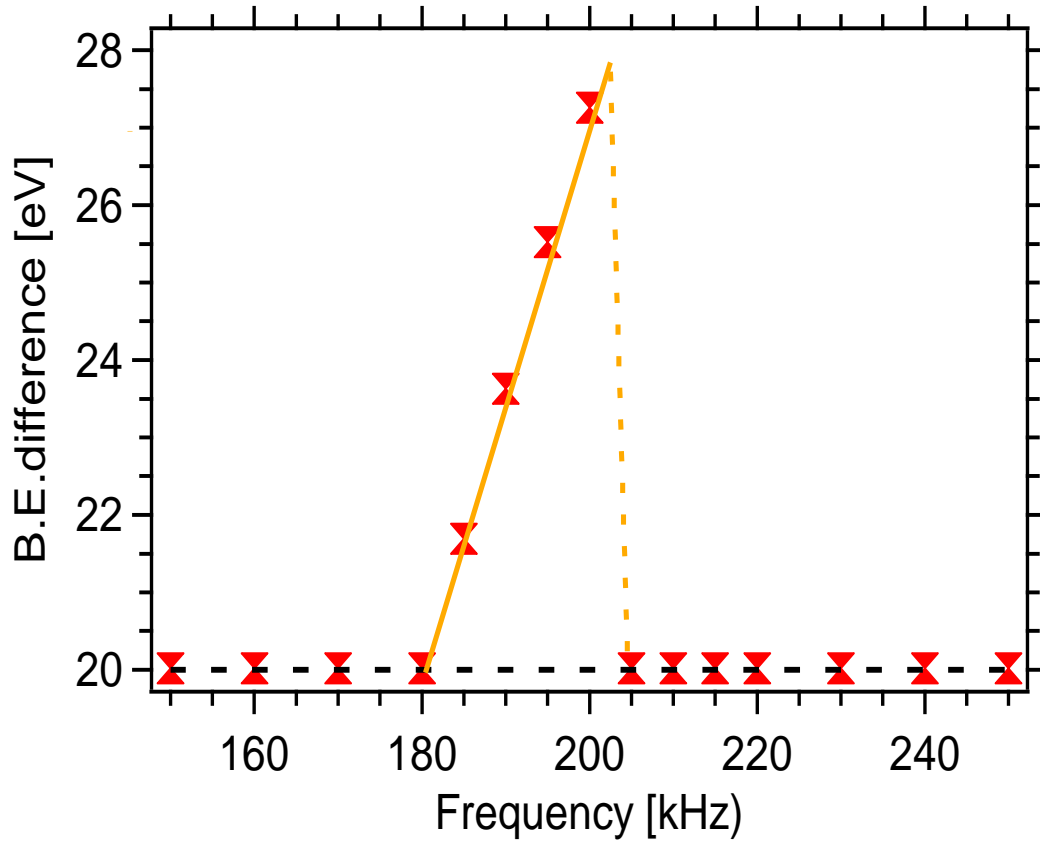


Figure 3.36 : Frequency dependence of the measured difference between the peaks like Figure 3.33 for $\text{S}_{1\text{PDS}}$

Table 3.6 : The B.E differences vs. frequency values S_{1PDS}

Freq. (kHz)	B.E Diff.(eV)
150	20
160	20
170	20
180	20
185	21.69
190	23.63
195	25.52
200	27.26
205	20
210	20
215	20
220	20
230	20
240	20
250	20

Accordingly, XPS spectra of the S_{1PDS} sample with nanosandwiches functionalized with thiol-terminated polymer were recorded under positive and negative pulses (± 10 V with SQW) with different frequencies. The highest binding energy difference was measured 27.2 eV for S_{1PDS} because of the PDS polymer bound on the Au layers. From Figure 3.36, the measured binding energy shift was observed nonlinear because of the different numbers of electrons that can be passed to the surfaces depending on the frequency levels (Dane et al., 2006).

When the S_{1PDS} sample is subjected to the negative pulses (-10V), the electrons which come from the function generator were neutralized by being negatively charged. Thus, the photoemitted electrons from the surface shift the binding energy position of the peaks -15eV lower than its grounded position. Meanwhile, when the positive pulses (+10V) are exposed to the S_{1PDS} sample, the low energy electrons were neutralized by the positive charging and the photoelectron peak position was shifted from grounded position to +12.6eV (Karabudak et al., 2006). Thus, the measured binding energy difference increased from 185 to 200 kHz due to the charging capacity of the surface; while the binding energy difference decreased to the initial 20 eV level when the frequency is increased above 200 kHz due to the discharging properties of the S_{1PDS} sample as shown in Table 3.6. The differential charging in XPS is used as a means to identify electrical parameters like capacitance

and dielectric properties of nanostructures in the noncontact fashion (Karabudak et al., 2006).

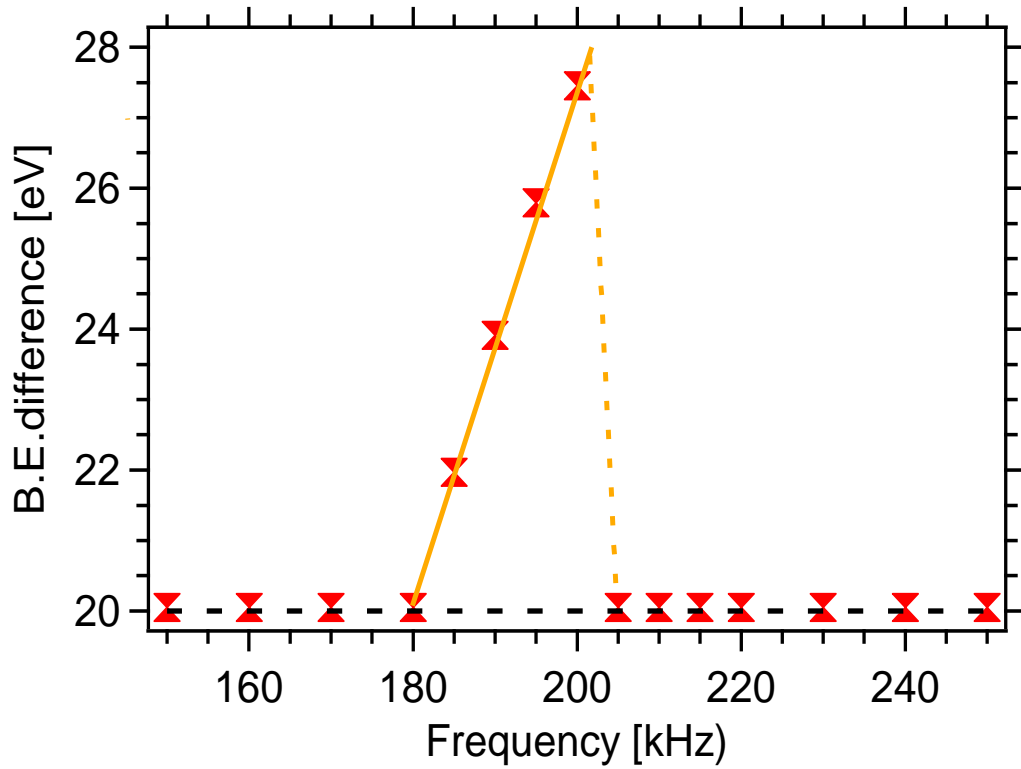


Figure 3.37 : The measured B.E difference was plotted against the frequency for $S_{1PDS+PHO}$

Table 3.7 : The B.E differences Vs. frequency values $S_{1PDS+PHO}$

Freq. (kHz)	B.E Diff. (eV)
150	20
160	20
170	20
180	20
185	21.97
190	23.91
195	25.79
200	27.45
205	20
210	20
215	20
220	20
230	20
240	20
250	20

In Figure 3.37, the measured binding energy difference of the XPS measurements were plotted which were recorded by using $\pm 10\text{V}$ amplitude of SQW pulses with different frequencies for $S1_{\text{PDS+PHO}}$ sample. This sample consists of nanosandwiches which are functionalized with PHO and PDS polymers to their specific layers of Al_2O_3 and Au respectively. For this sample, the highest binding energy difference is 27.45 eV at 200 kHz as result of the charging and it returns to its initial value of 20 eV at 205 kHz through discharging.

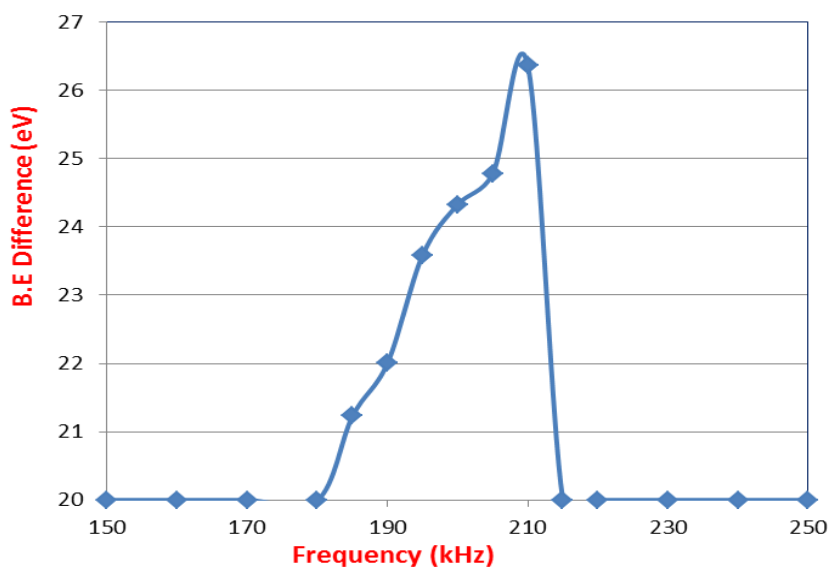


Figure 3.38 : The measured B.E difference was plotted against the frequency for $S1_{\text{SA}}$

Table 3.8 : The B.E differences vs. frequency values for $S1_{\text{SA}}$

Freq. (kHz)	B.E Diff. (eV)
150	20
160	20
170	20
180	20
185	21.23
190	22.01
195	23.59
200	24.33
205	24.78
210	26.36
215	20
220	20
230	20
240	20
250	20

Charging/ discharging properties of the S_{ISA} was examined under application of the SQW pulses (± 10 voltage) with various frequencies as shown in Table 3.8. From Figure 3.38, the binding energy difference between XPS peaks of S_{ISA} which consists of nanosandwiches (Au/ Al_2O_3 / Au) after functionalized with biotin-streptavidin complex was measured 26.36 eV with the highest binding energy difference at 210 kHz. This sample is charging between 185-210 kHz, and discharging above 210 kHz frequency. S_{ISA} has more charging/ discharging capacity than the S_1 sample, despite the fact that these two samples have identical dielectric layers of Al_2O_3 . This difference results from the binding of the biotin-streptavidin complex on the S_{ISA} . Streptavidin, being a large biomolecule, increased the charging capacity of the nanostructures (Holmberg et al., 2005). However, the highest binding energy difference of S_{ISA} sample (26.36 eV) is less than that of S_1 , (28.009 eV). This reduction of the binding energy difference is due to the differential charging of the streptavidin binding (Sezen et al., 2007).

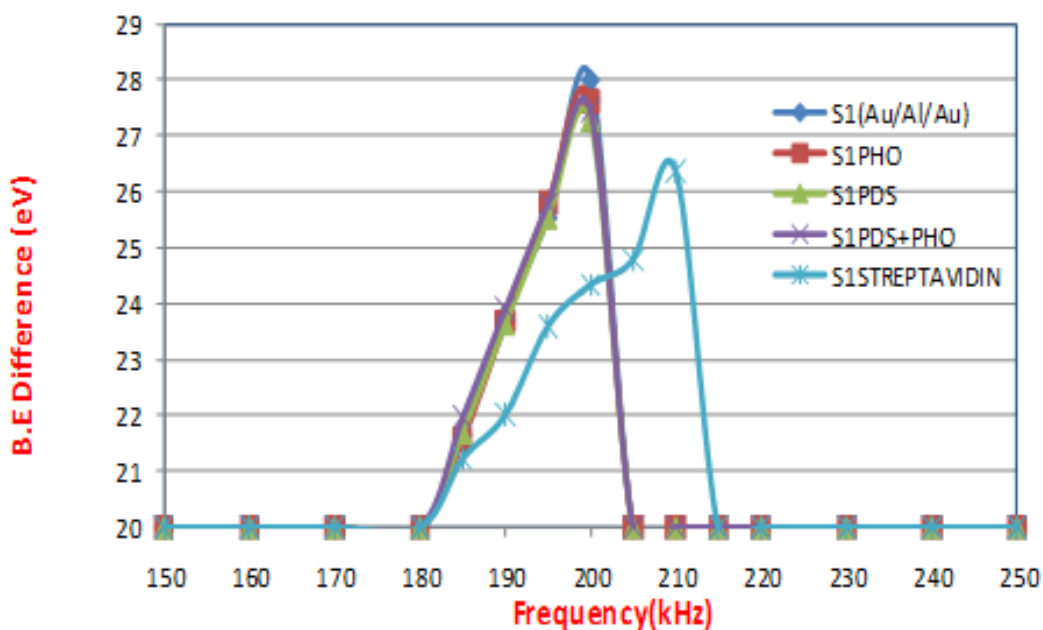


Figure 3.39 : The comparison of the binding energy difference versus frequency for the five samples which consist of Au/ Al_2O_3 / Au nanosandwiches

Table 3.9 : The comparison of the binding energy difference versus frequency for the five samples which consist of Au/ Al₂O₃/ Au nanosandwiches

Freq(kHz)	S ₁	S _{1PHO}	S _{1PDS}	S _{1PDS+PHO}	S _{1SA}
150	20	20	20	20	20
160	20	20	20	20	20
170	20	20	20	20	20
180	20	20	20	20	20
185	21.662	21.57	21.69	21.97	21.23
190	23.809	23.676	23.63	23.91	22.01
195	25.539	25.796	25.52	25.79	23.59
200	28.009	27.619	27.26	27.45	24.33
205	20	20	20	20	24.78
210	20	20	20	20	26.36
215	20	20	20	20	20
220	20	20	20	20	20
230	20	20	20	20	20
240	20	20	20	20	20
250	20	20	20	20	20

In Figure 3.39, the values of the binding energy difference and frequency for S₁, S_{1PHO}, S_{1PDS}, S_{1PHO+PDS} and S_{1SA} samples were compared in order to clarify charging/ discharging capacity of the each sample. Also, the capacitance information can be obtained from charging/ discharging properties which were achieved by the application of the SQW pulse stress (Suzer and Dâna, 2006), (Sezen et al., 2007). It is observed that S₁, which includes the nanosandwiches without functionalization, has the highest binding energy difference (28.009 eV), hence the highest charging capacity. Since the S_{1PDS}, S_{1PHO} and S_{1PDS+PHO} samples are covered with polymers their highest binding energy differences are lower than S₁, due to the reduced charging capacities. From Figure 3.39, S_{1SA} sample has the lowest binding energy difference (also the lowest charge capacity) of the five samples, because of the binding of the streptavidin biomolecule. This is because the binding of streptavidin to the biotin is the strongest, noncovalent, and biological interaction on the surface (Weber et al., 1989), (Graves et al., 1990). The strength and reliability of the streptavidin structure blockades the surface and reduces the photo-emitted electrons, thereby reducing the differential charging of the surface.

Next, the remaining four samples which consist of Au/ HfO₂/ Au nanosandwiches were analyzed with XPS when the SQW pulses ($\pm 10V$) are subjected to the samples from 150 to 250 kHz for examining charging/ discharging properties.

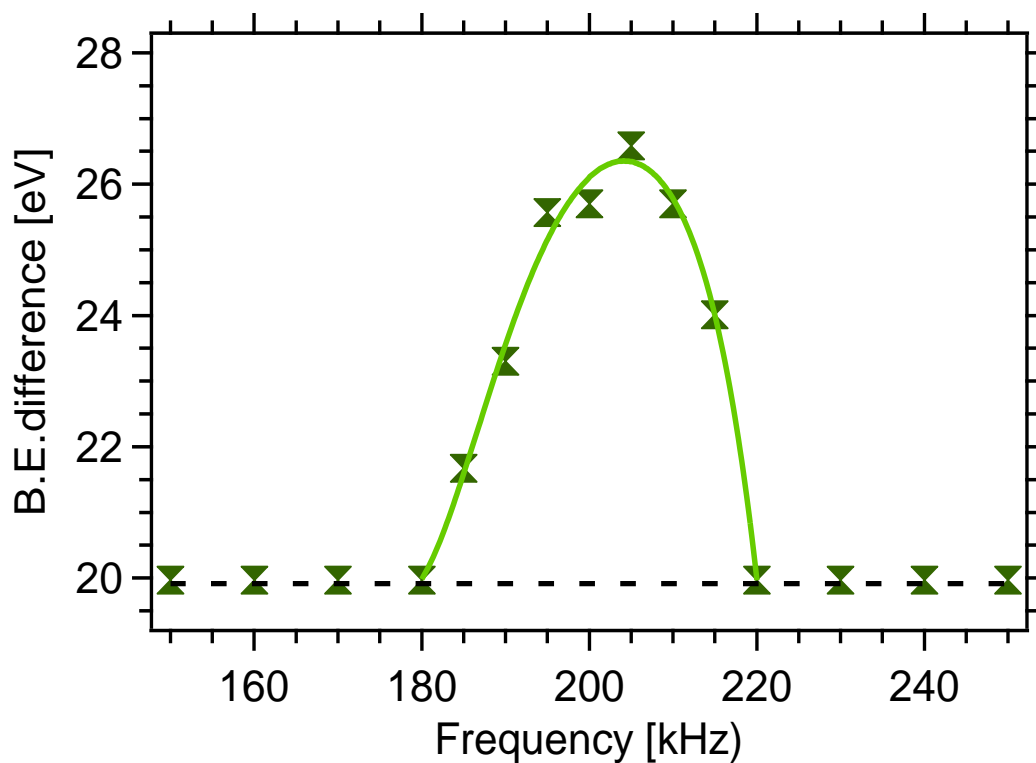


Figure 3.40 : The measured B.E difference was plotted against the frequency for S₂(Au/ HfO₂/ Au nanosandwiches).

Table 3.10 : The B.E differences vs. frequency values for S₂.

Freq.(kHz)	B.E Diff (eV)
150	20
160	20
170	20
180	20
185	21.67
190	23.3
195	25.57
200	25.7
205	26.58
210	25.7
215	24.01
220	20
230	20
240	20
250	20

Firstly, from Figure 3.40, when the frequency is changed from 150 up to 180 kHz, the binding energy difference did not change as expected (we applied 20 eV) for S₂. Then, when the frequency is increased to 185 kHz, the binding energy difference starts to increase and it continues to increasing until 205 kHz. When the frequency is at 205 kHz, the binding energy difference reaches its peak of 26.58 as shown in Table 3.10 because the sample was charged due to the dielectric material which is HfO₂ in this case (Suzer, 2003). In Figure 3.40, when the frequency increases to 210 and 215 kHz, the binding energy difference goes down to 25.7 and 24.01 eV, respectively. Yet, it went down to the initial 20 eV when the frequency goes up to 220 kHz and remains at 20 eV when the frequency is further increased. Thus, we can clearly say that S₂ sample is charging between 185-215 kHz, and discharging after 215 kHz. This charging/ discharging matter is resulted from the differential charging of the dielectric layer (HfO₂) (DEMIROK, 2005), (Sezen et al., 2007).

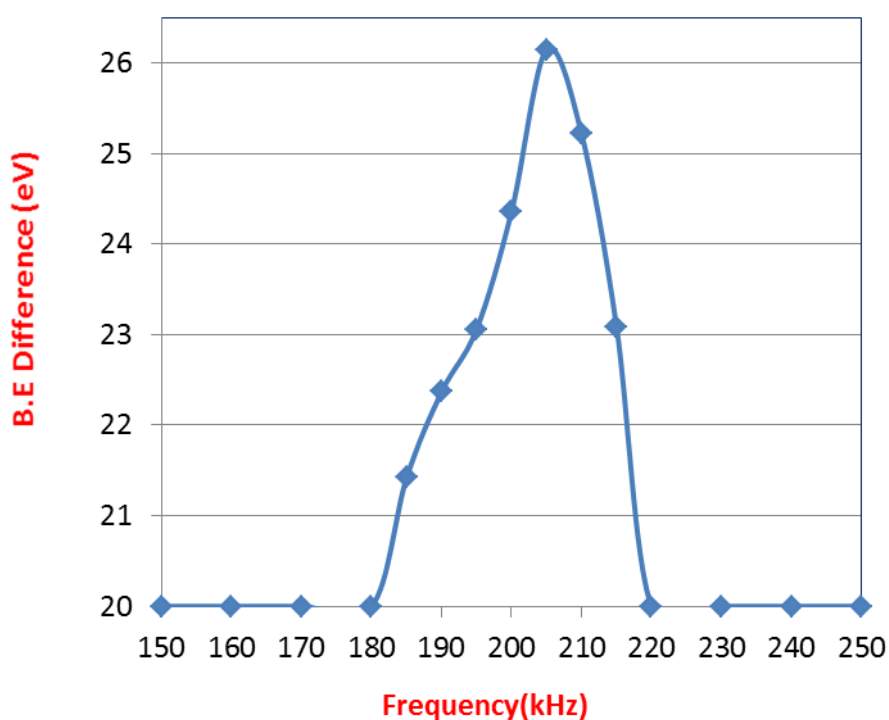


Figure 3.41 : The measured B.E difference was plotted vs against frequency for S_{2PDS}

Table 3.11 : The B.E differences frequency values for S₂PDS

Freq(kHz)	B.E Diff.(eV)
150	20
160	20
170	20
180	20
185	21.42
190	22.37
195	23.06
200	24.36
205	26.15
210	25.22
215	23.09
220	20
230	20
240	20
250	20

XPS results of S₂PDS with the nanosandwiches functionalized with thiol-terminated polymer were obtained while applying ± 10 V amplitude of SQW pulses with different frequencies as shown in Table 3.11. From Figure 3.41, the highest binding energy difference is measured as 26.15 eV at 205 kHz. This measured value is smaller than S₂ sample where the nanosandwiches were unfunctionalized. Moreover, when the frequency goes up to 220 kHz, the binding energy difference goes down to the initially applied level of 20 eV. This sample is charging from 185 to 215 kHz, and discharging after 215 kHz. The polymer binding affected the differential charging on the S₂PDS, and the polymer which was bound to the Au layers decreased the highest binding energy difference to a lower level when compared to the S₂(Au/HfO₂/Au nanosandwiches without functionalization). When the charging capacity was decreased due to the differential charging of the nanostructures, the capacitance value of the sample also decreases.

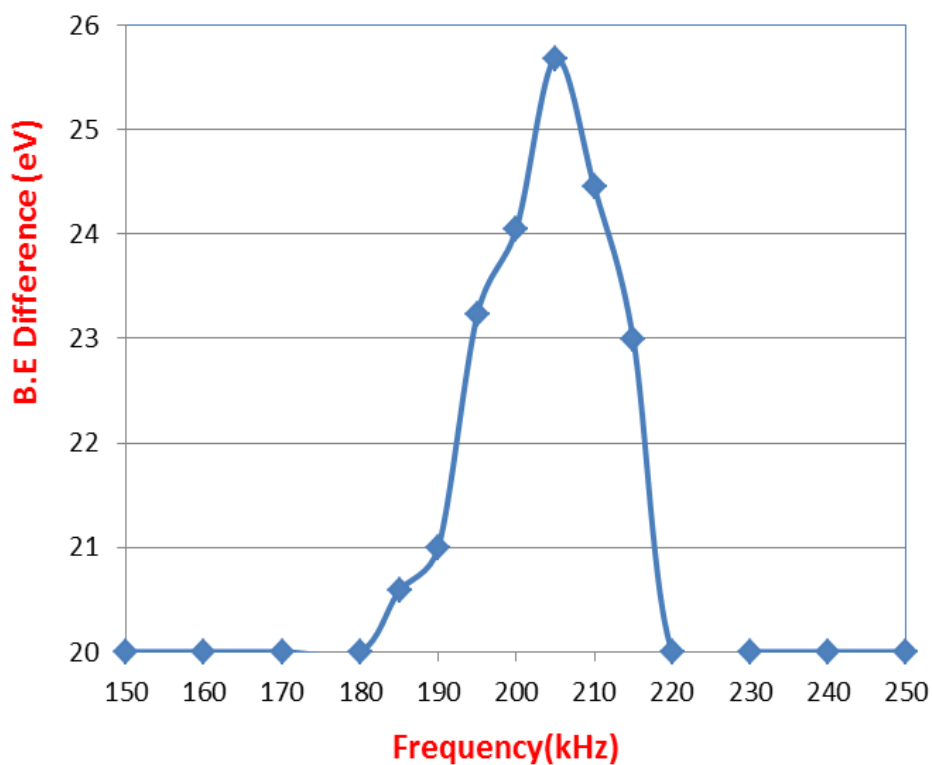


Figure 3.42 : The measured B.E difference was plotted vs against frequency for S_{2ATES}

Table 3.12 : The B.E differences frequency values for S_{2ATES}

Freq.(kHz)	B.E Diff.(eV)
150	20
160	20
170	20
180	20
185	20.59
190	21
195	23.23
200	24.05
205	25.68
210	24.45
215	22.99
220	20
230	20
240	20
250	20

S_{2ATES} with nanosandwiches after functionalized with silane-terminated polymer is subjected to the ± 10 voltage with SQW pulses at varying frequencies as shown in Table 3.12. When the frequency is 205 kHz, the binding energy difference reaches its

peak of 25.68 eV. And, when the frequency goes up to 220 kHz, the binding energy difference value goes down to 20 eV, which equals the total applied SQW pulses. From Figure 3.42, this sample's charging capacity was observed between 185-215 kHz; after 215 kHz the sample was discharged due to the characteristic of the surface. Thus, the charging capacity of S_{2ATES} is less than S_2 . Despite containing the same dielectric materials, these two samples have different charging capacities due to the fact that the surface of S_{2ATES} is covered with polymer, which reduces its charging capacity due to reduced number of stray electrons that can penetrate into the sample.

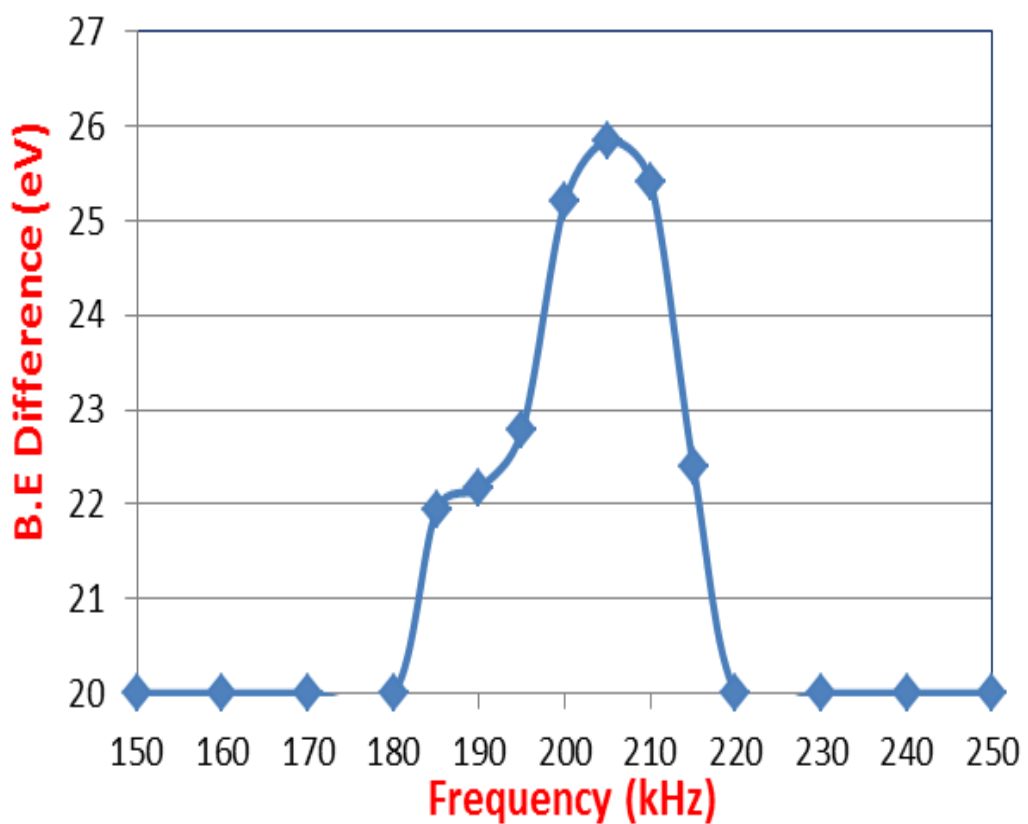


Figure 3.43 : The measured B.E difference was plotted against frequency for $S_{2PDS+ATES}$

Table 3.13 : The B.E differences vs frequency values for S_{2PDS+ATES}

Freq. (kHz)	B.E Diff. (eV)
150	20
160	20
170	20
180	20
185	21.94
190	22.17
195	22.79
200	25.2
205	25.85
210	25.41
215	22.4
220	20
230	20
240	20
250	20

The same XPS process was repeated for S_{2PDS+ATES} sample with thiol-terminated and silane-terminated polymers bound to the layers of Au and HfO₂ respectively and the highest binding energy difference was measured at 25.85 eV which is more than the applied total amplitude of the SQW pulses at 205 kHz as shown in Table 3.13. From Figure 3.43, when the frequency is increased to 220 kHz, the binding energy difference returns to its initial value of 20 eV. As a result, electrical potentials were extracted due to the charging of the samples under SQW pulses depending on the frequency. This way, the sample is charging between 205-215 kHz and discharging after 215 kHz. The highest binding energy difference of S_{2PDS+ATES} is measured at 25.85 eV which is less than that of S₂. The capacitance property of this sample is decreased due to the binding of the PDS and ATES polymers to the surface.

From Figure 3.44, the differential charging of S₂, S_{2PDS}, S_{2ATES}, S_{2ATES+PDS} samples which include Au/ HfO₂/ Au nanosandwiches can be compared by looking at the binding energy differences based on the frequency levels. Thus, we obtain the capacitance values of these samples based on the chemical specificity of the surfaces (Sezen et al., 2007).

When we measured the binding energy difference values of the four samples, the highest binding energy difference is observed 26.58 eV at 205 kHz for S₂ sample which has nanosandwiches without functionalization. Remaining samples of S_{2PDS}, S_{2ATES} and S_{2PDS+ATES} which have nanosandwiches after functionalized with thiol and

silane terminated polymers have lower binding energy differences when compared to the unfunctionalized sample, as tabulated below. The reason for this decrease is the fact that the surfaces of these three samples were covered by polymers due to the differential charging of the samples. As a result of the XPS data, differential charging can give us the capacitance properties of the samples. Thus, from Figure 3.44, it is understood that the S₂ sample shows more capacitance properties compared to the other polymer covered samples.

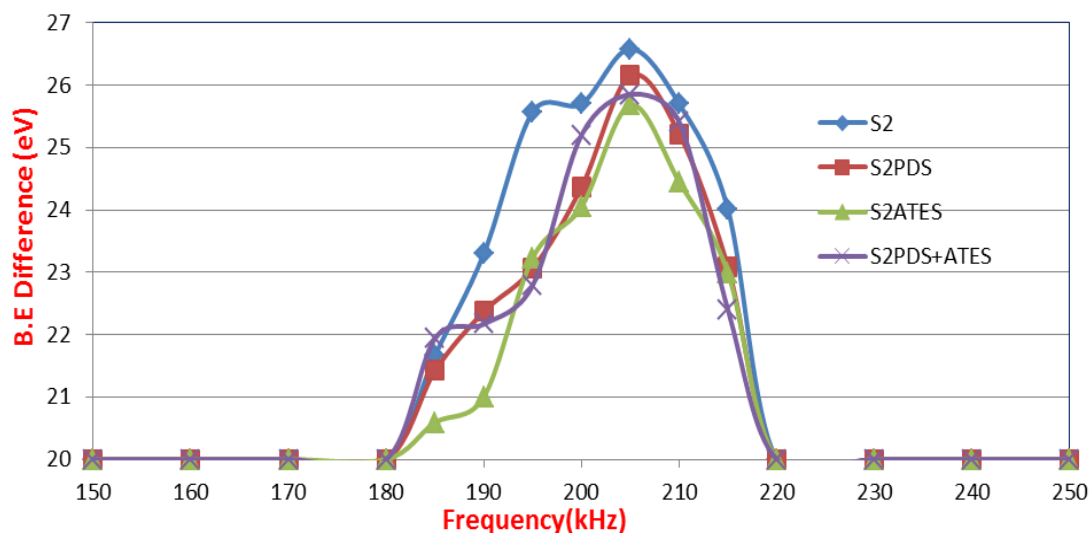


Figure 3.44 : The comparison of the binding energy difference versus frequency for the five samples which consist of Au/ HfO₂/ Au nanosandwiches.

Table 3.14 : The comparison of the binding energy difference versus frequency for the five samples which consist of Au/ HfO₂/ Au nanosandwiches.

Frequency(kHz)	S ₂	S ₂ PDS	S ₂ ATES	S ₂ PDS+ATES
150	20	20	20	20
160	20	20	20	20
170	20	20	20	20
180	20	20	20	20
185	21.67	21.42	20.59	21.94
190	23.3	22.37	21	22.17
195	25.57	23.06	23.23	22.79
200	25.7	24.36	24.05	25.2
205	26.58	26.15	25.68	25.85
210	25.7	25.22	24.45	25.41
215	24.01	23.09	22.99	22.4
220	20	20	20	20
230	20	20	20	20
240	20	20	20	20
250	20	20	20	20

Capacitors in conventional electronic circuits perform essential functions such as storing electrical charge and blocking direct current while allowing alternating currents to propagate (Shiraki et al., 2006). In this thesis, we fabricated ordered arrays of Au/ Al₂O₃/ Au and Au/ HfO₂/ Au nanosandwiches by using NSL in order to construct capacitor for quantitative measurements of biomolecular interaction by using an XPS technique as described below (from Tubitak report).

A series of XPS measurements were recorded by subjecting the nine samples (particularly the Au, C, O, Si regions of each sample) to SQW pulses (± 10 V) under different frequencies. Changing the polarity of the bias (SQW pulses) affects the differential charging (Suzer et al., 2007). This differential charging in XPS is used for understanding the capacitance properties of nanostructures (Suzer, 2003). This technique is used to investigate transient charging/ discharging properties of insulating materials or devices such as nanocapacitors (Zareie et al., 2008a).

From Figure 3.45, when we compare the binding energy differences of all samples, we can see the difference between the capacitance properties of Au/ Al₂O₃/ Au nanosandwiches (S₁, S_{1PHO}, S_{1PDS}, S_{1PHO+PDS}, S_{1SA}) and Au/ HfO₂/ Au nanosandwiches (S₂, S_{2PDS}, S_{2ATES}, S_{2PDS+ATES}). However, Al₂O₃ and HfO₂ layers are dielectric materials that have different dielectric constants of 9.4 and 25, respectively (King, 1963), (Zareie et al., 2008a), (Javey et al., 2002). Since the dielectric constant of HfO₂ is greater than that of Al₂O₃, its nanosandwiches show capacitance properties in a wider range of frequency. The range of frequency for samples that include HfO₂ is observed between 185-215 kHz, as opposed to the range of 185-200 kHz for nanosandwiches that contain Al₂O₃ dielectric materials. We have demonstrated that each of the nanocapacitors have the charging capacity at specific frequency ranges by using XPS under SQW pulses. Therefore, we conclude that our nine samples tabulated below act as capacitive devices (Zareie et al., 2008a).

Table 3.15 : The comparison of the binding energy differences per different frequencies for nine samples which consist of Au/ Al₂O₃/ Au nanosandwiches and Au/ HfO₂/Au nanosandwiches

Freq.(kHz)	S ₁	S _{1PHO}	S _{1PDS}	S _{1PDS+PHO}	S ₂	S _{2PDS}	S _{2ATES}	S _{2ATES+PDS}	S _{1SA}
150	20	20	20	20	20	20	20	20	20
160	20	20	20	20	20	20	20	20	20
170	20	20	20	20	20	20	20	20	20
180	20	20	20	20	20	20	20	20	20
185	21.662	21.57	21.69	21.97	21.67	21.42	20.59	21.94	21.23
190	23.809	23.676	23.63	23.91	23.3	22.37	21	22.17	22.01
195	25.539	25.796	25.52	25.79	25.57	23.06	23.23	22.79	23.59
200	28.009	27.619	27.26	27.45	25.7	24.36	24.05	25.2	24.33
205	20	20	20	20	26.58	26.15	25.68	25.85	24.78
210	20	20	20	20	25.7	25.22	24.45	25.41	26.36
215	20	20	20	20	24.01	23.09	22.99	22.4	20
220	20	20	20	20	20	20	20	20	20
230	20	20	20	20	20	20	20	20	20
240	20	20	20	20	20	20	20	20	20
250	20	20	20	20	20	20	20	20	20

3.6 Connection of External Resistance

In the previous parts, the electrical responses of nine metal-insulator samples were analyzed with the help of XPS. As a result of a series of experiments we demonstrated that our nine samples consisting of different layers of nanosandwiches have capacitance properties on the surfaces. Furthermore, we need to calculate the capacitance values of these samples both experimentally (real) and theoretically.

In this section, an external resistance of $10\text{ M}\Omega$ was connected to the samples (which are considered as nanocapacitors) under SQW pulses ($\pm 10\text{V}$) with different frequencies (while the flood gun was turned on). These connections are shown in Figure 3.45 below.

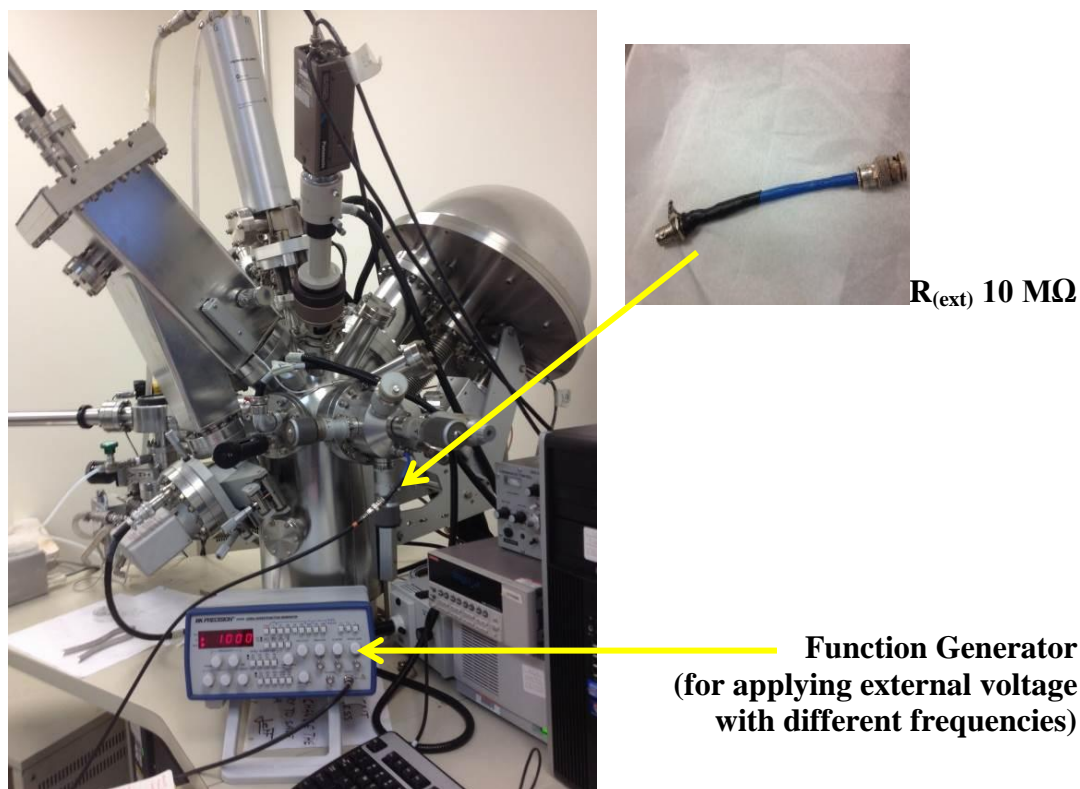


Figure 3.45 : Connecting an external resistance ($10\text{M}\Omega$) between the samples (inside XPS) and function generator.

From Figure 3.45, a simple RC circuit is created with the help of a resistor and a function generator. The goal of creating the RC circuit in this thesis is to understand the behavior of the samples' capacitance values. The nine samples were examined again with XPS under ($\pm 10\text{V}$) SQW pulses and (0.1 Hz to 10 kHz) frequencies by

connecting a 10M Ω resistance between the samples and function generator. It is observed that the distance between the separated two XPS peaks (due to the application of ± 10 voltage to the samples) were decreased when the frequencies are increased from 0.1 Hz to 1000 Hz as shown in Figure 3.46, Figure 3.47. The distance between the peaks was measured for Au/ Al₂O₃/ Au and Au/ HfO₂/ Au nanosandwiches which are shown in Table 16 and 17 respectively.

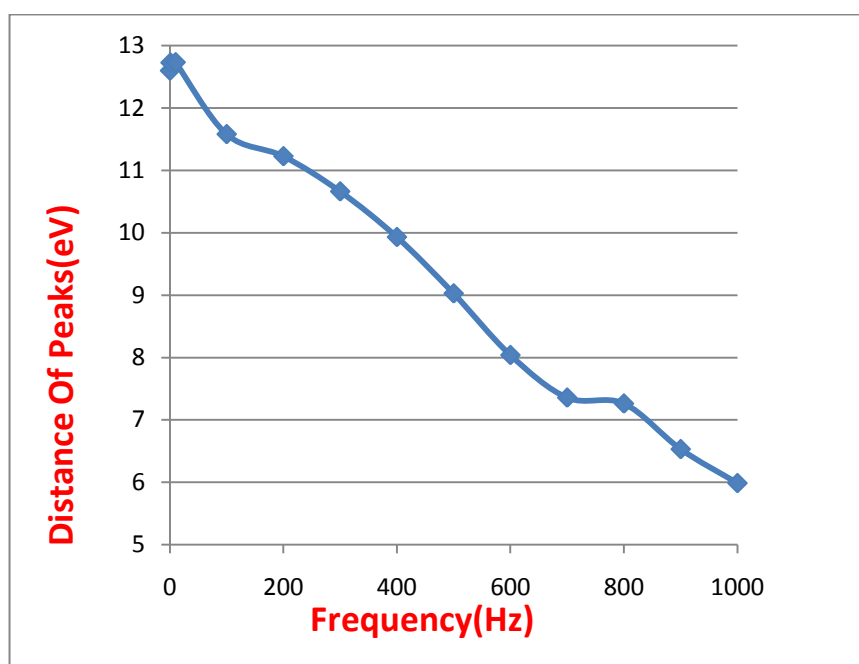


Figure 3.46 : Frequency dependence of the distance of peaks for Au/ Al₂O₃/ Au samples

Table 3.16 : The measured difference between the peaks versus frequencies for the samples which consist of Au/ Al₂O₃/ Au nanosandwiches

Freq. (kHz)	B.E Diff. (eV)
0.1	12.599
1	12.727
10	12.733
100	11.581
200	11.227
300	10.663
400	9.932
500	9.028
600	8.04
700	7.358
800	7.263
900	6.532
1000	5.987

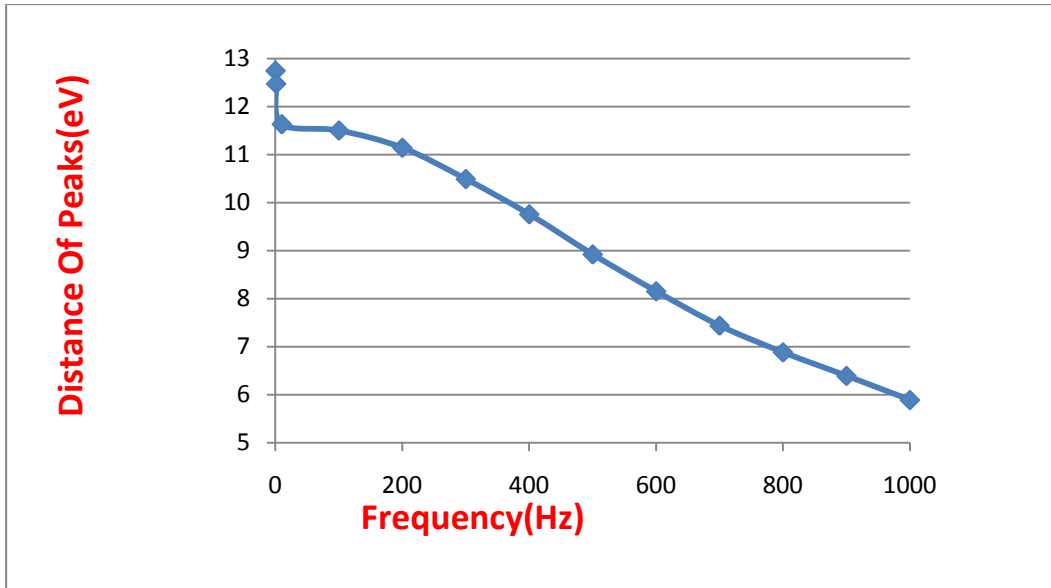


Figure 3.47 : Frequency dependence of the distance of peaks for Au/ HfO₂/ Au samples

Table 3.17 : The measured difference between the peaks versus frequency for the samples which consist of Au/ HfO₂/ Au nanosandwiches

Freq. (kHz)	B.E Diff. (eV)
0.1	12.745
1	12.474
10	11.631
100	11.501
200	11.142
300	10.49
400	9.756
500	8.921
600	8.152
700	7.437
800	6.881
900	6.39
1000	5.888

Our samples include two types of dielectric materials which are Al₂O₃ and HfO₂. These dielectric materials possess different frequency of response due to their dielectric constants. (Solymar and Walsh, 2009). So it is observed that the distance between the peaks is different for each type of dielectric materials (Al₂O₃ and HfO₂) as shown in Figure 3.46, Figure 3.47 respectively. Figure 3.48- Figure 3.67 below depicts the XPS data for Au4f region for each frequency level between 1Hz to 10 kHz (the same measurements were repeated for the Au4f, C1s, Si2p and O1s regions

on each of the nine samples; yet were not reported here in the interest of saving space).

It is observed that as the frequency for the samples continued to be increased beyond 1000 Hz, the distance between the two peaks get smaller, and around 2000 Hz it is reduced to 0 (Figure 3.59). Thus, at 2000 Hz the two peaks converge and observed as one peak, with the maximum intensity (CPS). This value is called cut-off frequency and it is observed at different specific frequency levels for each sample as listed in Table 3.18. After this cut-off frequency level, we continued to increase the frequency to 10 kHz, and it is observed that the peak stayed stable as one, as shown in the Figures 3.59 to Figure 3.67 below.

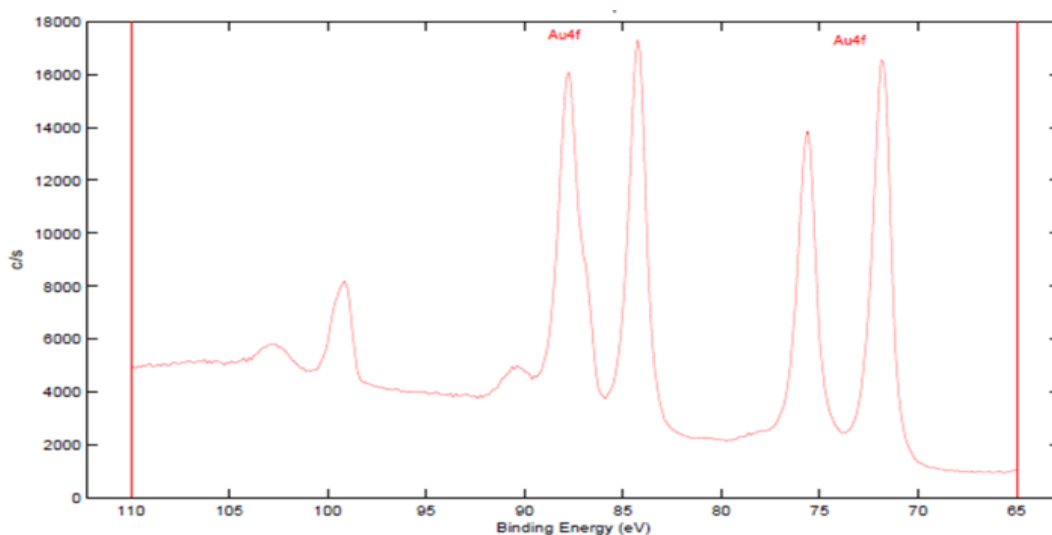


Figure 3.48 : XPS spectrum with RC at 1Hz

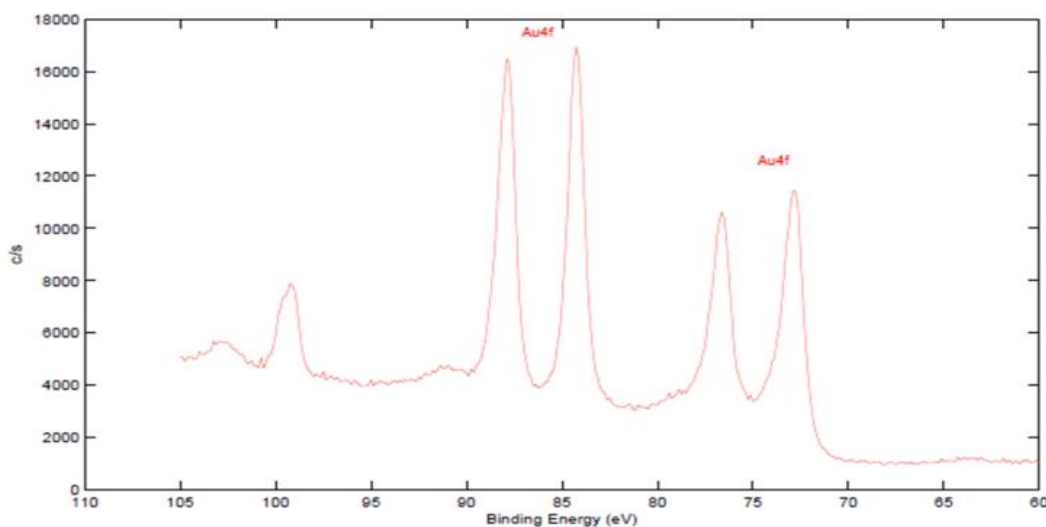


Figure 3.49 : XPS spectrum with RC at 100Hz

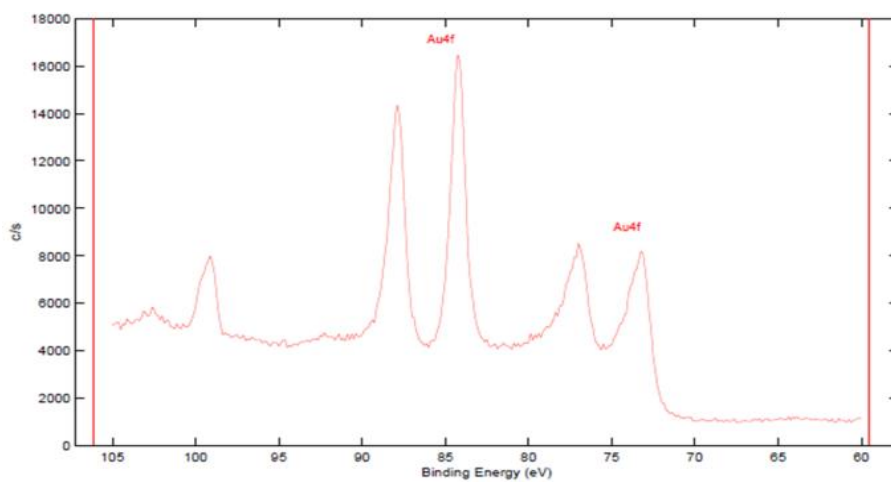


Figure 3.50 : XPS spectrum with RC at 200Hz

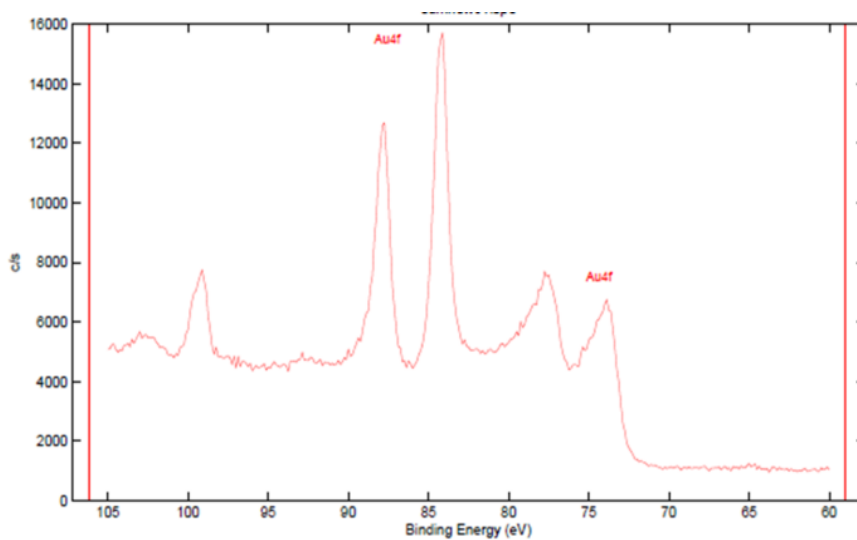


Figure 3.51 : XPS spectrum with RC at 300Hz

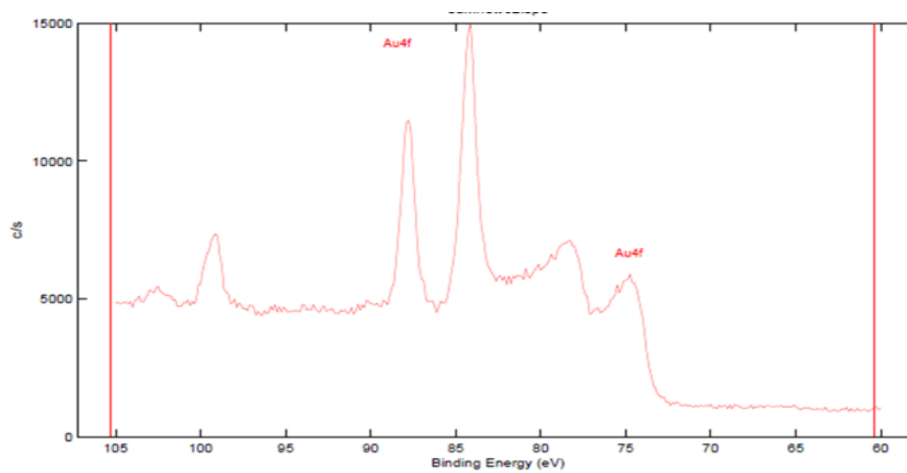


Figure 3.52 : XPS spectrum with RC at 400Hz

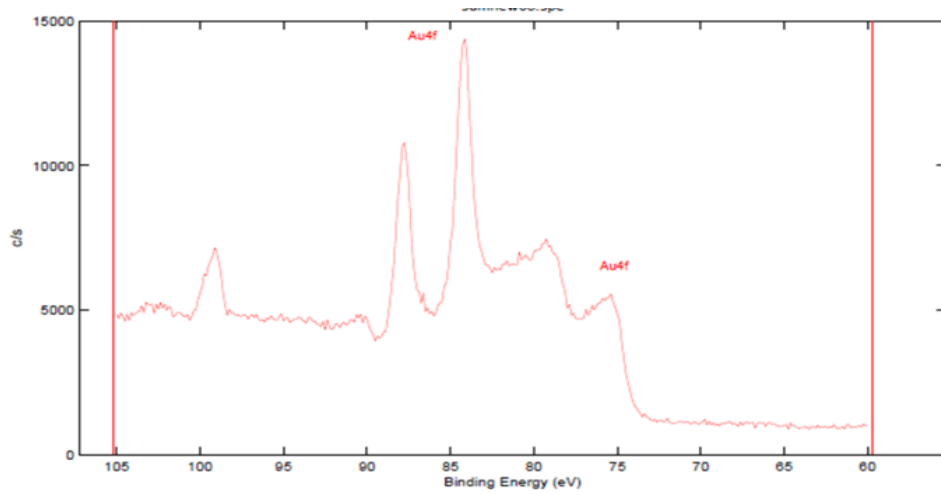


Figure 3.53 : XPS spectrum with RC at 500Hz

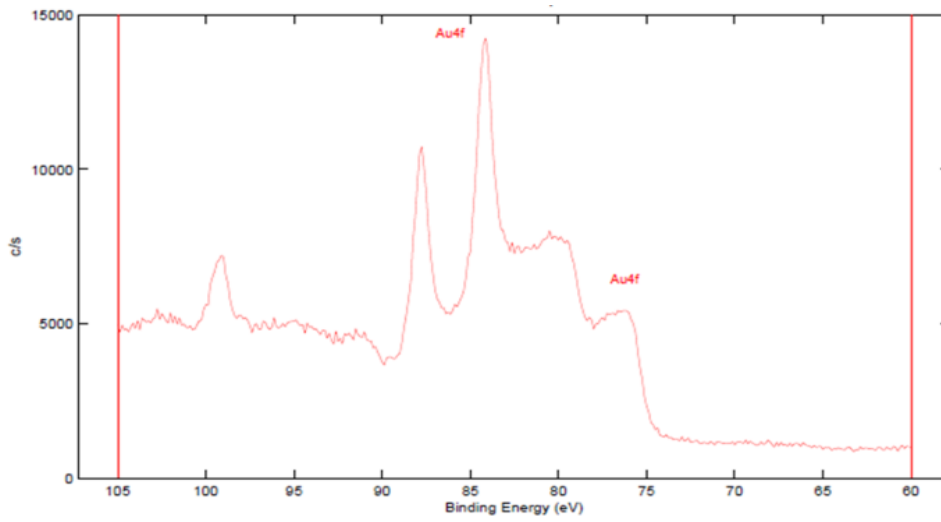


Figure 3.54 : XPS spectrum with RC at 600Hz

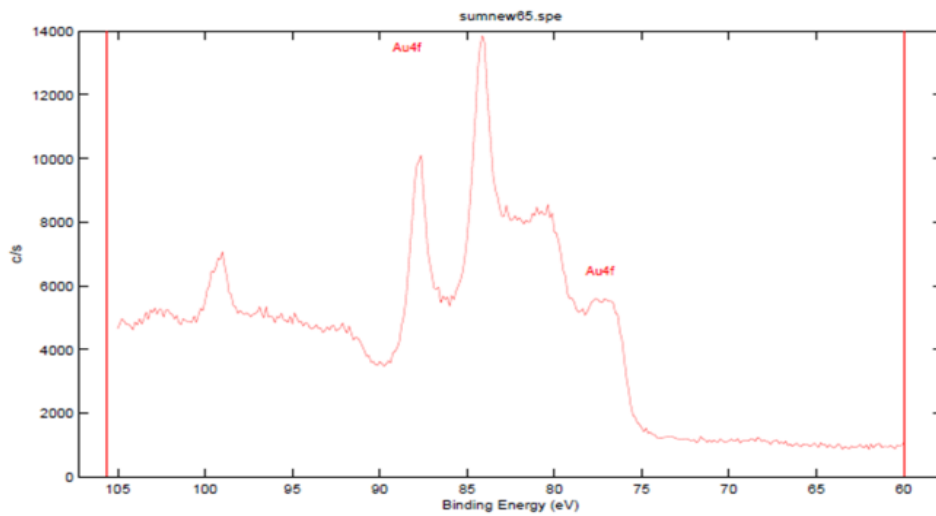


Figure 3.55 : XPS spectrum with RC at 700Hz

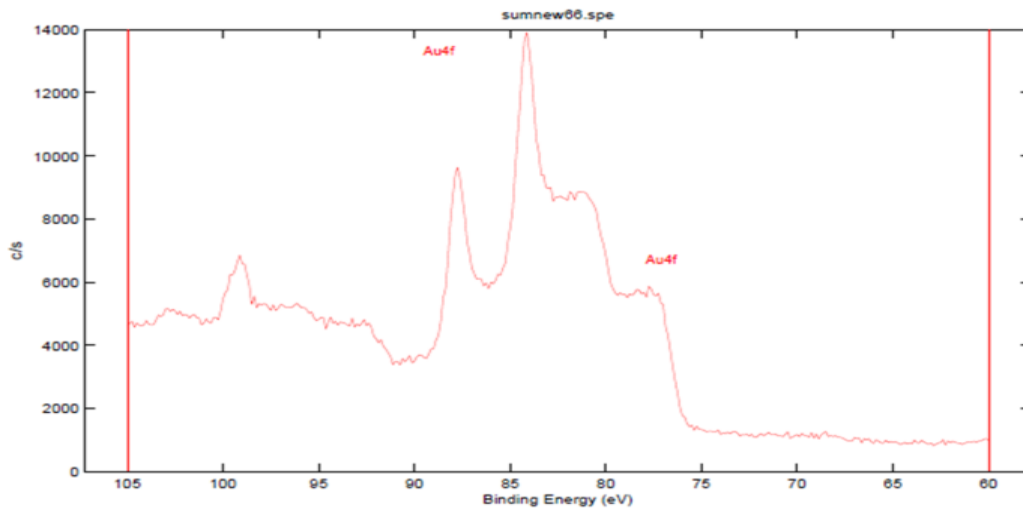


Figure 3.56 : XPS spectrum with RC at 800Hz

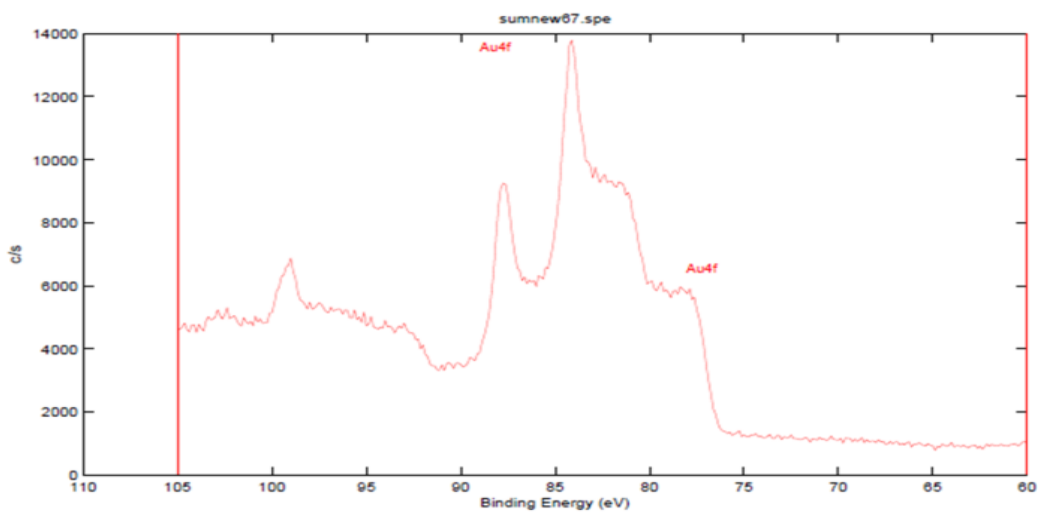


Figure 3.57 : XPS spectrum with RC at 900Hz

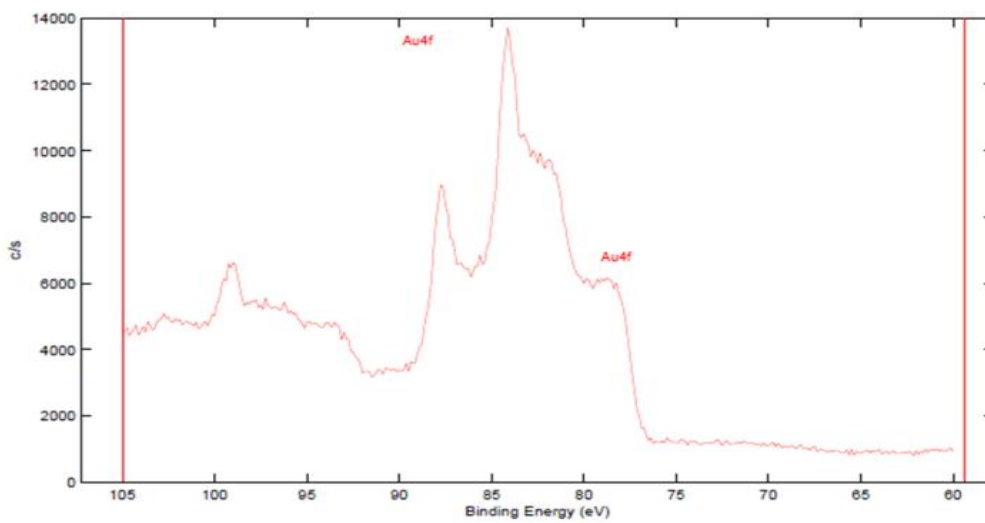


Figure 3.58 : XPS spectrum with RC at 1000Hz

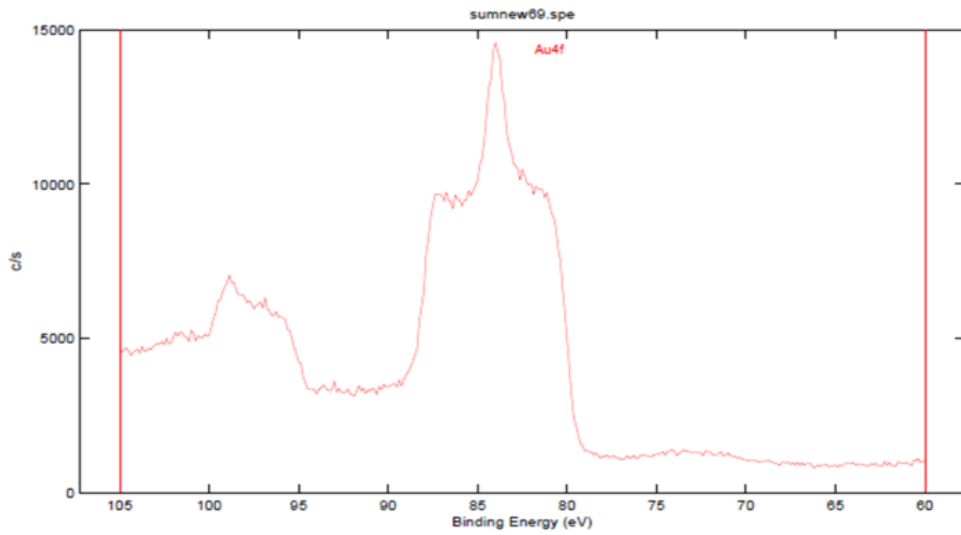


Figure 3.59 : XPS spectrum with RC at 2000Hz

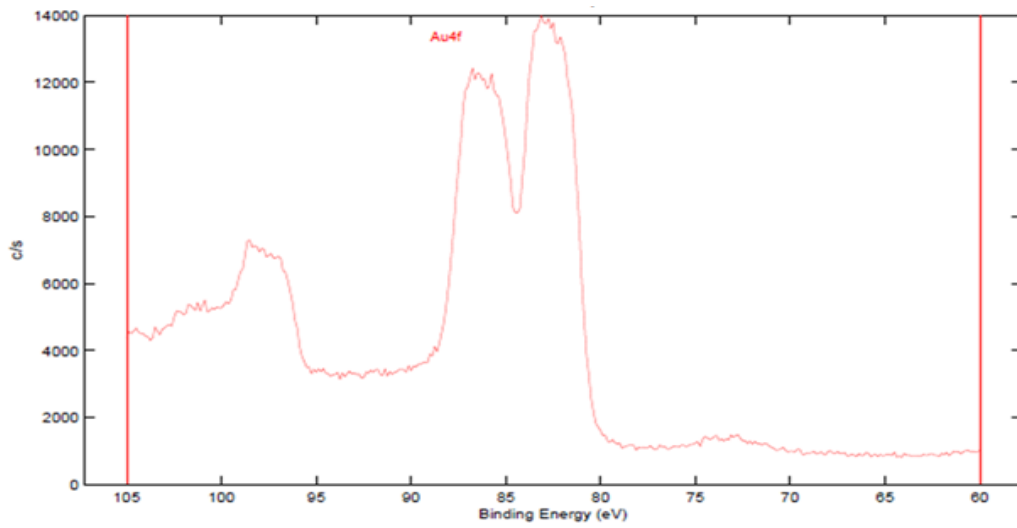


Figure 3.60 : XPS spectrum with RC at 3000Hz

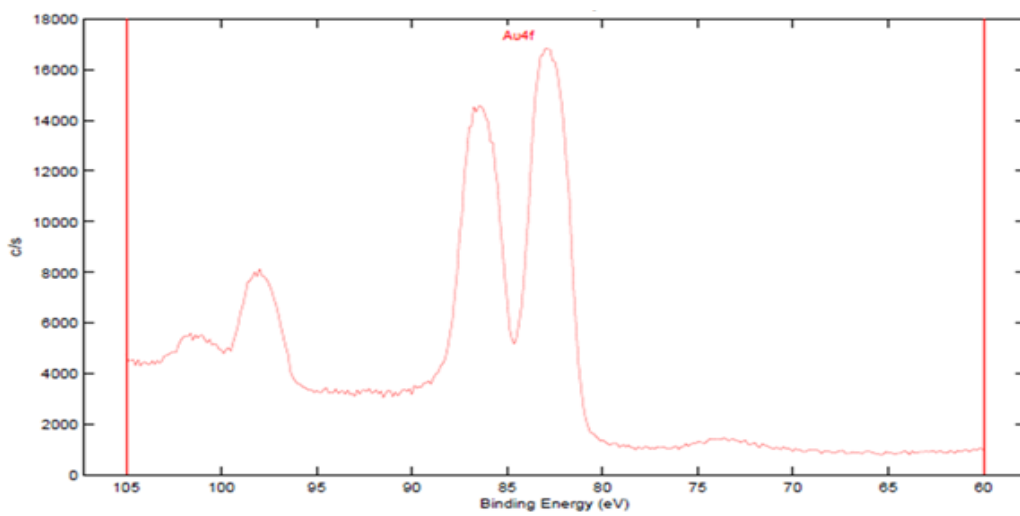


Figure 3.61 : XPS spectrum with RC at 4000Hz

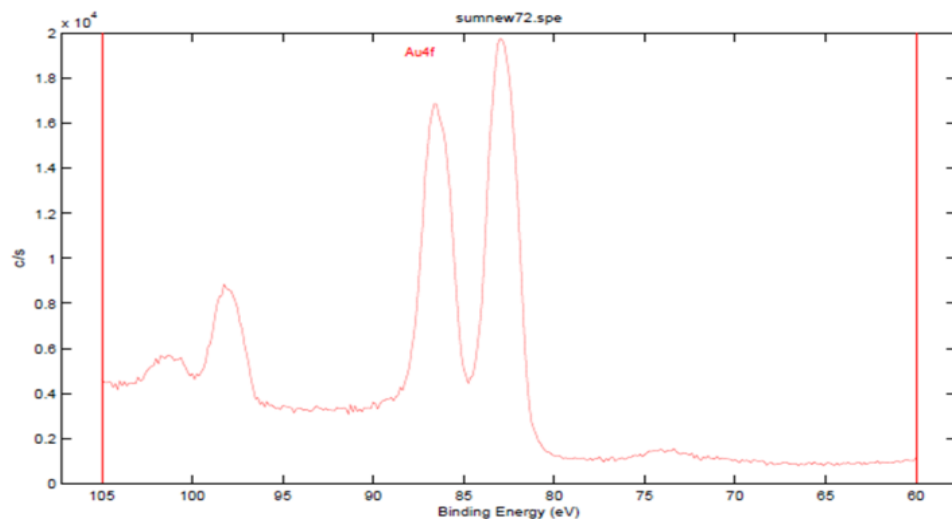


Figure 3.62 : XPS spectrum with RC at 5000Hz

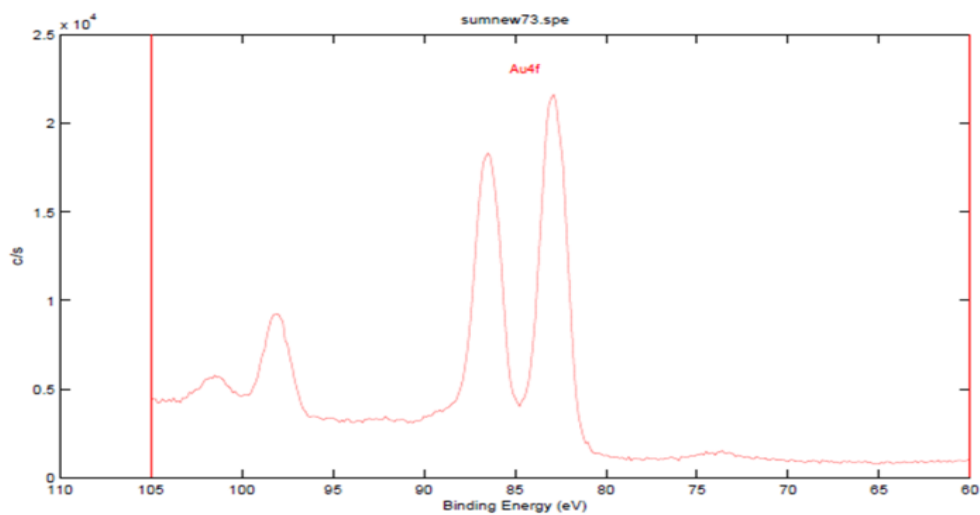


Figure 3.63 : XPS spectrum with RC at 6000Hz

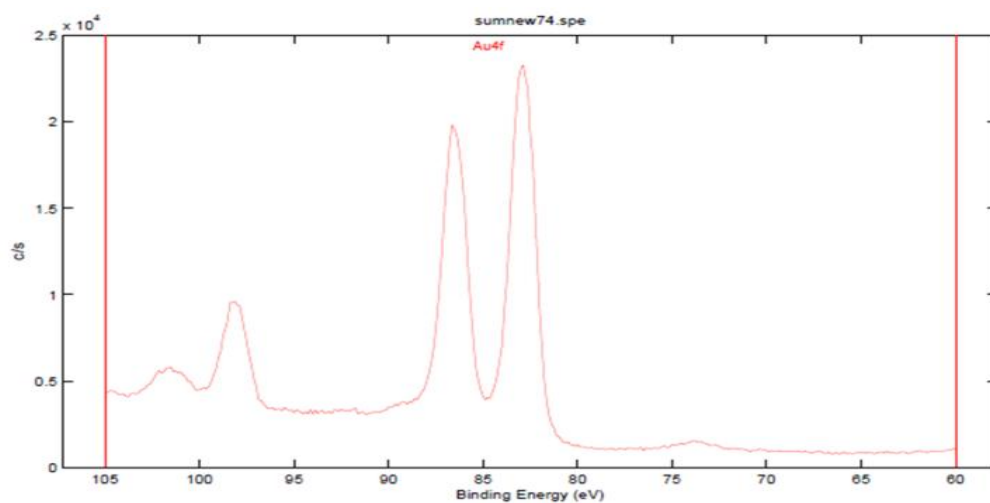


Figure 3.64 : XPS spectrum with RC at 7000Hz

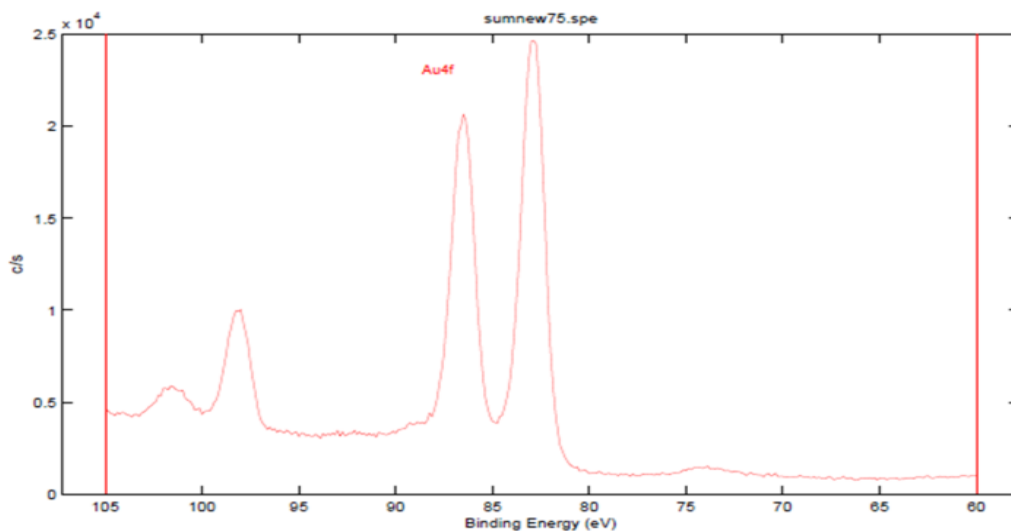


Figure 3.65 : XPS spectrum with RC at 8000Hz

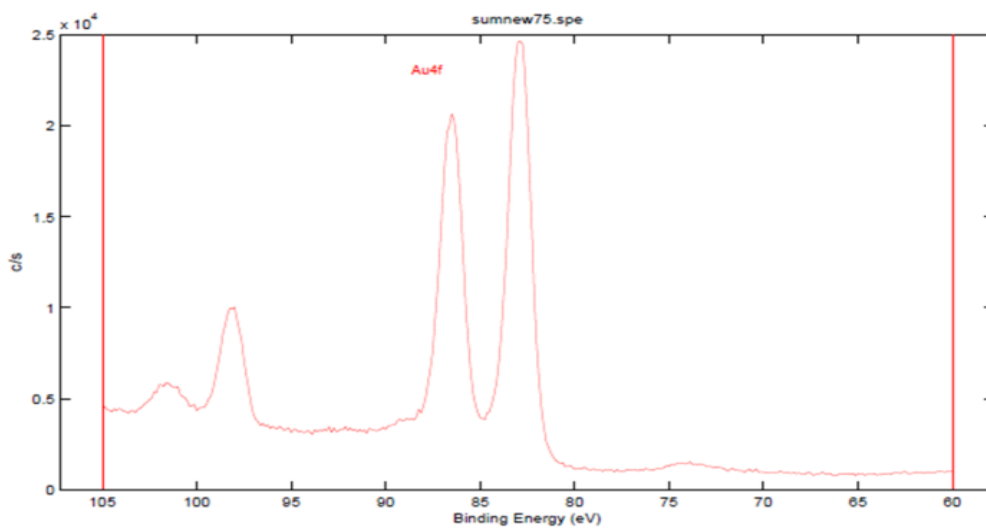


Figure 3.66 : XPS spectrum with RC at 9000Hz

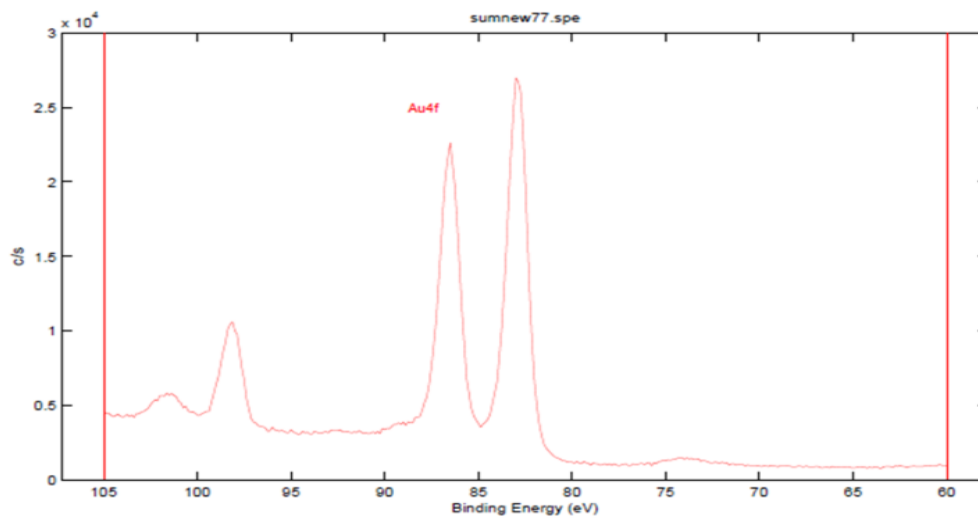


Figure 3.67 : XPS spectrum with RC at 10000Hz

XPS spectra were taken under SQW pulses by using an external resistance to determine the capacitance values of the samples depicted above (Neuendorf et al., 2001). The cut-off frequencies that are identified with the help of 10M Ω helped us calculate the experimental and theoretical capacitance values of our samples (Neuendorf et al., 2001).

3.7 Calculation of Capacitance Values

In this section, the capacitance values of the samples are calculated using cutoff frequencies which were identified as explained in part 3.6 (DEMIROK, 2005). The cutoff frequency values are measured for our nine samples as shown in Table 3.18.

Table 3.18 : Cut off frequency values for samples which includes Au/ Al₂O₃/ Au and Au/ HfO₂/ Au nanosandwiches

<i>SAMPLES</i>	<i>Cut-off Frequency(Hz)</i>
<i>S₁</i>	2000
<i>S_{1PHO}</i>	2010
<i>S_{1PDS}</i>	2005
<i>S_{1PDS+PHO}</i>	2008
<i>S_{1with STREPTAVIDIN}</i>	2025
<i>S₂</i>	1800
<i>S_{2PDS}</i>	1805
<i>S_{2ATES}</i>	1815
<i>S_{2ATES+PDS}</i>	1810

It is known that a capacitor contains two conductive plates that are insulated from each other (Hyun et al., 2001). The nine samples that consist of three layers which are Au/ Al₂O₃/ Au (*S₁*, *S_{1PHO}*, *S_{1PDS}*, *S_{1PDS+PHO}*, *S_{1SA}*) and Au/ HfO₂/ Au (*S₂*, *S_{2PDS}*, *S_{2ATES}*, *S_{2ATES+PDS}*) are comprised of two conducting layers (Au) which are insulated by Al₂O₃ and HfO₂ layers (Dmitriev et al., 2007). Therefore it could be argued that our samples act like nanocapacitors (Zareie et al., 2008a).

First, the areas of nanosandwiches are calculated on the samples in order to calculate the theoretical capacitance measurements. For calculating a nanodot the following formula is used:

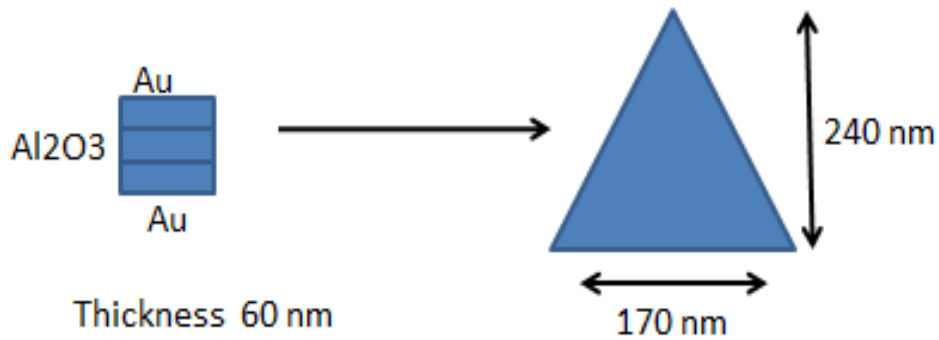


Figure 3.68 : A schematic display of a nanosandwich (Au/ Al₂O₃/ Au) which has 60 nm thickness, 240 nm height and 170 nm base.

$$\text{Area} = \frac{1}{2} \times b \times h \quad (3.1)$$

The area of the nanotriangle is half of the base times height. "b" (the distance along the base) is 170 nm, "h" (the height measured at right angles to the base) is 240nm. The area is calculated as 20,400 nm² for one nanosandwich from Equation 3.1. The total area of nanosandwiches on the sample is calculated as 8,16×10⁻¹⁰ m².

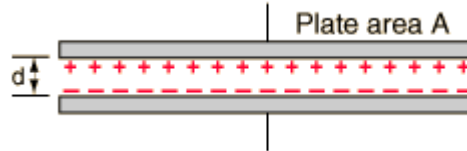


Figure 3.69 : Plate area A

$$C = \frac{\epsilon A}{d} = \frac{k\epsilon A}{d} \quad (3.2)$$

The theoretical capacitance value (C) of the samples are derived from Equation 3.2. The thickness of the dielectric material "d" is 2,0×10⁻⁸ m, the area of the capacitor "A" is 8,16×10⁻¹⁰ m², the permittivity of the vacuum "C₀" is 8,854×10⁻¹² F/m, the dielectric constants of the materials "k" are 9,4 and 25 for Al₂O₃ and HfO₂, respectively. (Lide, 2004). The theoretical capacitance values are calculated for the nine samples, where the unit of measurement is farad "F".

$$f_c = \frac{1}{2\pi RC} = \frac{1}{2\pi\tau} \quad (3.3)$$

The real (experimental) capacitance values (C) of the samples are calculated by using Equation 3.3. The cutoff frequency value “*f_c*” is different for each sample and its unit is “Hz”. An external resistance “R” of 10⁷Ω (ohm) is applied to all the samples, which allows us to calculate the real capacitance values.

The real and theoretical capacitance values of the samples are calculated for the nine samples dependent on the insulating materials used and different cutoff frequency values. From Table 3.19, the program we created in Excel allows us to calculate the real and theoretical capacitance values by changing the parameters according to the cut-off frequencies and dielectric constants of the samples.

Table 3.19 : An excel program for calculation of the real and theoretical capacitance values

Cut Off Frequency	2000	1/s
Resistance	10000000	Ohm
<u>Real Capacitance</u>	7.96178E-12	Farad
	0.007961783	nF
	7.961783439	pF

<u>Theoretical Capacitance</u>				
AREA	8.16E-10	m2	E0	8.854E-12
Dielectric Thickness	20	nm	m	0.00000002
Relative Permittivity	9.4	SI		
Capacitance	3.39569E-12	F		
	0.003395686	nF		
	3.39568608	pF		

3.8 Comparison of Theoretical and Experimental Capacitance Values

In this section, the samples examined in the previous sections are compared based on their real and theoretical capacitance values. These capacitance values were calculated by using the programs in Table 3.19, and listed below in Table 3.20.

Table 3.20 : Experimental and theoretical capacitance values of the nine samples

<i>SAMPLES</i>	<i>Real Capacitance(Farad)</i>	<i>Theoretical Capacitance(Farad)</i>
S₁	7.96E-12	3.40E-12
S_{1PHO}	7.91E-12	3.40E-12
S_{1PDS}	7.93E-12	3.40E-12
S_{1PDS+PHO}	7.92E-12	3.40E-12
S_{1SA}	7.86E-12	3.40E-12
S₂	8.84E-12	9.031E-12
S_{2PDS}	8.81E-12	9.031E-12
S_{2ATES}	8.76E-12	9.031E-12
S_{2ATES+PDS}	8.79E-12	9.031E-12

From Table 3.20, it is observed that Au/ Al₂O₃/ Au nanosandwiches have quantitatively different experimental and theoretical capacitance values than Au/ HfO₂/Au nanosandwiches. This is mainly because of the structure of the nanosandwiches, which consist of two conductive layers with an insulator layer (the dielectric material) in between. The dielectric materials can increase the surface charging when they are placed between two layers like Au layers (Neuendorf et al., 2001; Tunc et al., 2005). From the measured charges of the samples in Part 3.5, the capacitance values of nanosandwiches are calculated quantitatively (Tunc et al., 2005).

The theoretical capacitance value of Au/ HfO₂/ Au is calculated as 9.031E-12 F; which is greater than that of Au/ Al₂O₃/ Au, calculated as 3.40E-12 F. This is due to the fact that the dielectric constants of Al₂O₃ ve HfO₂ are different from each other (9.4 for Al₂O₃, 25 for HfO₂) (Tunc et al., 2005), (Zareie et al., 2008a). Since the dielectric constant of HfO₂ (25) is greater than that of Al₂O₃ (9.4), its calculated capacitance value (with Equation 3.2) is also higher.

Next, Equation 3.3 allows us to calculate the experimental capacitance values. When the Au/ Al₂O₃/ Au ve Au/ HfO₂/ Au nanosandwiches are examined, it is observed that the capacitance values of the unfunctionalized sample are greater than the capacitance values after the samples are functionalized with different polymers, as expected. The effect of polymers in reducing the capacitance values is explained in detail in the previous sections.

Finally, when we compared the theoretical and experimental (real) capacitance values of the nanosandwiches; theoretical capacitance value of Au/ HfO₂/ Au nanosandwiches (9.031E-12 farads) is very close to the experimental capacitance value which is 8.84E-12 farads. Likewise, the theoretical value for Au/ Al₂O₃/ Au nanosandwiches is 3.40E-12 farads which is fairly close to the experimental value of 7.96E-12 farads.

4. CONCLUSIONS AND RECOMMENDATIONS

In this thesis work, new nanomaterials and techniques are generated for the development of novel and improved capacitance based biosensors for the diagnosis of multiple diseases with single blood sample. Results have potential applications in biomedicine and biotechnology.

The aim of this study is to use the differential charging properties of Au/Al₂O₃/Au and Au/HfO₂/Au nanosandwich structures by applying external ± 10 voltage bias under 150- 250 kHz frequencies while recording XPS data, to measure the capacitance values of these nanostructures in order to obtain capacitance-based biosensors. Particularly, ± 10 V of external bias was chosen to apply to the surfaces in order to control the stray low-energy electrons sent from the flood gun, as well as the secondary electrons reflected from the surface. Thus, XPS was used to extract capacitance parameters of nanostructures under external bias with varying frequencies.

To our knowledge no previous study has investigated the use of metal/insulator/metal nanostructures as capacitors for biosensor applications. Charging/discharging properties of the nanostructures and the collection of charge into the dielectric layers are quite significant in order to produce biosensors.

However, Al₂O₃ and HfO₂ layers are dielectric materials that have different dielectric constants of 9.4 and 25, respectively. Since the dielectric constant of HfO₂ is greater than that of Al₂O₃; its nanosandwiches show capacitance properties in a wider range of frequency. The range of frequency for samples that include HfO₂ is observed between 185-215 kHz, as opposed to the range of 185-200 kHz for nanosandwiches that contain Al₂O₃ dielectric materials. We have demonstrated that each of the nanocapacitors have the charging capacity at specific frequency ranges by using XPS under SQW pulses. Therefore, we conclude that our samples act as capacitive devices when an external resistance of 10 M Ω was connected to the samples (which are considered as nanocapacitors) under SQW pulses (± 10 V) with different frequencies (while the flood gun was turned on).

The theoretical capacitance value of Au/ HfO₂/ Au is calculated as 9.031E-12 F; which is greater than that of Au/ Al₂O₃/ Au, calculated as 3.40E-12 F. This is due to the fact that the dielectric constants of Al₂O₃ ve HfO₂ are different from each other

(9.4 for Al_2O_3 , 25 for HfO_2). Since the dielectric constant of HfO_2 (25) is greater than that of Al_2O_3 (9.4), its calculated capacitance value is also higher.

When the Au/ Al_2O_3 / Au ve Au/ HfO_2 / Au nanosandwiches are examined, it is observed that the capacitance values of the unfunctionalized samples are greater than the capacitance values after the samples are functionalized with different polymers.

In this project, our aim was to develop a capacitance-based biosensor that can be used for diagnosis of multiple diseases with one blood sample. We used the differential charging properties to measure the capacitance value of the nanostructures in order to obtain capacitance-based biosensors. Thus, we can clearly say that our samples are charging and discharging at specific frequency range. We understand that our samples work like a capacitor at specific range of frequencies. We proved experimentally and theoretically the capacitance values of nanosandwiches. ERGTD

REFERENCES

- Barr, T.L.** 1989. Studies in differential charging. *Journal of Vacuum Science & Technology A: Vacuum, Surfaces, and Films*. 7:1677-1683.
- Bauer, M., C. Lei, K. Read, R. Tobey, J. Gland, M. Murnane, and H. Kapteyn.** 2001. Direct observation of surface chemistry using ultrafast soft-X-ray pulses. *Physical Review Letters*. 87:025501.
- Belluzo, M.S., M.É. Ribone, and C.M. Lagier.** 2008. Assembling amperometric biosensors for clinical diagnostics. *Sensors*. 8:1366-1399.
- Björneholm, O., A. Nilsson, A. Sandell, B. Hernnäs, and N. Mrtensson.** 1992. Determination of time scales for charge-transfer screening in physisorbed molecules. *Physical review letters*. 68:1892.
- Blanchard, C.R.** 1996. Atomic force microscopy. *The chemical educator*. 1:1-8.
- Boyer, C., V. Bulmus, T.P. Davis, V. Ladmiral, J. Liu, and S.b. Perrier.** 2009. Bioapplications of RAFT polymerization. *Chemical reviews*. 109:5402-5436.
- Briggs, D., M. Seah, and H. Bubern.** 1995. Practical Surface Analysis. Vol. 1: Auger and X-Ray Photoelectron Spectroscopy. *Angewandte Chemie-German Edition*. 107:1367-1367.
- Bulmus, V., Z. Ding, C.J. Long, P.S. Stayton, and A.S. Hoffman.** 2000. Site-specific polymer-streptavidin bioconjugate for pH-controlled binding and triggered release of biotin. *Bioconjugate chemistry*. 11:78-83.
- Cabane, E., X. Zhang, K. Langowska, C.G. Palivan, and W. Meier.** 2012. Stimuli-responsive polymers and their applications in nanomedicine. *Biointerphases*. 7:1-27.
- Carcia, P., R. McLean, M. Reilly, and G. Nunes.** 2003. Transparent ZnO thin-film transistor fabricated by rf magnetron sputtering. *Applied Physics Letters*. 82:1117-1119.
- Charnay, C., A. Lee, S.-Q. Man, C.E. Moran, C. Radloff, R.K. Bradley, and N.J. Halas.** 2003. Reduced symmetry metallodielectric nanoparticles: chemical synthesis and plasmonic properties. *The Journal of Physical Chemistry B*. 107:7327-7333.
- Cros, A.** 1992. Charging effects in X-ray photoelectron spectroscopy. *Journal of electron spectroscopy and related phenomena*. 59:1-14.
- Dane, A., U.K. Demirok, A. Aydinli, and S. Suzer.** 2006. X-ray photoelectron spectroscopic analysis of Si nanoclusters in SiO₂ matrix. *The Journal of Physical Chemistry B*. 110:1137-1140.
- Deckman, H., and J. Dunsmuir.** 1983. Applications of surface textures produced with natural lithography. *Journal of Vacuum Science & Technology B: Microelectronics and Nanometer Structures*. 1:1109-1112.
- DEMIROK, U.K.** 2005. investigation of electrical properties of surface structures by x-ray photoelectron spectroscopic technique under external voltage stimuli. *bilkent university*.
- Dickinson, T., A. Povey, and P. Sherwood.** 1975. X-ray photoelectron spectroscopic studies of solid electrolytes. *Journal of Solid State Chemistry*. 13:237-244.

- Dmitriev, A., T. Pakizeh, M. Käll, and D.S. Sutherland.** 2007. Gold–silica–gold nanosandwiches: tunable bimodal plasmonic resonators. *Small*. 3:294-299.
- Doron-Mor, I., A. Hatzor, A. Vaskevich, T. van der Boom-Moav, A. Shanzer, I. Rubinstein, and H. Cohen.** 2000. Controlled surface charging as a depth-profiling probe for mesoscopic layers. *Nature*. 406:382-385.
- Drescher, M., M. Hentschel, R. Kienberger, M. Uiberacker, V. Yakovlev, A. Scrinzi, T. Westerwalbesloh, U. Kleineberg, U. Heinzmann, and F. Krausz.** 2002. Time-resolved atomic inner-shell spectroscopy. *Nature*. 419:803-807.
- Dubey, M., I. Gouzman, S.L. Bernasek, and J. Schwartz.** 2006. Characterization of self-assembled organic films using differential charging in X-ray photoelectron spectroscopy. *Langmuir*. 22:4649-4653.
- Ekiz, O.O., K. Mizrak, and A. Dâna.** 2010. Chemically specific dynamic characterization of photovoltaic and photoconductivity effects of surface nanostructures. *ACS nano*. 4:1851-1860.
- Endo, K., S. Koizumi, T. Otsuka, M. Suhara, T. Morohasi, E. Kurmaev, and D. Chong.** 2001. Analysis of XPS and XES of diamond and graphite by DFT calculations using model molecules. *Journal of Computational Chemistry*. 22:102-108.
- Ertas, G., and S. Suzer.** 2004. XPS analysis with external bias: a simple method for probing differential charging. *Surface and interface analysis*. 36:619-623.
- Ertas, G., and S. Suzer.** 2006. Analysis of surface structures using XPS with external stimuli. In *Surface Chemistry in Biomedical and Environmental Science*. Springer. 45-58.
- Faber, B.C., S. Heeneman, M.J. Daemen, and K.B. Cleutjens.** 2002. Genes potentially involved in plaque rupture. *Current opinion in lipidology*. 13:545-552.
- Fan, X., L. Lin, and P.B. Messersmith.** 2006. Cell fouling resistance of polymer brushes grafted from Ti substrates by surface-initiated polymerization: effect of ethylene glycol side chain length. *Biomacromolecules*. 7:2443-2448.
- Gil, E.S., and S.M. Hudson.** 2004. Stimuli-responsive polymers and their bioconjugates. *Progress in polymer science*. 29:1173-1222.
- Gouzman, I., M. Dubey, M.D. Carolus, J. Schwartz, and S.L. Bernasek.** 2006. Monolayer vs. multilayer self-assembled alkylphosphonate films: X-ray photoelectron spectroscopy studies. *Surface science*. 600:773-781.
- Graves, B.J., M.H. Hatada, W.A. Hendrickson, J.K. Miller, V.S. Madison, and Y. Satow.** 1990. Structure of interleukin 1. alpha. at 2.7-Å resolution. *Biochemistry*. 29:2679-2684.
- Guittet, M., J. Crocombette, and M. Gautier-Soyer.** 2001. Bonding and XPS chemical shifts in ZrSiO₄ versus SiO₂ and ZrO₂: Charge transfer and electrostatic effects. *Physical Review B*. 63:125117.
- Haes, A.J., L. Chang, W.L. Klein, and R.P. Van Duyne.** 2005. Detection of a biomarker for Alzheimer's disease from synthetic and clinical samples using a nanoscale optical biosensor. *Journal of the American Chemical Society*. 127:2264-2271.
- Haes, A.J., and R.P. Van Duyne.** 2004. A unified view of propagating and localized surface plasmon resonance biosensors. *Analytical and Bioanalytical Chemistry*. 379:920-930.

- Havercroft, N., and P. Sherwood.** 2000. Use of differential surface charging to separate chemical differences in x-ray photoelectron spectroscopy. *Surface and interface analysis*. 29:232-240.
- Hoffman, A.S.** 1995. "Intelligent" polymers in medicine and biotechnology. In *Macromolecular Symposia*. Vol. 98. Wiley Online Library. 645-664.
- Holmberg, A., A. Blomstergren, O. Nord, M. Lukacs, J. Lundeberg, and M. Uhlén.** 2005. The biotin-streptavidin interaction can be reversibly broken using water at elevated temperatures. *Electrophoresis*. 26:501-510.
- Höfer, U., I. Shumay, C. Reuß, U. Thomann, W. Wallauer, and T. Fauster.** 1997. Time-resolved coherent photoelectron spectroscopy of quantized electronic states on metal surfaces. *Science*. 277:1480-1482.
- Hövel, H., I. Barke, H.-G. Boyen, P. Ziemann, M. Garnier, and P. Oelhafen.** 2004. Photon energy dependence of the dynamic final-state effect for metal clusters at surfaces. *Physical Review B*. 70:045424.
- Hövel, H., B. Grimm, M. Pollmann, and B. Reihl.** 1998. Cluster-substrate interaction on a femtosecond time scale revealed by a high-resolution photoemission study of the Fermi-level onset. *Physical review letters*. 81:4608.
- Huang, Y., Q. Liu, X. Zhou, S.b. Perrier, and Y. Zhao.** 2009. Synthesis of silica particles grafted with well-defined living polymeric chains by combination of RAFT polymerization and coupling reaction. *Macromolecules*. 42:5509-5517.
- Huang, Z., and J. Zhu.** 2007. Growth and enhanced emission of silicon-germanium hemisphere shell arrays. *Applied physics letters*. 91:013108-013108-013103.
- Hulteen, J.C., D.A. Treichel, M.T. Smith, M.L. Duval, T.R. Jensen, and R.P. Van Duyne.** 1999. Nanosphere lithography: size-tunable silver nanoparticle and surface cluster arrays. *The Journal of Physical Chemistry B*. 103:3854-3863.
- Hulteen, J.C., and R.P. Van Duyne.** 1995. Nanosphere lithography: A materials general fabrication process for periodic particle array surfaces. *Journal of Vacuum Science & Technology A: Vacuum, Surfaces, and Films*. 13:1553-1558.
- Hyun, J., Y. Zhu, A. Liebmman-Vinson, T.P. Beebe, and A. Chilkoti.** 2001. Microstamping on an activated polymer surface: Patterning biotin and streptavidin onto common polymeric biomaterials. *Langmuir*. 17:6358-6367.
- Ishii, M.** 2009. Selective X-ray analysis of electron localizing sites using capacitance or electrostatic force. *Electronics and Communications in Japan*. 92:38-45.
- Iwata, S., and A. Ishizaka.** 1996. Electron spectroscopic analysis of the SiO₂/Si system and correlation with metal-oxide-semiconductor device characteristics. *Journal of applied physics*. 79:6653-6713.
- Javey, A., H. Kim, M. Brink, Q. Wang, A. Ural, J. Guo, P. McIntyre, P. McEuen, M. Lundstrom, and H. Dai.** 2002. High- κ dielectrics for advanced carbon-nanotube transistors and logic gates. *Nature materials*. 1:241-246.
- Jiang, P.** 2004. Surface-Templated Nanostructured Films with Two-Dimensional Ordered Arrays of Voids. *Angewandte Chemie*. 116:5743-5746.
- Jianrong, C., M. Yuqing, H. Nongyue, W. Xiaohua, and L. Sijiao.** 2004. Nanotechnology and biosensors. *Biotechnology Advances*. 22:505-518.
- Johnson, P.A., and R. Levicky.** 2004. X-ray photoelectron spectroscopy and differential capacitance study of thiol-functional polysiloxane films on gold supports. *Langmuir*. 20:9621-9627.

- Kaifer, A.E.** 1992. Fundamentals of Analytical Chemistry. (Skoog, Douglas A.; West, Donald M.; Hollar, James F.). *Journal of Chemical Education*. 69:A305.
- Karabudak, E., U.K. Demirok, and S. Suzer.** 2006. XPS analysis with pulsed voltage stimuli. *Surface science*. 600:L12-L14.
- Karadas, F., G. Ertas, and S. Suzer.** 2004. Differential charging in SiO₂/Si system as determined by XPS. *The Journal of Physical Chemistry B*. 108:1515-1518.
- Kerber, S., J. Bruckner, K. Wozniak, S. Seal, S. Hardcastle, and T. Barr.** 1996. The nature of hydrogen in x-ray photoelectron spectroscopy: General patterns from hydroxides to hydrogen bonding. *Journal of Vacuum Science & Technology A: Vacuum, Surfaces, and Films*. 14:1314-1320.
- King, R.W.P.** 1963. Fundamental Electromagnetic Theory. Dover Publications.
- Knop-Gericke, A.** 2012. X-ray Photoelectron Spectroscopy. An Introduction to Principles and Practices. By Paul van der Heide. *Angewandte Chemie International Edition*. 51:9218-9218.
- Lal, S.P., R.I. Christopherson, and C.G. dos Remedios.** 2002. Antibody arrays: an embryonic but rapidly growing technology. *Drug Discovery Today*. 7:S143-S149.
- Lau, W.** 1989. Use of surface charging in x-ray photoelectron spectroscopic studies of ultrathin dielectric films on semiconductors. *Applied Physics Letters*. 54:338-340.
- Lau, W., and X.-W. Wu.** 1991. Measurements of interface state density by X-ray photoelectron spectroscopy. *Surface science*. 245:345-352.
- Lewis, R., and M. Kelly.** 1980. Binding-energy reference in X-ray photoelectron spectroscopy of insulators. *Journal of Electron Spectroscopy and Related Phenomena*. 20:105-115.
- Lide, D.R.** 2004. CRC Handbook of Chemistry and Physics 2004-2005: A Ready-Reference Book of Chemical and Physical Data. CRC press.
- Lindgren, T., J.M. Mwabora, E. Avendaño, J. Jonsson, A. Hoel, C.-G. Granqvist, and S.-E. Lindquist.** 2003. Photoelectrochemical and optical properties of nitrogen doped titanium dioxide films prepared by reactive DC magnetron sputtering. *The Journal of Physical Chemistry B*. 107:5709-5716.
- Love, J.C., L.A. Estroff, J.K. Kriebel, R.G. Nuzzo, and G.M. Whitesides.** 2005. Self-assembled monolayers of thiolates on metals as a form of nanotechnology. *Chemical reviews*. 105:1103-1170.
- Marsi, M., R. Belkhou, C. Grupp, G. Panaccione, A. Taleb-Ibrahimi, L. Nahon, D. Garzella, D. Nutarelli, E. Renault, and R. Roux.** 2000. Transient charge carrier distribution at UV-photoexcited SiO₂/Si interfaces. *Physical Review B*. 61:R5070.
- Metson, J.** 1999. Charge compensation and binding energy referencing in XPS analysis. *Surface and interface analysis*. 27:1069-1072.
- Michael, K.L., L.C. Taylor, S.L. Schultz, and D.R. Walt.** 1998. Randomly ordered addressable high-density optical sensor arrays. *Analytical chemistry*. 70:1242-1248.
- Neuendorf, R., A. Brysch, G. Bour, and U. Kreibig.** 2001. Optical properties of II-VI semiconductor nanoparticles. In International Symposium on Optical Science and Technology. International Society for Optics and Photonics. 39-47.

- Nikitin, A., H. Ogasawara, D. Mann, R. Denecke, Z. Zhang, H. Dai, K. Cho, and A. Nilsson.** 2005. Hydrogenation of single-walled carbon nanotubes. *Physical review letters*. 95:225507.
- Rowe, C.A., L.M. Tender, M.J. Feldstein, J.P. Golden, S.B. Scruggs, B.D. MacCraith, J.J. Cras, and F.S. Ligler.** 1999. Array biosensor for simultaneous identification of bacterial, viral, and protein analytes. *Analytical Chemistry*. 71:3846-3852.
- Savage, M.D.** 1992. Avidin-biotin chemistry. Pierce Chemical Co.
- Schmaljohann, D.** 2006. Thermo- and pH-responsive polymers in drug delivery. *Advanced drug delivery reviews*. 58:1655-1670.
- Schreiber, F.** 2000. Structure and growth of self-assembling monolayers. *Progress in surface science*. 65:151-257.
- Sezen, H., G. Ertas, A. Dâna, and S. Suzer.** 2007. Charging/discharging of thin PS/PMMA films as probed by dynamic X-ray photoelectron spectroscopy. *Macromolecules*. 40:4109-4112.
- Shiraki, I., Y. Miyatake, T. Nagamura, and K. Miki.** 2006. Demonstration of low-temperature atomic force microscope with atomic resolution using piezoresistive cantilevers. *Review of scientific instruments*. 77:023705-023705-023704.
- Siegbahn, K., C. Nordling, and A. Fahlman.** 1967. ESCA, atomic, molecular and solid state structure studied by means of electron spectroscopy. *Nov. Act. Uppsaliensis*.
- Solyman, L., and D. Walsh.** 2009. Electrical properties of materials. Oxford University Press.
- Suzer, S.** 2003. Differential charging in X-ray photoelectron spectroscopy: A nuisance or a useful tool? *Analytical chemistry*. 75:7026-7029.
- Suzer, S., and A. Dâna.** 2006. X-ray photoemission for probing charging/discharging dynamics. *The Journal of Physical Chemistry B*. 110:19112-19115.
- Suzer, S., A. Dâna, and G. Ertas.** 2007. Differentiation of domains in composite surface structures by charge-contrast X-ray photoelectron spectroscopy. *Analytical chemistry*. 79:183-186.
- Suzer, S., H. Sezen, and A. Dâna.** 2008. Two-dimensional X-ray photoelectron spectroscopy for composite surface analysis. *Analytical chemistry*. 80:3931-3936.
- Sze, S.M., and K.K. Ng.** 2006. Physics of semiconductor devices. Wiley. com.
- Takahashi, H., K. Ando, and Y. Shirakawabe.** 2002. Self-sensing piezoresistive cantilever and its magnetic force microscopy applications. *Ultramicroscopy*. 91:63-72.
- Tunc, I., U.K. Demirok, S. Suzer, M.A. Correa-Duarte, and L.M. Liz-Marzan.** 2005. Charging/discharging of Au (core)/silica (shell) nanoparticles as revealed by XPS. *The Journal of Physical Chemistry B*. 109:24182-24184.
- Ulgut, B., and S. Suzer.** 2003. XPS studies of SiO₂/Si system under external bias. *The Journal of Physical Chemistry B*. 107:2939-2943.
- Ulman, A.** 1996. Formation and structure of self-assembled monolayers. *Chemical reviews*. 96:1533-1554.
- Van Grieken, R., and A. Markowicz.** 2001. Handbook of X-ray Spectrometry. CRC Press.

- Védrine, C., S. Fabiano, and C. Tran-Minh.** 2003. Amperometric tyrosinase based biosensor using an electrogenerated polythiophene film as an entrapment support. *Talanta*. 59:535-544.
- Wagner, C., D. Briggs, and M. Seah.** 1990. Practical surface analysis. *Auger and X-ray Photoelectron Spectroscopy*. 1:595.
- Wagner, C., and J.A. Taylor.** 1980. Generation of XPS Auger lines by bremsstrahlung. *Journal of Electron Spectroscopy and Related Phenomena*. 20:83-93.
- Wagner, C.D.** 1979. Handbook of x-ray photoelectron spectroscopy: a reference book of standard data for use in x-ray photoelectron spectroscopy. Physical Electronics Division, Perkin-Elmer Corp.
- Weber, P.C., D. Ohlendorf, J. Wendoloski, and F. Salemme.** 1989. Structural origins of high-affinity biotin binding to streptavidin. *Science*. 243:85-88.
- Xia, N., J.S. Shumaker-Parry, M.H. Zareie, C.T. Campbell, and D.G. Castner.** 2004. A streptavidin linker layer that functions after drying. *Langmuir*. 20:3710-3716.
- Xu, F., H. Li, J. Li, Y. Teo, C. Zhu, E. Kang, and K. Neoh.** 2008. Spatially well-defined binary brushes of poly (ethylene glycol) s for micropatterning of active proteins on anti-fouling surfaces. *Biosensors and Bioelectronics*. 24:773-780.
- Yonzon, C.R., D.A. Stuart, X. Zhang, A.D. McFarland, C.L. Haynes, and R.P. Van Duyne.** 2005. Towards advanced chemical and biological nanosensors—an overview. *Talanta*. 67:438-448.
- Young, R.A.** 2000. Biomedical discovery with DNA arrays. *Cell*. 102:9-15.
- Zareie, H.M., C. Boyer, V. Bulmus, E. Nateghi, and T.P. Davis.** 2008a. Temperature-responsive self-assembled monolayers of oligo (ethylene glycol): control of biomolecular recognition. *ACS nano*. 2:757-765.
- Zareie, H.M., S.W. Morgan, M. Moghaddam, A.I. Maarroof, M.B. Cortie, and M.R. Phillips.** 2008b. Nanocapacitive Circuit Elements. *ACS nano*. 2:1615-1619.
- Zhai, J., H. Cui, and R. Yang.** 1997. DNA based biosensors. *Biotechnology advances*. 15:43-58.
- Zhang, X., C. Yonzon, M. Young, D. Stuart, and R. Van Duyne.** 2005. Surface-enhanced Raman spectroscopy biosensors: excitation spectroscopy for optimisation of substrates fabricated by nanosphere lithography. *In IEE Proceedings-Nanobiotechnology*. Vol. 152. IET. 195-206.
- Zhu, H., M. Bilgin, R. Bangham, D. Hall, A. Casamayor, P. Bertone, N. Lan, R. Jansen, S. Bidlingmaier, and T. Houfek.** 2001. Global analysis of protein activities using proteome chips. *science*. 293:2101-2105.

CURRICULUM VITAE

Name Surname: Sümeyra GÖKALP

Place and Date of Birth: Ankara-1985

Address: Boston, MA, USA

E-Mail: gokalpsumeyra@gmail.com

B.Sc.: Uludağ University

M.Sc.: Gediz University

Professional Experience and Rewards:

-University of Texas at Dallas, Richardson, TX July 2012 – May 2013 Visiting Research Scholar at Material Science and Engineering Department

-Uludag University, Bursa, Turkey 2010-2011 Pedagogical Proficiency in Chemistry

-Hasan Ali Yucel High School, Bursa, Turkey 2010-2011 Teaching Intern

-Polikor Paint, Resin and Polyester A.S., Bursa, Turkey August-September 2009

-TUBITAK (The Scientific and Technological Research Council of Turkey) Project Scholarship 2012-2013

-Recipient of Turkish Prime Ministry Full Scholarship for Undergraduate Education in Turkey 2005-2010

List of Publications and Presentation:

Chemical Stability and Reactivity of HF Etched Silicon Nitride Surfaces (Poster presented at the TECHCON conference, Austin, TX), 2013, with Peixoto, T., Debenedetti, W., Gokalp, S., Ramos, K.B., and Prof. Yves J. Chabal.